Investigation of Strain Relaxation Mechanisms and Interfacial Defects in Lattice-mismatched GaAs(001)-based Heterostructures

by

Abhinandan Gangopadhyay

A Dissertation Presented in Partial Fulfilment
of the Requirements for the Degree
Doctor of Philosophy

Approved December 2020 by the
Graduate Supervisory Committee:

David J. Smith, Chair
Mariana Bertoni
Peter A. Crozier
Richard R. King
Martha R. McCartney

ARIZONA STATE UNIVERSITY

May 2021

ABSTRACT

The evolution of defects at different stages of strain relaxation in low-mismatched GaAs/$GaAs_{1-x}Sb_x$/GaAs(001) (x ~ 0.08) heterostructures, and the underlying relaxation mechanisms, have been comprehensively studied primarily using transmission electron microscopy (TEM). Aberration-corrected scanning transmission electron microscopy (STEM) has been used for atomic-scale study of interfacial defects in low-mismatched GaAs(001)-based and high-mismatched GaSb/GaAs(001) heterostructures.

Three distinct stages of strain relaxation were identified in GaAs/$GaAs_{1-x}Sb_x$/GaAs(001) (x ~ 0.08) heterostructures with GaAsSb film thicknesses in the range of 50 to 4000 nm capped with 50-nm-thick GaAs layers. Diffraction contrast analysis with conventional TEM revealed that although 60° dislocations were primarily formed during the initial sluggish Stage-I relaxation, 90° dislocations were also created. Many curved dislocations, the majority of which extended into the substrate, were formed during Stage-II and Stage-III relaxation. The capping layers of heterostructures with larger film thickness (500 nm onwards) exhibited only Stage-I relaxation. A decrease in dislocation density was observed at the cap/film interface of the heterostructure with 4000-nm-thick film compared to that with 2000-nm-thick film, which correlated with smoothening of surface cross-hatch morphology. Detailed consideration of plausible dislocation sources for the capping layer led to the conclusion that dislocation half-loops nucleated at surface troughs were the main source of threading dislocations in these heterostructures.

Aberration-corrected STEM imaging revealed that interfacial 60° dislocations in GaAs/GaAsSb/GaAs(001) and GaAs/GaAsP/GaAs(001) heterostructures were dissociated to form intrinsic stacking faults bounded by 90° and 30° Shockley partial

dislocations. The cores of the 30° partials contained single atomic columns indicating that these dislocations primarily belonged to glide set. Apart from isolated dissociated 60° dislocations, Lomer-Cottrell locks, Lomer dislocations and a novel type of dissociated 90° dislocation were observed in GaAs/GaAsSb/GaAs heterostructures.

The core structure of interfacial defects in GaSb/GaAs(001) heterostructure was also investigated using aberration-corrected STEM. 90° Lomer dislocations were primarily formed; however, glide-set perfect 60° and dissociated 60° dislocations were also observed. The 5-7 atomic-ring shuffle-set dislocation, the left-displaced 6-8 atomic-ring glide-set and the right-displaced 6-8 atomic-ring glide-set dislocations were three types of Lomer dislocations that were identified, among which the shuffle-set type was most common.

This dissertation is dedicated to my parents – *Jaya Gangopadhyay* and *Udayan Gangopadhyay;* and my elder sister *Koyel*

ACKNOWLEDGEMENTS

I would like to take this opportunity to sincerely thank my advisor, Regents' professor David J. Smith, for introducing me to the fascinating world of transmission electron microscopy. I am grateful for his constant guidance, support and encouragement in different aspects of both professional and personal life, throughout my doctoral study. His enthusiasm and positive attitude towards research have taught me valuable lessons which would be great treasure for my future career.

I would like to thank Prof. Martha McCartney for her help with microscope operation and many insightful comments, which have helped shape my research. I would also like to thank Prof. Mariana Bertoni, Prof. Peter Crozier and Prof. Richard R. King for serving on my dissertation committee. I am thankful to Dr. Nikolai Faleev, Dr. Aymeric Maros and Prof. Ganesh Balakrishnan for their collaboration. I am especially grateful to Dr. Faleev for the numerous interesting discussions, advices and suggestions. I am also grateful for the use of facilities within John M. Cowley Center of High Resolution Electron Microscopy. I would like to thank Karl Weiss, Dr. Toshihiro Aoki, Dr. Manuel Roldan Gutierrez, Diana Convey and Ken Mossman for their help with my training on microscopes and instruments for sample preparation.

Special thanks go to Molly & Dave Gang (MDG) members – Dr. Allison Boley, Dr. Ajit Dhamdhere, Dr. Jing Lu, Dr. Sirong Lu, Dr. Thomas McConkie, Dr. Brandon McKeon, Prudhvi Ram Peri, Scott Sherman, Dr. Brian Tracy, Dr. Majid Vaghayenegar and Dr. HsinWei Wu for the interesting discussions and friendship in general. Cheers to the lunch session discussions with Shanthan and Kartik on wide-ranging topics, which provided much-needed recess from daily research activities.

Above all, I would like to thank my family for their unconditional love and for being always there during tough times as well as at moments of happiness.

TABLE OF CONTENTS

Page

LIST OF TABLES x

LIST OF FIGURES xi

CHAPTER

1 INTRODUCTION 1

1.1 Semiconductors 1

1.2 Semiconductor Heterostructures 2

1.3 Growth Modes 4

1.4 Strained Layer Epitaxy 6

1.5 Strain Relaxation in Epitaxially-Grown Lattice-Mismatched Heterostructures 7

1.5.1 Critical Thickness 7

1.5.2 Geometry and Type of Misfit Dislocations 8

1.5.3 Dislocation Nucleation and Interaction Events in Low-mismatched Heterostructures 10

1.5.4 Asymmetric Strain Relaxation in Low-Mismatched Heterostructures 12

1.6 Core Structure of Defects 13

1.6.1 60° Dislocations 14

1.6.2 Interaction of 60° Dislocations 18

CHAPTER Page

1.7 Outline of Dissertation 19

References 21

2 EXPERIMENTAL METHODS 24

2.1 Molecular Beam Epitaxy 24

2.2 X-ray Diffraction 26

2.3 Transmission Electron Microscopy 26

2.3.1 Convergent Beam Electron Diffraction (CBED) 28

2.3.2 Imaging 29

2.4 Sample Preparation for TEM 30

2.5 Atomic Force Microscopy (AFM) 31

References 32

3 STRAIN RELAXATION IN LOW-MISMATCHED GaAs/$GaAs_{1-X}Sb_X$/GaAs HETEROSTRUCTURES 33

3.1 Introduction and Motivation 33

3.2 Experimental Details 34

3.3 Results and Discussion 37

3.3.1 Strain Relaxation Stages at The Film/Substrate Interface 37

3.3.2 Defects Formed During Stage-I Relaxation 38

3.4 Defects in Stage-II And Stage-III of Strain Relaxation 43

CHAPTER Page

3.5 Strain Relaxation at The Cap/Film Interface 45

3.6 Asymmetric Dislocation Distribution During Stage-I Relaxation 46

3.6.1 Distinguishing <110> Directions in Plan-View Projection 47

3.7 Dislocation Nucleation and Density Evolution at GaAsSb/GaAs and GaAs/GaAsSb Interfaces During Stage-I Relaxation 55

3.8 Conclusions 66

References 68

4 ATOMIC-SCALE CHARACTERIZATION OF INTERFACIAL DEFECTS IN LOW-MISMATCHED GaAs(001)-BASED HETEROSTRUCTURES........... 71

4.1 Introduction and Motivation 71

4.2 Dissociated 60° Dislocations 72

4.3 Lomer-Cottrell Locks..82

4.4 Lomer Dislocations 85

4.5 Conclusions 90

References 91

5 ATOMIC-RESOLUTION STRUCTURAL IMAGING OF INTERFACIAL DEFECTS IN GaSb/GaAs(001) HETEROSTRUCTURE................................. 93

5.1 Introduction 93

5.2 Results and Discussion...94

CHAPTER Page

5.3 Summary 103

References 104

6 SUMMARY AND FUTURE WORK 105

6.1 Summary 105

6.2 Future Work 107

References 110

LIST OF REFERENCES 111

LIST OF TABLES

Table Page

3.1 Sample Details 36

3.2 Slip Plane, Burgers Vector and g.b/g.b×u Contrast for Two-beam Conditions with Excited $\bar{2}20/220$ Reflection for 60° and 90° Dislocations having $\bar{1}10/110$ Dislocation Line. 40

3.3 Dislocation Densities at Heterointerfaces That have Undergone Stage-I Relaxation...59

LIST OF FIGURES

Figure Page

1.1 Schematic Diagram Showing The Three Types of Band Alignment in Undoped Heterojunctions: (a) Type-I, (b) Type-II, and (c) Type-III Heterostructures. E_{c1} and E_{c2} are The Conduction-band Edges and E_{v1} and E_{v2} are The Valence-band Edges of The Two Materials Forming The Heterojunction....................2

1.2 Plot of Band-gap Energy vs. Lattice Constant for Si, Ge and Common III-V Semiconductors [2]....................3

1.3 Growth Modes in Epitaxial Thin Film Growth - (a) FM Layer-by-layer Growth, (b) SK Layer + island Growth and (c) VW Island Growth. θ Is The Coverage Expressed in Monolayer (ML). 5

1.4 Schematic Description of: (a) 60° Misfit Dislocation Formation by Glide of Threading Dislocation Segment, and (b) Final Network of Misfit Dislocations at The Interface Plane. 9

1.5 (a) [110] and (b) $[1\bar{1}0]$ Projected Structures of Shuffle-set 60° Negative Dislocation Showing Extra Half-planes That are Terminated by As and Ga Atoms, Respectively; (c) [110] and (d) $[1\bar{1}0]$ Projected Structures of Glide-set 60° Negative Dislocation Showing That The Extra Half-planes are Terminated by Ga and As Atoms, Respectively. 14

Figure Page

1.6 [111] Projected Images of: (a) Perfect Diamond Crystal, (b) Unreconstructed Core of 30° partial, (c) Unreconstructed Core of 90° Partial, (d) Double-period Reconstructed Core of 30° Partial, (e) Single-period Reconstructed Core of 90° Partial, and (f) Double-period Reconstructed Core of 90° Partial. The Black and White Atoms Represent Atomic Layers That are Just Below and Above The (111) Glide Plane [42]..16

2.1 Schematic of MBE System Used for Growing The Semiconductor Heterostructures Investigated in This Study. 25

3.1 Schematic Cross-sectional Illustration (Not to Scale) Showing Geometry of GaAs(cap)/$GaAs_{1-x}Sb_x$/GaAs (001) Heterostructures.....................................34

3.2 Percentage of Strain Relaxation vs. Film Thickness Showing Three Stages of Strain Relaxation in $GaAs_{1-x}Sb_x$/GaAs Heterostructures................................38

3.3 Bright-field Plan-view TEM Images Showing Orthogonal Network of Misfit Dislocations at The $GaAs_{1-x}Sb_x$/GaAs Interface Plane for: (a) Sample B, and (b) Sample C. Bright-field Cross-sectional TEM Images of: (c) Sample B, and (d) Sample C. 39

3.4 $GaAs_{1-x}Sb_x$/GaAs Interface Plane in Sample C: (a) Bright-field Plan-view TEM Image, (b) Bright-field $g = \bar{2}20$ Image; and (c) Bright-field $g = 220$ Image..41

3.5 Plan-view TEM Images Showing Dislocation Distribution at The Interface Plane of: (a) Sample D, and (b) Sample E. Bright-field Cross-sectional TEM

Figure Page

Images of: (c) Sample D, and (d) Sample E. Bright-field Two-beam Plan-view Images Formed with: (e) $g = 220$, and (f) $g = \bar{2}20$ in Sample D. 44

3.6 Bright-field Cross-sectional TEM Images of (a) Sample F, (b) Sample G and (c) Sample H. Interfacial Defects are Present at GaAsSb/GaAs Film/substrate Interfaces. However, No Threading Dislocation is Visible in Any of The Images. 45

3.7 Bright-field Plan-view TEM Images Showing Distribution of Misfit Dislocations at The Cap/film Interfaces of: (a) Sample E, (b) Sample F, (c) Sample G, and (d) Sample H……………………………………………...46

3.8 (a) Cross-sectional TEM (XTEM) Image of GaAs/GaAsSb/GaAs Heterostructure Showing In-plane [001] Growth Direction; (b) Experimental CBED Pattern Collected from The GaAs Substrate Region of (a); (c) Simulated [110] Zone-axis CBED Pattern Matched with The Experimental Pattern Shown in (b); (d) Schematic of The Geometry of XTEM and Plan-view TEM Samples Showing In-plane and Out-of-plane Directions; (e) Plan-view TEM Image with Identified In-plane $[110]$ and $[1\bar{1}0]$ Directions. 49

3.9 Collage of Plan-view Bright-field [001] Projected Images Showing Distribution of Misfit Dislocations Along The Two <110> Directions in at The Cap/film Interface of GaAs/$GaAs_{0.917}Sb_{0.083}$/GaAs(001) Heterostructure with 2000-nm-thick Film. 52

Figure Page

3.10 Plot Showing Dislocation Spacing as a Function of Excess Stress for Film/substrate Interfaces and Cap/film Interfaces of GaAs/GaAsSb/GaAs Heterostructures. 53

3.11 Schematic Depiction of Possible Strain Relaxation Mechanisms at The Cap/film Interface: (a) Extended Double-kink Motion of Threading Dislocation in The Film; (b) Glide of Threading Dislocation in The Capping Layer, which is Blocked at The Film/substrate Interface; (c) Surface Half-loop Creation and Subsequent Glide of Threading Dislocation in The Capping Layer. 56

3.12 Evolution of Excess Stress and Dislocation Density with Increasing Film Thickness. The Dislocation Density Values are Shown for Film/substrate Interfaces in Samples B and C, and for Cap/film Interfaces in Samples F, G and H. The Two Arrows Mark The Onset of Relaxation at The Two Interfaces: Sample A for Film/substrate Interface and Sample E for Cap/film Interface. SK: Single-kink, DK: Double-kink. 61

3.13 (a) Surface Height Profiles Along <110> Direction Obtained by AFM in Samples E-H. AFM Images Showing Surface Topography of (b) Sample G and (c) Sample H. 65

4.1 (a) Crystal Model Showing Burgers Vectors of Perfect 60° Dislocations and Shockley Partial Dislocations Generated at Compressively-strained (001) Interface. Aberration-corrected HAADF-STEM Images of

Figure Page

GaAsSb/GaAs(001) Heterostructure Showing: (b) Dissociated 60° Dislocation at Film/substrate Interface, (c) 90° Partial Dislocation Located Very Close to Film/substrate Interface, and (d) 30° Partial Dislocation Located Well into Substrate [12]. 74

4.2 Atomic Structural Models of Dissociated 60° Dislocation for: (a) Interstitial Shuffle Type, (b) Vacancy Shuffle Type, and (c) Glide Type. The Cores of 90° and 30° Partial Dislocations are Marked by Green and Red Arrows, Respectively. The Faulted Area is Shown by Dashed Box [12]. 76

4.3 (a) Aberration-corrected HAADF-STEM Image of Dissociated 60° Misfit Dislocation at GaAsSb/GaAs Interface. The Pseudo-colored Magnified Image of 30° Partial in Inset Clearly Shows Presence of Unpaired Ga Atomic Column at Dislocation Core. (b) HAADF-STEM Image of Dissociated 60° Misfit Dislocation at Cap/film Interface, Showing Presence of Single As Atomic Column at 30° Partial Dislocation Core [12]. 78

4.4 Aberration-corrected HAADF-STEM Images Showing The Location of 30° and 90° Shockley Partials with Respect to: (a) Compressively-strained Film/substrate Interface, and (b) Tensile-strained Cap/film Interface in GaAs/GaAsSb/GaAs Heterostructure. Interface Locations are Shown by Dashed White Lines [12]. 79

4.5 Aberration-corrected HAADF-STEM Image Showing Dissociated 60° Dislocation at The Tensile-strained Film/substrate GaAsP/GaAs Interface in

Figure Page

GaAs/GaAsP/GaAs Heterostructure. Interface Location Indicated by Dashed White Line. 81

4.6 (a) Aberration-corrected HAADF-STEM [110] Projected Images Showing Two Intersecting Stacking Faults Forming Stair-rod Dislocation at Film/substrate Interface. (d) Bright-field STEM Image Showing Location of One 90° Partial Corresponding to Defect Complex Shown in (a). The Film/substrate Interface is Marked By White Dashed Line. Inset Shows Low Magnification Image Illustrating That The Entire Defect Lies in The Substrate..83

4.7 (a) Aberration-corrected HAADF-STEM Image of Lomer Edge Dislocation in Sample E. Bright-field STEM Images Showing (b) Location of Edge Dislocation in (a) Relative to Strained Film/Substrate Interface, and (c) Another Lomer Edge Dislocation Situated Right at Film/substrate Interface of Sample F. Interfaces are Marked By White Dashed Lines [21]. 85

4.8 Atomic-resolution HAADF-STEM Image Showing Dissociated 90° Dislocation at $GaAs_{0.913}Sb_{0.087}$/GaAs Interface. RH/FS Burgers Circuits are Drawn around The Fault and Partial Dislocations. The Magnified Image of Boxed Area Around The Trailing Partial Core Shows Burgers Vector (Red Arrow) of Trailing Partial as A Resultant of Burgers Vector (green arrow) of Perfect 60° Dislocation and Burgers Vector (Blue Arrow) of 90° Shockley Partial Dislocation. Magnified Image at The Bottom Portion of The Image Shows Boxed Area around 30° Partial Core..88

Figure Page

5.1 (a) TEM Micrograph of GaSb/GaAs(001) Heterostructure Revealing The Crystalline Quality and Defect Structure of The GaSb Layer. (b) Atomic-resolution HAADF-STEM Structural Image of GaSb/GaAs Heterointerface Region Showing Short {111}-type Intrinsic Stacking Fault (Yellow Arrow), 60° Dislocation (Red Arrow) and Two Lomer Dislocations (White Arrows). 95

5.2 (a) Atomic-resolution LABF-STEM Structural Image of Interfacial Dislocation at GaSb/GaAs Interface, Together with Corresponding RH/FS Burgers Circuit. (b) HAADF-STEM Image of The Same Defect With Structural Model Overlaid on The Dislocation Depicting The Five-membered and Seven-membered Atomic Ring Arrangements at The Defect Core. 96

5.3 (a) Atomic-resolution LABF-STEM Image of Dislocation Located at GaSb/GaAs Interface with Corresponding RH/FS Burgers Circuit. (b) HAADF-STEM Image of The Dislocation Core and Intensity Profile (Inset) Revealing Two Distinct Peaks Corresponding to Separate Atomic Columns. (c) Proposed Atomic Arrangement at Dislocation Core Overlaid on HAADF-STEM Image. 97

5.4 (a) Aberration-corrected LABF-STEM Image of Interfacial Dislocation at GaSb/GaAs Interface with Corresponding RH/FS Burgers Circuit. (b) HAADF-STEM Image and Intensity Profile From HAADF-STEM Image of Dislocation Core Revealing Two Distinct Peaks (The One Corresponding to The Atom Centrally Located in The Defect Core is Marked by Arrow in The Inset). (c) Proposed Atomic Arrangement of Defect Core Overlaid on

Figure Page

HAADF-STEM Image. Dotted Line Shows Location of GaSb/GaAs Interface. 99

5.5 (a) Aberration-corrected LABF-STEM Structure Image of Interfacial Defect in The GaSb/GaAs Heterostructure with Corresponding RH/FS Burgers Circuit. (b) HAADF-STEM Image and Intensity Profile Obtained from HAADF-STEM Image Reveal Single Atomic Peak at Defect Core. (c) Proposed Atomic Arrangement of Defect Core Overlaid on HAADF-STEM Image....................100

5.6 Aberration-corrected HAADF-STEM Image of Dissociated 60° Dislocation at The GaSb/GaAs(001) Interface and Corresponding RH/FS Burgers Circuit. 102

CHAPTER 1

INTRODUCTION

1.1 Semiconductors

Semiconductors are materials with electrical conductivity much less than for metals but much more than for insulators. Semiconductors consist of elemental semiconductors, which are the group IV elements, and compound semiconductors, which are composed of two different elements, such as group III and group V, group II and group VI, and group IV with group VI. Silicon is the most widely used elemental semiconductor while gallium arsenide and gallium nitride are the two most commonly used compound semiconductors. Further, semiconductors can be alloyed to produce compound semiconductors (e.g., SiGe), ternary semiconductors (e.g., InGaAs), quaternary semiconductors (e.g., GaInAsSb) and even quinary semiconductors (e.g., GaInAsSbP).

Band-gap energy, E_G, is an important parameter for semiconductors. E_G is defined as the energy gap between the top of the valence band and the bottom of the conduction band. Semiconductor band-gaps can be classified as either direct or indirect depending on whether the maximum of the valence band and the minimum of the conduction band are at the same k-value, where k is the wavenumber [1]. The band-gaps of Si - an indirect band-gap semiconductor - and GaAs - a direct band-gap semiconductor - are 1.11 eV and 1.43 eV, respectively. Insulators have much wider band-gaps, typically in the range of 5.0 - 10 eV, while the valence and conduction bands in metals are partially overlapped.

There are very few electrons in the conduction band of a semiconductor at very low temperature. In response to external stimuli, such as electric field or light, it is possible to excite electrons from the valence band to the conduction band where they are free to move and conduct current. The conductivity of semiconductors can be greatly improved by doping with impurity atoms either by diffusion or ion implantation. Dopant atoms may contribute electrons to the conduction band to create *n*-type semiconductors. Conversely, *p*-type semiconductors are created when dopant atoms contribute holes to the valence band [1].

1.2 Semiconductor heterostructures

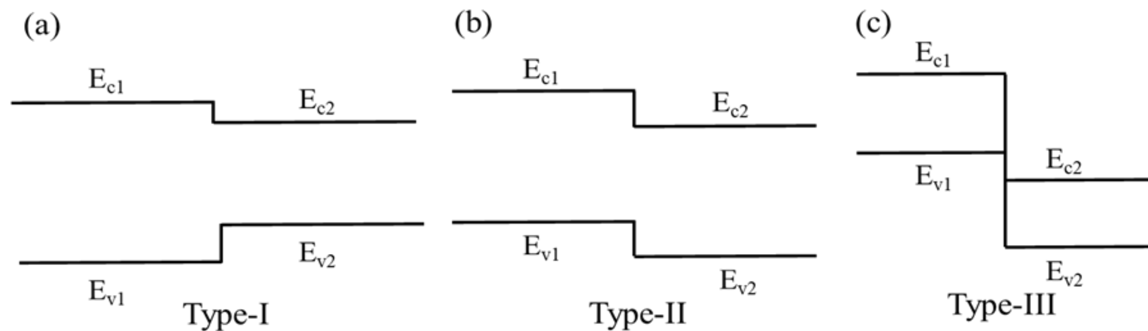

Fig. 1.1: Schematic diagram showing the three types of band alignment in undoped heterojunctions: (a) Type-I, (b) Type-II, and (c) Type-III heterostructures. E_{c1} and E_{c2} are the conduction-band edges and E_{v1} and E_{v2} are the valence-band edges of the two materials forming the heterojunction.

Semiconductor heterostructures are formed when two or more dissimilar semiconductor materials are combined. The materials interface in semiconductor heterostructures is known as a heterojunction, and can be classified as Type-I, Type-II or Type-III,

depending on the arrangement of bands across the heterointerface. The band arrangements in these three types of heterojunctions are illustrated in Fig. 1.1.

Type-I heterojunction: These heterojunctions are formed when the conduction-band and valence-band edges of the narrower band-gap material lie entirely within the band-gap of the wider band-gap material, i.e., $E_{c1} > E_{c2}$ and $E_{v1} < E_{v2}$. This type of heterostructure is known as a straddling-gap type-I heterostructure.

Type-II heterojunction: In the case of Type-II heterojunctions, the conduction-band and valence-band edges of one material are each lower than in the other material, i.e., $E_{c1} > E_{c2}$, $E_{v1} > E_{v2}$ and $E_{c2} > E_{v1}$. This type of heterostructure is known as a staggered-gap type-II heterostructure.

Type-III heterojunction: These heterojunctions are characterized by no overlap between the band-gaps of the two materials, i.e., $E_{c1} > E_{c2}$ and $E_{v1} > E_{c2}$. This type of heterojunction is known as a broken-gap type-III heterostructure.

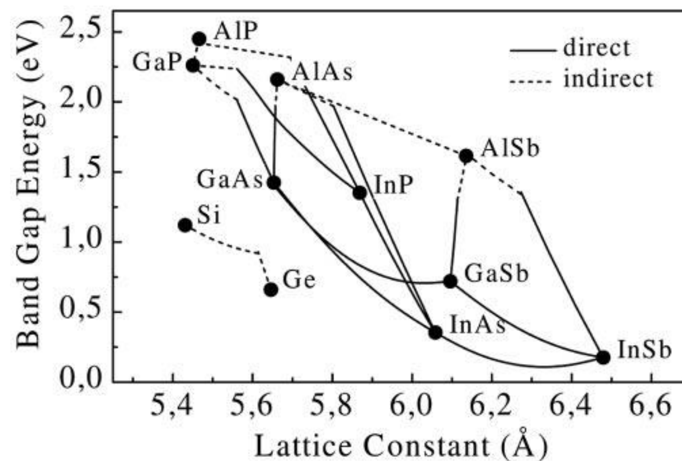

Fig. 1.2: Plot of band-gap energy vs. lattice constant for Si, Ge and common III-V semiconductors [2]

Semiconductor heterostructures are widely used for many optoelectronic applications such as multi-junction solar cells, lasers, and light-emitting diodes [3]. Figure 1.2 shows band-gap energy vs. lattice constant for Si, Ge and different III-V semiconductors. Combining materials with different band-gaps allows absorption of incident photons over a wider energy range, thus providing access to a broader range of wavelengths, which is advantageous for optical detectors and other optoelectronic devices. The feasibility of alloying compound semiconductors to produce ternary (eg.- $In_xGa_{1-x}As$) and quaternary (eg.- $In_xGa_{1-x}As_{1-y}P_y$) semiconductors opens up the option for a wider range of materials that can be combined [4]. However, differences in lattice constants between the film and the substrate will cause interfacial misfit strain, which can potentially introduce defects into the film layer and thus degrade device performance. In addition to the three basic types of heterostructures, more complex heterostructures such as double heterostructures (e.g., quantum wells, wires, and dots), superlattices, and modulation-doped heterostructures are increasingly being studied and used in device applications. The surface energies of the film and the substrate, as well as the interfacial energy, give rise to different growth modes, which are discussed in the following section.

1.3 Growth modes

The growth modes for epitaxial thin films on a substrate are three types [5]:

i) Frank-van der Merwe (FM) growth: FM or layer-by-layer growth, shown schematically in Fig. 1.3(a), occurs when $\gamma_A < \gamma_B + \gamma^*$, where γ_A is the surface energy of the substrate material A, γ_B is the surface energy of the film material B and γ^* is the

interfacial energy. In this case, the deposited atoms are more attracted to the substrate than they are to each other.

ii) Stranski-Krastanov (SK) growth: SK growth is characterized by an initial several monolayers of layer-by-layer growth followed by growth in the form of islands. In this mode, the interfacial energy increases as the layer thickness increases, which leads to a shift from layer-by-layer growth mode to the island growth mode, as shown in Fig. 1.3(b).

iii) Volmer-Weber (VW) growth: The VW or island growth occurs when $\gamma_A > \gamma_B + \gamma^*$. The deposited materials tend to cluster together, thus growing as separate islands. The VW growth mode is schematically depicted in Fig. 1.3(c).

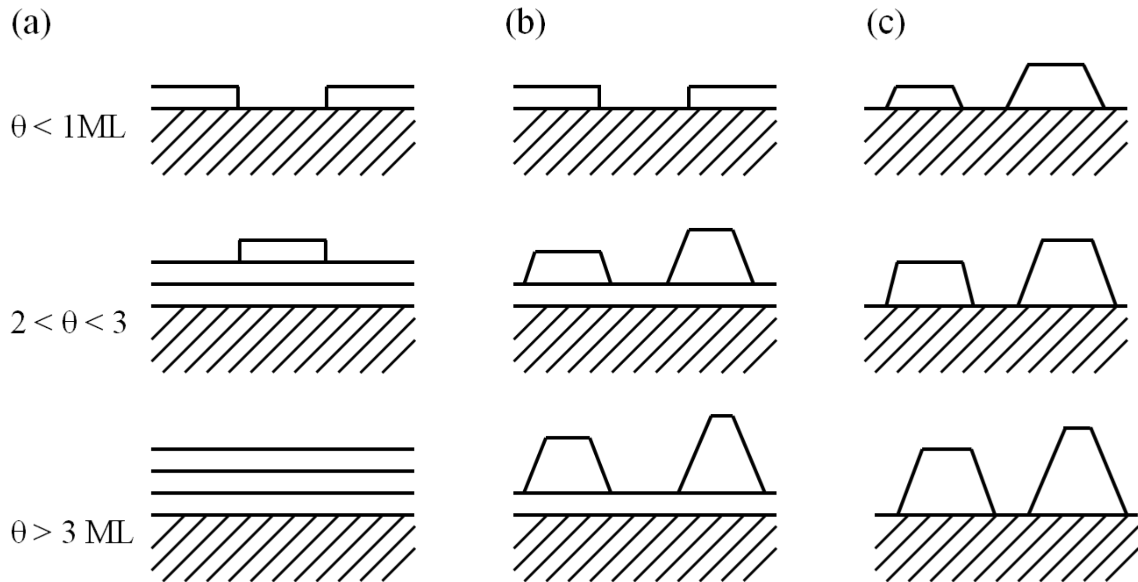

Fig. 1.3: Growth modes in epitaxial thin film growth - (a) FM layer-by-layer growth, (b) SK layer + island growth and (c) VW island growth. θ is the coverage expressed in monolayer (ML).

1.4 Strained layer epitaxy

Electronic devices require materials of the highest possible crystalline quality, which can be achieved by epitaxial growth of thin films on suitable substrates. Due to differences in lattice parameter as well as thermal expansion coefficients between films and substrate, misfit strain is invariably introduced at the film/substrate interface. Strain provides an extra degree of freedom to alter the band structure in semiconductor materials, since strain can change the band-gap energy [6]. Strain might cause a reduced valence-band density of states and reduction in Auger recombination process, which in turn lead to reduced threshold current densities in lasers [7]. However, the misfit strain often gives rise to line defects such as dislocations at the interface [8]. These dislocations might have dangling bonds at their cores, which may introduce deep-level energy states in the band gap [9]. Thus, dislocations may act as sites for electron-hole pair recombination and reduce minority carrier lifetimes [10]. The tolerable density of dislocations can be as low as 10^3 cm^{-2} in some minority-carrier devices [11].

A thorough understanding of defect creation and evolution in semiconductor heterostructures is essential in order to develop approaches to growth that result in defect densities within permissible limits. The following section describes different aspects of the dislocations that are generated during strain relaxation in heteroepitaxial systems. Both relaxation kinetics and electronic properties have been found to be dependent on atomic arrangements at the defect cores, which are described in a later section of this chapter.

1.5 Strain relaxation in epitaxially-grown lattice-mismatched heterostructures

1.5.1 Critical thickness

The misfit strain across an interface is considered to be bi-axial and can be expressed as:

$$\varepsilon = -\left(\frac{a_f - a_s}{a_s}\right) \tag{1.1}$$

where a_f and a_s are the lattice parameters of the film and the substrate, respectively.

Up to a certain thickness, the elastically-strained films can be grown pseudomorphically, thereby maintaining coherency with the underlying substrate. The elastic strain energy in the case of isotropic material can be expressed as [12]

$$E_e = 2\mu\left(\frac{1+\nu}{1-\nu}\right)\varepsilon^2 h \tag{1.2}$$

where μ and ε are shear modulus and misfit strain, respectively.

Dislocations serve to relieve misfit strain in the film, but they create distortions in the crystal and thus have associated strain energy. The elastic component of the strain energy of a mixed dislocation can be written as [13]:

$$E_d = \frac{\mu b^2(1-\nu cos^2\theta)}{4\pi(1-\nu)}\ln\left(\frac{R}{r}\right) \tag{1.3}$$

where ***b*** is the Burgers vector of the dislocation, θ is the angle between the Burgers vector and the line direction of the dislocation, R is the outer cut-off radius and r is the inner cut-off radius of elastic strain field associated with the dislocation.

Since the elastic strain energy caused by misfit strain at the interface is proportional to film thickness, a point is reached with increased film thickness where the elastic strain energy becomes sufficiently large to create interfacial misfit dislocations. This point marks the onset of strain relaxation in the film, and the corresponding thickness is usually called the critical thickness. Mathematically, the critical thickness can be determined by minimizing the total energy of the system (E_e+E_d) with respect to ε. However, this energy model of critical thickness does not take into account the Schmid factor, which describes the orientation of the glide plane relative to the applied stress direction, and is often an important consideration for 60° dislocations which lie in the {111} planes and glide to relieve misfit strain in low-mismatched heterostructures. Thus, a force model that includes the Schmid factor is normally used to determine the critical thickness in a material system where 60° dislocations are prevalent [12]. This critical thickness (h_c) is expressed as [4]:

$$h_c = \frac{b(1-\nu cos^2\theta)}{8\pi(1+\nu)\varepsilon cos\lambda} \ln\left(\frac{R}{r}\right) \tag{1.4}$$

where λ is the angle between the Burgers vector and the normal to the dislocation line direction at the interface.

1.5.2 Geometry and type of misfit dislocations

60° and 90° dislocations are the two main types of dislocations commonly observed in epitaxially-grown semiconductor heterostructures with films and substrates of either diamond-cubic or sphalerite crystal structure. These angles are the characteristic angle, θ, which is the angle between the Burgers vector and the dislocation line direction.

60° dislocations are prevalent in low-mismatched heterostructures when the misfit strain is less than ~1.5%, whereas 90° dislocations are most commonly created in high-mismatched heterostructures [12].

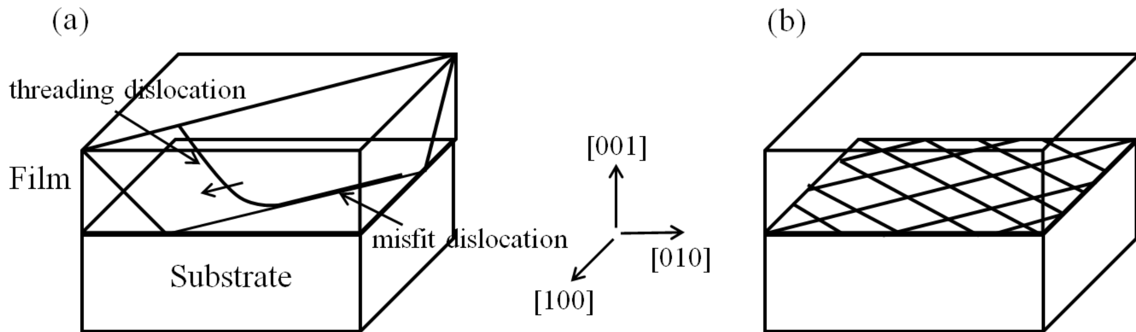

Fig. 1.4. Schematic description of: (a) 60° misfit dislocation formation by glide of threading dislocation segment, and (b) final network of misfit dislocations at the interface plane.

The mechanism for the formation of 60° dislocations in (001)-grown heterostructures is shown in Fig. 1.4(a). These dislocations lie on {111} planes which are the slip plane for diamond-cubic/sphalerite crystals. Thus, the threading segments can easily glide in the inclined {111} planes to create misfit dislocation segments at the interface plane. These {111} planes intersect the (001) interface plane along [110] and $[\bar{1}10]$ directions. Hence, misfit dislocations lie along the two <110> directions at the (001) interface plane. Figure 1.4(b) illustrates the final dislocation configuration after all the threading dislocations have escaped through the side-walls of the wafer. In reality, this might not happen - in which case the threading dislocations either escape through the film surface or they end on a misfit dislocation at the interface creating a dislocation loop. Although 60° dislocations have low formation energy and can easily propagate to relieve

misfit strain, they are only 50% effective in relieving the strain. This is because their Burgers vectors are inclined to the interface plane and only the in-plane edge components are effective in relaxing the bi-axial misfit strain.

Creation and propagation of 90° dislocations is not energetically favorable since these dislocations lie on the (001) plane which is not a low-Peierls-stress plane in semiconductors. However, these dislocations are fully effective in relieving misfit strain since their Burgers vector lies completely in the interface plane. They are primarily formed in high-mismatched systems.

In this dissertation research, the primary focus is on strain relaxation in low-mismatched heterostructures since the strain relaxation mechanisms were being investigated in $GaAs/GaAs_{1-x}Sb_x/GaAs$ materials that had a misfit strain of about 0.6%, and thus fall in the low-mismatch category.

1.5.3 Dislocation nucleation and interaction events in low-mismatched heterostructures

It has been experimentally observed that epitaxial films can be grown beyond the theoretical critical thickness up to a second critical thickness while not being measurably relieved [14]. This metastable regime of film growth is dependent on growth conditions [15], and is attributed to the sluggish kinetics of strain relaxation in the early stages of growth [16]. The two major factors that control the relaxation kinetics at this point are dislocation nucleation and mobility [16,17]. Dislocation nucleation is an important aspect of strain relaxation in lattice-mismatched systems, albeit poorly understood. There have been several proposals about possible dislocation sources in semiconductor heterostructures. Dislocations in the substrate are considered to be one of the primary

sources for grown-in threading dislocations [8]. However, the dislocation densities of films that have undergone only the early stages of relaxation are orders of magnitude larger than the typical dislocation densities for Si and GaAs substrates. Hence, grown-in threading dislocations cannot be the only source for these dislocations.

The homogeneous nucleation of dislocation half-loops at surfaces has been considered as a possible source of dislocations. These half-loops expand under the application of misfit stress and eventually reach the strained interface to create two threading dislocations that then move laterally in opposite directions to deposit misfit dislocations at the interface. However, theoretical calculations have shown that the energy required for homogeneous nucleation is 50-88 k_BT, which is available only in high-mismatched systems with misfit strains of greater than 5% [18]. However, heterogeneous nucleation of dislocation half-loops is plausible at surface steps [19] and other points of stress concentration caused by local fluctuations in composition in alloyed semiconductors [20], or trace impurities of Cu [21], even in low-mismatched heterostructures.

In addition to dislocation nucleation and multiplication, dislocation interaction events such as blocking and annihilation can play a major role in the strain relaxation process. Analytical [22] and numerical [23] studies of dislocation blocking, as well as experimental observations [24], have been reported. Dislocation blocking may occur as a result of long-range or short-range interactions between threading/threading or threading/misfit dislocations with parallel Burgers vectors. Dislocation blocking increases the number of threading dislocations in the film, which can be extremely deleterious for device performance.

Dislocation annihilation is commonly observed in high-mismatched heterostructures where the density of threading dislocations are orders of magnitude higher than for low-mismatched structures [25]. Threading dislocations having opposite Burgers vectors attract and eventually annihilate each other. However, due to the substantially lower dislocation density in low-mismatched heterostructures, dislocation annihilation may not be as effective. Thus, producing low-defect-density heterostructures by growing thicker epilayers such that considerable dislocation annihilation is achieved, which has been proven to be successful for high-mismatched heterostructures [26], may not be a viable option for low-mismatched heterostructures.

1.5.4 Asymmetric strain relaxation in low-mismatched heterostructures

Asymmetric distribution of misfit dislocations in the early stage of relaxation has been widely reported in compound semiconductor heterostructures [27-34]. The reasons for asymmetry have been argued to be the differences between nucleation barrier [35] and/or glide velocity [29] of the two types of 60° dislocations: α- and β-dislocations that have their extra half-planes terminated by group-V and group-III elements, respectively. In addition to the fundamental difference in the chemical nature of α and β-dislocation cores, deformation tests on bulk materials have been reported that the nature of doping and impurities may have large effects on dislocation velocity [36,37]. The general consensus is that the α-dislocations have higher velocity in undoped and *n*-type materials, whereas the β-dislocations have higher velocity in *p*-type materials [37]. However, it is well-known that deformation experiments tend to cause segregation of point defects and impurities along dislocation cores [38]. Hence, the mobility of the dislocations can be

substantially altered in the case of deformation experiments in comparison to crystal growth processes which are, on the other hand, are much cleaner.

There have been contradictory reports on whether the density of α-dislocations is higher than the density of β-dislocations at heterointerfaces. Some researchers reported that the density of dislocations along the $[110]$ direction is higher than the $[\bar{1}10]$ direction in InGaAs/GaAs heterostructures [28,29,31,35], while others observed the opposite trend [32,39]. Moreover, the reason for asymmetry is still debated. While Fox *et al*. argued that only the Peierls barrier to dislocation glide is different for the two types of dislocations [29], Fitzgerald *et al*. suggested that the nucleation barrier could also be different [35]. Thus, it can be concluded that the fundamental aspects of asymmetric strain relaxation in semiconductor heterostructures remain poorly understood.

1.6 Core structure of defects

The core structure of defects in semiconductors significantly influences the electronic and mechanical properties. Non-radiative recombination of electron-hole pairs at the defect core is a well-known phenomenon and is likely to be dependent on the specific core structure of the defect [40]. Thus, understanding the detailed core structure of defects is important. In this dissertation research, a primary focus has been on the core structure of 60° dislocations, which are the most common type of misfit dislocation found in low-mismatched heterostructures.

1.6.1 60° dislocations

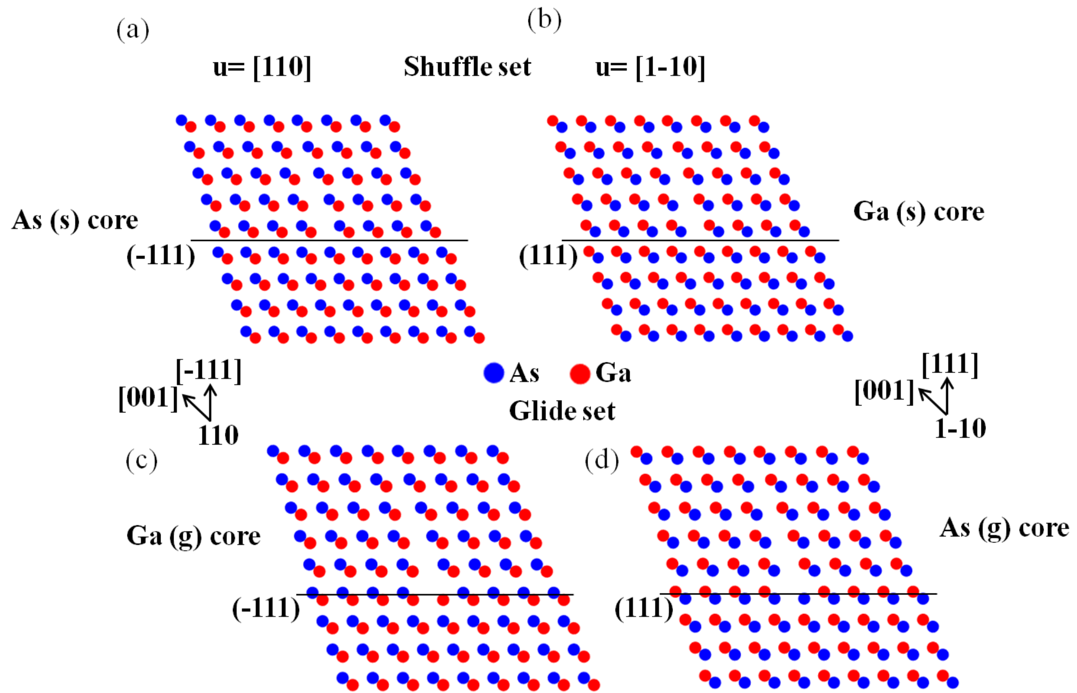

Fig. 1.5. (a) [110] and (b) [1$\bar{1}$0] projected structures of shuffle-set 60° negative dislocation showing extra half-planes that are terminated by As and Ga atoms, respectively; (c) [110] and (d) [1$\bar{1}$0] projected structures of glide-set 60° negative dislocation showing that the extra half-planes are terminated by Ga and As atoms, respectively.

In non-centrosymmetric crystals such as III-V and II-VI semiconductors, 60° dislocations are classified as α and β dislocations, based on the chemical nature of the dislocation core. In this dissertation it has been maintained that α-dislocations are terminated by group-V atoms and β-dislocations are terminated by group-III atoms. These dislocations have different mobility [29,41], and may be responsible for

asymmetric strain relaxation in (001)-grown heterostructures involving non-centrosymmetric materials [27,30,31,34]. The sign of the dislocation, and whether the dislocation belongs to glide set or shuffle set, determine the chemical nature of the core [28].

The two sub-lattices in diamond-cubic or zincblende semiconductors are shifted by $\boldsymbol{a}$/4[111] lattice vector, where $\boldsymbol{a}$ is the lattice parameter. Consequently, the {111} planes can be closely-spaced or widely-spaced. As shown by the horizontal black lines in Figs. 1.5(a) and (b), when shear happens between the widely-spaced {111} planes, the dislocation generated would belong to the shuffle set whereas glide-set dislocations are created by shear operation between two closely-spaced {111} planes, as indicated in Figs. 1.5(c) and (d) by the horizontal black lines.

Figure 1.5 illustrates the 110 and $1\bar{1}0$ projected structure of negative 60° glide-set and shuffle-set dislocations in GaAs. The dislocation line coincides with the projection direction. The extra half-plane is As-terminated in the shuffle-set dislocation in Fig. 1.5(a), which has a $[110]$ dislocation line. The shuffle-set dislocation with $[1\bar{1}0]$ dislocation line has Ga-terminated extra half-plane. The situation is reversed for a glide-set dislocation. As shown in Figs. 1.5(c) and (d), for dislocations with $[110]$ and $[1\bar{1}0]$ line directions, the dislocation cores contain Ga-terminated and As-terminated extra half-planes, respectively. Thus, for a negative dislocation, the α-dislocation (As-terminated core) would have $[1\bar{1}0]$ line direction if it is a glide-set dislocation but the α-dislocation would have $[110]$ line direction for a shuffle-set dislocation. Similarly, the β-dislocation (Ga-terminated core) would have $[110]$ or $[1\bar{1}0]$ line direction depending on whether it is a glide-set or shuffle-set dislocation. The line directions corresponding to α- and β-

dislocations are reversed in the case of positive 60° dislocations, which relieve misfit strain in tensile-strained films. For such dislocations, α-dislocations have $[110]$ or $[1\bar{1}0]$ line directions and β-dislocations have $[1\bar{1}0]$ or $[110]$ line directions, depending on whether they belong to glide set or shuffle set.

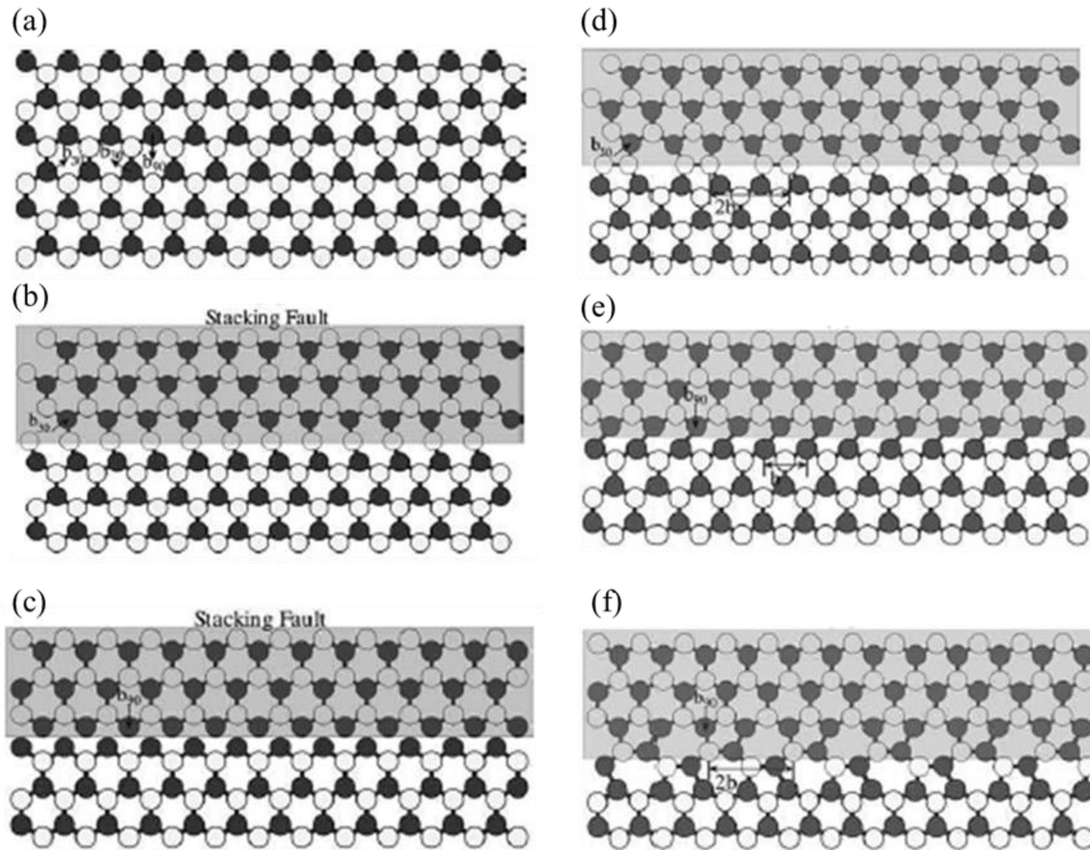

Fig. 1.6. [111] projected images of: (a) Perfect diamond crystal, (b) unreconstructed core of 30° partial, (c) unreconstructed core of 90° partial, (d) double-period reconstructed core of 30° partial, (e) single-period reconstructed core of 90° partial, and (f) double-period reconstructed core of 90° partial. The black and white atoms represent atomic layers that are just below and above the (111) glide plane [42].

Figure 1.6(a) shows two atomic layers below (black circles) and above (white circles) the (111) glide plane of a perfect diamond cubic lattice viewed in [111] projection. In the case of a sphalerite lattice, the atoms below and above the glide plane have different chemical elements. An intrinsic stacking fault can be introduced by shifting the black atoms into the centers of the unoccupied white triangles in three different ways, as indicated in Fig. 1.6(a). The angle between the shift direction and the line direction, which is the interface separating the shaded faulted region and the perfect crystal, determines the character of the partial dislocation. Hence, each {111}-type glide plane would have 30° partials of two possible Burgers vectors but a unique 90° partial that can generate an intrinsic stacking fault.

The core structure of the 30° partial dislocation is shown in Fig. 1.6(b). For sphalerite structures, the unreconstructed core of glide-set 30° partial is characterized by the absence of any wrong cation-cation/anion-anion bond in its core. An alternative reconstructed structure, distinguished by double-periodicity along the dislocation line, is shown in Fig. 1.6(c). *Ab initio* calculation has shown that this reconstructed core has significantly reduced core energy for silicon [43]. Figure 1.6(d) shows the core structure of an unreconstructed 90° partial in {111} projection. The dangling bonds at this core provide a strong driving force for reconstruction. Two possible configurations of reconstructed 90° partial have been identified: single-period (SP) and double-period (DP) reconstruction [44]. These are shown in Figs 1.6(e) and (f), respectively. The differences between the core energies corresponding to these two configurations is rather small, and thus there is a possibility of co-existence of both along the dislocation line of the 90° partial [42].

Interaction of point defects and impurities with dislocation core [45], and the presence of kinks and anti-phase defects along the core, can generate numerous atomic configurations of the dislocation core [46]. While many of these configurations are predicted by atomistic calculations, experimental evidence has hardly been reported. The most direct experimental technique to study the atomic structure of dislocation cores is high-resolution electron microscopy (HREM). However, experimental conditions including sample geometry as well as strain fields around the dislocation core, make this task extremely challenging [47,48].

1.6.2 Interaction of 60° dislocations

Dissociated 60° dislocations on intersecting glide planes may interact with each other to form Lomer-Cottrell locks and Hirth locks [49]. For both type of locks, the 30° partials react to form stair-rod dislocations, which are sessile in nature. Formation of such dislocations locks the motion of dislocations on their corresponding glide plane, and thereby contribute to work-hardening. In the case of Lomer-Cottrell locks, the two stacking faults meet at an acute angle (70.5°). The cores of the two reacting 30° partials have the same chemical configuration and are separated by a cation-anion pair. The resultant dislocation, namely a stair-rod dislocation, has a Burgers vector of $\boldsymbol{a}/6\langle 110\rangle$ type. In the case of Hirth lock dislocations, the intrinsic stacking faults meet at an obtuse angle (109.5°). Here, the reacting 30° partials have cores of dissimilar polarity and the resultant stair-rod dislocation has a Burgers vector of $\boldsymbol{a}/3[001]$-type [49]. Undissociated 60° dislocations on intersecting glide plane may interact to form Lomer edge dislocations

with compact core structure or they can reside as a pair of dislocations that are a few unit cells apart [50].

1.7 Outline of dissertation

This dissertation describes a comprehensive investigation of strain relaxation mechanisms and the characterization of defects created in GaAs(001)-based lattice-mismatched heterostructures grown by molecular beam epitaxy (MBE).

Chapter 2 introduces the experimental methods used to grow and characterize the samples investigated in this research. A brief description of the MBE growth method and the equipment used to grow the semiconductor heterostructures studied in this dissertation is provided. Transmission electron microscopy-based techniques including convergent beam electron diffraction, high-resolution transmission electron microscopy, and scanning transmission electron microscopy are described. Other characterization techniques such as X-ray diffraction and atomic-force microscopy (AFM) are also briefly introduced.

Chapter 3 reports a detailed investigation of strain relaxation mechanisms in GaAs/GaAsSb/GaAs heterostructures with GaAsSb film thicknesses in the range of 50 - 4000 nm. Defects formed at the heterointerfaces were characterized using the standard $g.b$ method in conventional TEM. Additionally, the surface morphology of the heterostructures was characterized using the AFM technique and correlated with misfit dislocation density at the GaAs cap/GaAsSb film interface.

Chapter 4 reports atomic-scale characterization of interfacial defects in low-mismatched semiconductor heterostructures using aberration-corrected scanning

transmission electron microscopy. The Burgers vectors of the dislocations were identified using Burgers circuit analysis. Possible dislocation reactions leading to dissociation and formation of junctions were proposed. The core structure of the Shockley partial dislocations in the HAADF-STEM images were compared with previously proposed phenomenological atomic structural models of these defects.

Chapter 5 describes atomic-scale characterization of interfacial defects in high-mismatched GaSb/GaAs(001) heterostructures. Contrast analysis of aberration-corrected HAADF-STEM images of interfacial dislocations such as Lomer dislocations, perfect and dissociated 60° dislocations was performed and compared with previously proposed and/or observed structural models in order to identify the core structure of these defects.

In Chapter 6, a summary of the results is provided, and important conclusions are described. Opportunities for future work are also discussed.

References

[1] D.A. Neaman, Semiconductor Physics and Devices: Basic Principles, fourth ed., McGraw-Hill, New York, 2003.

[2] A.W. Bett, F. Dimroth, G. Stollwerck, O. V. Sulima, Appl. Phys. A Mater. Sci. Process. 69 (1999) 119–129.

[3] F. Capasso, Science 235 (1987) 172–176.

[4] C.S. Schnohr, Appl. Phys. Rev. 2 (2015) 031304.

[5] J.A. Venables, Introduction to Surface and Thin Film Processes, second ed., Cambridge University Press, 2000.

[6] C.P. Kuo, S.K. Vong, R.M. Cohen, G.B. Stringfellow, J. Appl. Phys. 57 (1985) 5428– 5432.

[7] H. Morkoç, B. Sverdlov, G.B. Gao, Proc. IEEE 81 (1993) 493–556.

[8] J.W. Matthews, S. Mader, T.B. Light, J. Appl. Phys. 41 (1970) 3800–3804.

[9] W.T. Read, Jr., Philos. Mag. 45 (1954) 775–796.

[10] A.D. Krnttz, S.A. Kulrn, A.L. Avernacht, Phys. Rev. 101 (1956).

[11] R. Hull, J.C. Bean, Crit. Rev. Solid State Mater. Sci. 17 (1992) 507–546.

[12] E.A. Fitzgerald, Mater. Sci. Reports 7 (1991) 87–140.

[13] J. P. Hirth, J. Lothe, Theory of Dislocations, second ed., Wiley, New York, 1982.

[14] J.C. Bean, T.T. Sheng, L.C. Feldman, A.T. Fiory, R.T. Lynch, Appl. Phys. Lett. 44 (1984) 102–104.

[15] J.Y. Tsao, B.W. Dodson, Appl. Phys. Lett. 53 (1988) 848–850.

[16] B.W. Dodson, J.Y. Tsao, Appl. Phys. Lett. 51 (1987) 1325–1327.

[17] D.C. Houghton, J. Appl. Phys. 70 (1991) 2136–2151.

[18] D.J. Eaglesham, E.P. Kvam, D.M. Maher, C.J. Humphreys, D.J. Eaglesham, D.M. Maher, J.C. Bean, Philos. Mag. 59 (1989) 1059–1073.

[19] M. Albrecht, S. Christiansen, J. Michler, W. Dorsch, H.P. Strunk, P.O. Hansson, E. Bauser, Appl. Phys. Lett. 67 (1995) 1232.

[20] R. Hull, J.C. Bean, J. Vac. Sci. Technol. A 7 (1989) 2580– 2585.

[21] V. Higgs, P. Kightley, P.J. Goodhew, P.D. Augustus, Appl. Phys. Lett. 59 (1991) 829–831.

[22] L.B. Freund, J. Appl. Phys. 68 (1990) 2073–2080.

[23] K.W. Schwarz, Phys. Rev. Lett. 78 (1997) 4785–4788.

[24] E.A. Stach, K.W. Schwarz, R. Hull, F.M. Ross, R.M. Tromp, Phys. Rev. Lett. 84 (2000) 947–950.

[25] E.A. Fitzgerald, phys. stat. sol. (a) 171 (1999) 227–238.

[26] P. Sheldon, K.M. Jones, M.M. Al-Jassim, B.G. Yacobi, J. Appl. Phys. 63 (1988) 5609–5611.

[27] K.L. Kavanagh, M.A. Capano, L.W. Hobbs, J.C. Barbour, P.M.J. Marée, W. Schaff, J.W. Mayer, D. Pettit, J.M. Woodall, J.A. Stroscio, R.M. Feenstra, J. Appl. Phys. 64 (1988) 4843–4852.

[28] M. Grundmann, U. Lienert, D. Bimberg, A. Fischer-Colbrie, J.N. Miller, Appl. Phys. Lett. 55 (1989) 1765–1767.

[29] B.A. Fox, W.A. Jesser, J. Appl. Phys. 68 (1990) 2739–2746.

[30] R.S. Goldman, K.L. Kavanagh, H.H. Wieder, S.N. Ehrlich, R.M. Feenstra, J. Appl. Phys. 83 (1998) 5137–5149.

[31] O. Yastrubchak, T. Wosiński, J.Z. Domagała, E. Łusakowska, T. Figielski, B. Pécz, and A.L. Tóth, J. Phys. Condens. Matter 16 (2004) S1–S8.

[32] L. Gelczuk, D. Pucicki, J. Serafińczuk, M. Dąbrowska-Szata, P. Dłuzewski, J. Cryst. Growth 430 (2015) 14–20.

[33] L. Gelczuk, J. Serafisiczuk, Mater. Sci. 26 (2008) 157.

[34] E.A. Fitzgerald, G.P. Watson, R.E. Proano, D.G. Ast, P.D. Kirchner, G.D. Pettit, J.M. Woodall, J. Appl. Phys. 65 (1989) 2220–2237.

[35] H. Teichler, Jpn. J. Appl. Phys. 16 (1977) 737-745.

[36] I. Yonenaga, K. Sumino, J. Cryst. Growth 126 (1993) 19–29.

[37] I. Yonenaga, K. Sumino, J. Appl. Phys. 65 (1989) 85–92.

[38] M.J. Matragrano, D.G. Ast, J.R. Shealy, V. Krishnamoorthy, J. Appl. Phys. 79 (1996) 8371–8378.

[39] P.M. Petroff, R.A. Logan, A. Savage, Phys. Rev. Lett. 44 (1980) 287–291.

[40] M.S. Abrahams, J. Blanc, C.J. Buiocchi, Appl. Phys. Lett. 21 (1972) 185–186.

[41] E.A. Fitzgerald, D.G. Ast, P.D. Kirchner, G.D. Pettit, J.M. Woodall, J. Appl. Phys. 63 (1988) 693–703.

[42] F.R.N. Nabarro, T. Mura, Dislocations in Solids: Other Effects of Dislocations: Disclinations (Vol. 5), 1981.

[43] V. V. Bulatov, J.F. Justo, W. Cai, S. Yip, A.S. Argon, T. Lenosky, M. De Koning, T. Diaz de la Rubia, Philos. Mag. A 81 (2001) 1257–1281.

[44] J. Bennetto, R.W. Nunes, D. Vanderbilt, Phys. Rev. Lett. 849 (1997) 1–4.

[45] X. Xu, S.P. Beckman, P. Specht, E.R. Weber, D.C. Chrzan, R.P. Erni, I. Arslan, N. Browning, A. Bleloch, C. Kisielowski, Phys. Rev. Lett. 95 (2005) 1–4.

[46] V. V. Bulatov, Scr. Mater. 45 (2001) 1247–1252.

[47] P. Hirsch, D. Cockayne, J. Spence, M. Whelan, Philos. Mag. 86 (2006) 4519–4528.

[48] J. Spence, C. Koch, Scr. Mater. 45 (2001) 1273–1278.

[49] T. Paulauskas, C. Buurma, E. Colegrove, B. Stafford, Z. Guo, M.K.Y. Chan, C. Sun, M.J. Kim, S. Sivananthan, R.F. Klie, Acta Crystallogr. Sect. A Found. Adv. 70 (2014) 524–531.

[50] J. Narayan, S. Sharan, Mater. Sci. Eng. B 10 (1991) 261–267.

CHAPTER 2

EXPERIMENTAL METHODS

This chapter provides a brief description of the experimental techniques that were used to grow and characterize the semiconductor heterostructures that were studied in this dissertation. These heterostructures were grown using the technique of molecular beam epitaxy (MBE) and were characterized using transmission electron microscopy (TEM) as well as high-resolution x-ray diffraction (HR-XRD) and atomic force microscopy (AFM). Conventional TEM was used for bright-field imaging of plan-view and cross-sectional samples, and also for recording convergent beam electron diffraction patterns. Aberration-corrected scanning transmission electron microscopy was used for atomic-scale imaging of defect cores. Samples for TEM observation were prepared using polishing, dimpling and argon-ion milling at liquid nitrogen temperature.

2.1 Molecular beam epitaxy

Molecular beam epitaxy (MBE) is a technique used to grow epitaxial films by impinging thermal beams of molecules onto heated substrates under ultra-high vacuum conditions. MBE is employed to grow a wide range of materials, including semiconductors, oxides and metals. Despite the fact that growth rate in MBE is comparatively slow, typically about 1 μm/hr, its capability of producing abrupt interfaces and precise doping profiles makes MBE an ideal approach to realize many unique types of semiconductor structures, such as quantum wells, superlattices, and modulation-doped heterostructures [1].

The GaAs(001)-based heterostructures studied in this research were grown using a Veeco Applied Epi Mod Gen III, which is a solid-source MBE system. The Group-V materials such as As, Sb and P were injected through cracker tubes, whereas the Group-III materials were evaporated in Knudsen effusion cells. The substrates were rotated using a continual azimuthal-rotation (CAR) unit to ensure uniform growth. A flux monitor was used to measure the beam flux, which was controlled by opening the cracker valve for the Group-V materials, and by changing the effusion cell temperatures and controlling mechanical shutters in the case of group-III materials. The system was equipped with a residual gas analyzer (RGA) and reflection-high-energy electron diffraction (RHEED) for *in situ* monitoring during growth. The RGA provided information about the presence of any impurities in the growth chamber, while RHEED was used to monitor deoxidation, surface reconstruction and growth-rate calibration.

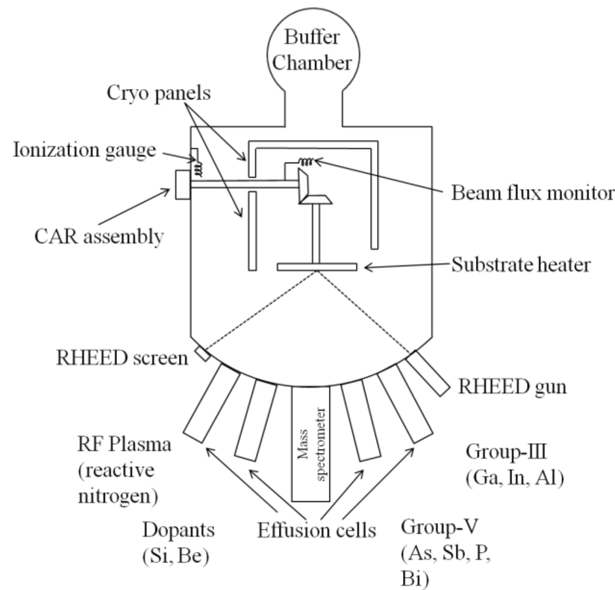

Fig. 2.1. Schematic of MBE system used for growing the semiconductor heterostructures investigated in this study.

The substrate surfaces were initially deoxidized for 15 minutes at elevated temperature. Subsequently, 300-nm-thick GaAs buffer layers were grown at substrate temperatures of 600 °C. The III-V epilayers were typically grown at 500 °C at growth rates of 0.72 μm/hr. The V/III equivalent beam pressure ratio used was 15. Finally, 50-nm-thick GaAs capping layers were usually deposited on the epilayers at ~ 600 °C.

2.2 X-ray diffraction

X-ray diffraction (XRD) is widely used to characterize different aspects of thin epitaxial films deposited on thick substrates [2]. In this research, the high-resolution x-ray diffraction (HR-XRD) technique was used to evaluate epilayer quality and to determine film composition and the extent of strain relaxation. The XRD scans were collected using a PANalytical X'Pert PRO MRD machine. ω-2θ double-crystal scans were typically recorded in the vicinity of (004) reflections to obtain lattice parameters of the epitaxial films. Vegard's law was then used to calculate the film compositions. Triple-crystal ω-rocking curves were often recorded to gain qualitative understanding of any relaxation in the films. Strain relaxation in the epilayers was quantified using high-resolution reciprocal-space maps recorded under asymmetric (224) diffraction conditions.

2.3 Transmission electron microscopy

Transmission electron microscopy (TEM) is a characterization technique widely used for imaging many types of physical and biological materials, as well as for obtaining analytical information using suitable spectrometers. Ruska built the first electron microscope in the early 1930s [3], with a resolution of ~10 nm. Electron microscopy has since come a long way in terms of improved resolution. Aberration correction in the late

1990s helped bring about the realization of sub-Ångstrom resolution in the electron microscope [4,5], making it possible to routinely obtain atomic-resolution images of many diverse types of materials.

In TEM, the electron beam interacts with a thin electron-transparent sample, and transmitted electrons are used to form amplitude-contrast, phase-contrast and mass-thickness contrast images. Amplitude-contrast images are formed by selecting either the direct beam or one of the Bragg-diffracted beams using a small objective aperture. Phase-contrast high-resolution TEM (HRTEM) images, on the other hand, are formed using a large objective aperture that encompasses multiple diffracted beams as well as the central beam. Both amplitude-and phase-contrast TEM imaging require a parallel beam configuration. Conversely, scanning transmission electron microscopy (STEM) images are formed by rastering a focused electron probe across the sample. The high-angle annular-dark-field (HAADF) imaging mode in the STEM uses elastically-scattered electrons to form an image. The image intensities in HAADF images are proportional to Z^{α}, where Z is the atomic number and α is typically in the range of 1.6 to 1.9 [6]. Due to the predominantly incoherent nature of the image, image interpretation of the HAADF-STEM images is relatively straightforward with no contrast reversals with either defocus or specimen thickness. This is a great advantage over HRTEM images, which undergo contrast reversals with changes in defocus and/or specimen thickness, so that detailed image interpretation should be supplemented by image simulations. Recent advances in aberration correction have enabled formation of high-intensity finely-focused electron probes that allow routine production of sub-Ångstrom resolution STEM images [7]. Both HAADF and large-angle bright-field (LABF) STEM imaging enable individual atomic

columns in compound semiconductors to be resolved in low-index zone axes projections [8]. In addition, HAADF-STEM imaging can be combined with electron-energy-loss spectroscopy (EELS) and energy-dispersive X-ray spectroscopy (EDXS) to obtain simultaneous chemical information at high spatial resolution.

In this dissertation research, conventional transmission electron microscopy (CTEM) was mostly carried out using a Philips-FEI CM-200 FEG TEM operated at 200 keV. This microscope had an interpretable resolution limit of ~2.5 Å. Aberration-corrected electron microscopy was carried out using a probe-corrected JEOL ARM-200F microscope which had an instrumental resolution of ~0.8 Å when operated at 200 keV. The probe convergence angle was ~22 mrad and the inner and outer detector collection angles for HAADF-STEM imaging were 90 and 150 mrad, respectively. The LABF images were typically recorded with collection angles of 0~20 mrad.

2.3.1 Convergent beam electron diffraction (CBED)

Convergent beam electron diffraction (CBED) patterns are obtained by focusing the electron beam onto small sample areas. CBED patterns are rich in crystallographic information and can therefore be used for determination of point groups and space groups, thickness measurement, lattice strain measurement, defect characterization, and determination of structure factor and charge density [9]. The recent development of pixelated direct electron detectors has made recording and storage of CBED patterns possible at every pixel of 2D STEM images, thereby generating 4D-STEM datasets that can be used for diverse applications such as phase, strain and

orientation mapping, thickness measurement, differential phase-contrast imaging, and ptychography [10].

In this dissertation research, the CBED technique was used in TEM mode to determine sample crystal polarity. The CBED patterns were obtained from GaAs substrate in <110> zone-axis orientation by using a condenser aperture that was small enough to avoid overlap between diffraction discs. These experimental <110> zone-axis CBED patterns were then matched with simulated CBED patterns to determine the crystal polarity. The CBED simulations were carried out using JEMS, which is a commercial software package widely used for CBED, HRTEM and HRSTEM simulation [11].

2.3.2 Imaging

In these studies, bright-field images were recorded in either [001] plan-view and <110> cross-sectional geometries. For ***g.b*** Burgers circuit analysis, samples were usually tilted to obtain two-beam diffraction conditions with <220> beams excited. This imaging condition was ideal for identifying the Burgers vectors of dislocations by exploiting strain contrast from the dislocation lines. Additionally, high-resolution TEM (HRTEM) was carried out to visualize the defect structures in greater detail. HRTEM is a phase-contrast technique that relies on interference between diffracted beams transmitted by the sample. HRTEM images should, in general, be regarded as lattice fringe images, since the fringe positions may not correspond to atomic positions. Moreover, the resolution needed for unravelling dislocation core structures of interest in this dissertation is well beyond the interpretable resolution of the non-aberration-corrected CM-200 microscope. Hence,

interpretation of HRTEM images of dislocation cores must be accompanied by image simulations with experimental input such as defocus, spherical aberration co-efficient, and sample thickness [12,13]. The latest generation of aberration-corrected STEM images can however routinely produce images with sub-Ångstrom resolution. Thus, details of the dislocation core structures were investigated using aberration-corrected HAADF and LABF STEM imaging, as described in the following chapters.

2.4 Sample preparation for TEM

TEM samples in either plan-view or cross-sectional orientations, were prepared by conventional polishing, dimpling and argon-ion milling with the specimen held at liquid-nitrogen temperature to avoid image artefacts produced by ion irradiation. Cleaved semiconductor samples were typically cut in ~2×1 mm^2 size using a diamond blade. For cross-sectional sample preparation, two samples were then glued face-to-face using M-bond epoxy adhesive and cured in an oven at about 95°C for more than 2 hours. The cured sample was then attached to a glass stub using wax for polishing and dimpling. Diamond lapping films were used to polish the samples down to thicknesses of ~80-100 μm, followed by dimpling, which was carried out using a cloth wheel to thin the sample to 5-15 μm. A copper washer ring was then glued to the four corners of the sample, which was then cured in an oven. The sample was subsequently removed from the glass stub by dissolving the wax with acetone. The next step was argon-ion milling, which was mostly performed using a Gatan PIPS 691 model with the sample held at liquid-nitrogen temperature. The guns were tilted at 7° and the dual-beam mode was used for milling. The energy used was usually 2.5-2.7 keV. The milling operation was normally stopped when an elliptical hole appeared near the center of the sample. Finally, a cleaning

operation was usually performed using 2-keV argon ions. Plan-view samples were prepared using a similar method, with the only difference being that no glue was required, and the cut samples were polished, dimpled and ion-milled from the substrate side only.

2.5 Atomic Force Microscopy (AFM)

Atomic force microscopy is a type of scanning probe microscopy where a tip, attached to the free end of a cantilever, is rastered across the sample surface [14]. The force between the tip and the surface profile is measured by tracking the cantilever deflection. This deflection is tracked by reflecting a laser beam off the cantilever onto a position-sensitive photodetector. Subsequently, an image showing the sample surface topography is obtained. A Bruker Multimode 8 AFM operated in tapping mode was used to generate images of the sample surfaces. Typically, the sample surface was rastered at an angle of 45° to reveal the cross-hatch surface morphology.

References

[1] J.Y. Tsao, Materials Fundamentals of Molecular Beam Epitaxy, first ed., Academic Press, Inc., California, 2012.

[2] P.F. Fewster, N.L. Andrew, J. Appl. Phys. 74 (1993) 3121–3125.

[3] P.W. Hawkes, Phys. Today 43 (1990) 84–85.

[4] M. Haider, H. Rose, S. Uhlemann, B. Kabius, K. Urban, J. Electron Microsc. 47 (1998) 395–405.

[5] O.L. Krivanek, N. Dellby, A.R. Lupini, Ultramicroscopy 78 (1999) 1–11.

[6] P. Hartel, H. Rose, C. Dinges, Ultramicroscopy 63 (1996) 93–114.

[7] D.J. Smith, Microsc. Microanal. (2008) 2–15.

[8] T. Aoki, J. Lu, M.R. McCartney, D.J. Smith, Semicond. Sci. Technol. 31 (2016) 094002.

[9] M. Tanaka, K. Tsuda, J. Electron Microsc. (Tokyo). 60 (2011) 245–267.

[10] C. Ophus, Microsc. Microanal. (2019) 563–582.

[11] P.A. Stadelmann, Ultramicroscopy 21 (1987) 131–145.

[12] A. Olsen, J.C.H. Spence, Philos. Mag. A 43 (1981) 945–965.

[13] P. Lu, D.J. Smith, Philos. Mag. B 62 (1990) 435–450.

[14] F.J. Giessibl, Rev. Mod. Phys. 75 (2003) 949–983.

CHAPTER 3

STRAIN RELAXATION IN LOW-MISMATCHED $GaAs/GaAs_{1-X}Sb_X/GaAs$ HETEROSTRUCTURES

3.1 Introduction and Motivation

GaAs/GaAsSb/GaAs quantum well structures are attracting interest for long-wavelength optoelectronic device applications [1]. Band structure calculations have shown that the type of band alignment depends on whether the GaAsSb layer is pseudomorphic or fully relaxed [2]. Moreover, the defects created as a result of strain relaxation in these heterostructures, which act as non-radiative recombination centers for electron-hole pairs, can seriously degrade device performance. Strain relaxation in epitaxial semiconductor heterostructures has been studied thoroughly over the last few decades [3-10]. Strain relaxation in the SiGe/Si system is most thoroughly investigated, while strain relaxation in the InGaAs/GaAs system is well examined amongst III-V semiconductor heterostructures [11-14]. However, very few studies have focused on strain relaxation in GaAsSb/GaAs heterostructures [15,16]. In this chapter, GaAs/GaAsSb/GaAs heterostructures with different GaAsSb film thicknesses have been investigated for the primary purpose of understanding strain relaxation in epitaxially-grown low-mismatched semiconductor heterostructures as a function of film thickness.

The creation of structural defects in low-mismatched heterostructures of GaAs/GaAsSb/GaAs(001) (Sb content ~ 8%) and their evolution during strain relaxation in thicker films were studied using TEM as well as HRXRD and AFM. Epitaxial growth

and HRXRD characterization were carried out by our collaborators Aymeric Maros and Nikolai Faleev. Results emerging from this study have been published [17].

3.2 Experimental Details

All epilayers were grown by molecular beam epitaxy (MBE) on GaAs(001) substrates. The substrate surfaces were initially deoxidized for 15 minutes at elevated temperature. Subsequently, a 300-nm-thick GaAs buffer layer was grown at 600 °C. The GaAsSb epilayers were grown at 500 °C at a growth rate of 0.72 μm/hr. The V/III equivalent beam pressure ratio used was 15. Finally, 50-nm-thick GaAs capping layers were grown on top of the epilayers at ~ 600 °C. Figure 3.1 provides a schematic illustration (not to scale) of the sample geometry. More details of the samples studied are given in Table 3.1.

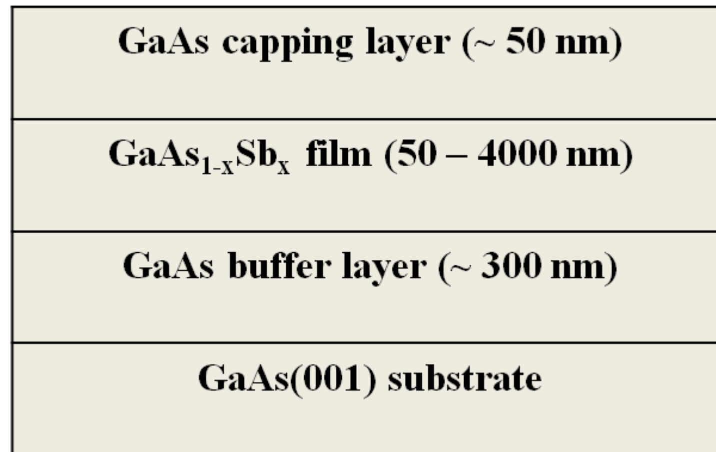

Fig. 3.1. Schematic cross-sectional illustration (not to scale) showing geometry of GaAs(cap)/$GaAs_{1-x}Sb_x$/GaAs (001) heterostructures.

Samples for TEM observation were prepared by conventional mechanical polishing, dimpling and argon ion-milling with the samples cooled to liquid nitrogen

temperature in order to minimize ion-beam-induced damage. Bright-field TEM images and convergent beam electron diffraction patterns were recorded with a Philips-FEI CM-200 microscope operated at 200 kV. A probe-corrected JEOL ARM-200F microscope operated at 200 kV was used to record aberration-corrected STEM images. The probe convergence angle was ~22 mrad, and the inner and outer collection angles for high-angle annular-dark-field (HAADF) STEM images were 90 and 150 mrad, respectively. A Bruker Multimode 8 instrument was operated in tapping mode to obtain the AFM images.

The misfit strain at the film/substrate interface was calculated as:

$$\varepsilon_{film/substrate} = -\left(\frac{a_f - a_s}{a_s}\right) \quad (1)$$

where a_f and a_s are the lattice parameters of the film and the substrate, respectively. The lattice parameters of the $GaAs_{1-x}Sb_x$ films were calculated using Vegard's law: $a_{GaAs_{1-x}Sb_x} = (1-x)a_{GaAs} + xa_{GaSb}$, where x is the Sb percentage in the film as measured by XRD. For samples other than A, B and C, the percentage strain relaxation values were obtained by reciprocal space mapping using XRD. The strain relaxation (γ) parameter is defined as:

$$\gamma = \frac{a'_f - a_s}{a_f - a_s} \quad (2)$$

Where a'_f is the lattice parameter of the relaxed film.

Table 3.1: Sample details

Sample	% Sb	Film thickness (nm)	Misfit strain at film/substrate interface (%)	% strain relaxation at film/substrate interface	Misfit strain at cap/film interface (%)
A	6.6	50	-0.52	-	-
B	9.4	50	-0.74	3	0.02
C	7.7	100	-0.6	4	0.02
D	7.1	250	-0.56	42	0.23
E	7.4	500	-0.58	68	0.39
F	8.7	1000	-0.68	75	0.51
G	8.3	2000	-0.65	81	0.52
H	8.6	4000	-0.63	92	0.57

For very small relaxation, as in Samples A, B and C, an approximate method of predicting relaxation by measuring misfit dislocation spacings in plan-view samples was adopted. Considering that 60° dislocations are primarily responsible for strain relaxation in the early stage of relaxation, the plastic strain can be written as:

$$\varepsilon_p = \frac{b}{2S} \quad (3)$$

where b is the Burgers vector of the 60° dislocation and S is the average spacing between dislocations.

The strain relaxation in Stage-I phase of relaxation can be calculated as:

$$\gamma = \frac{\varepsilon_p}{\varepsilon} \tag{4}$$

The misfit strain at the cap/film interface was calculated by taking into account the amount of relaxation in the GaAsSb film. The misfit strain at the cap/film interface can be expressed as:

$$\varepsilon_{cap/film} = -\left(\frac{\gamma(a_s - a_f)}{(1-\gamma)a_s + \gamma a_f}\right) \tag{5}$$

3.3 Results and Discussion

3.3.1 Strain relaxation stages at the film/substrate interface

Three different stages of strain relaxation are identified, as shown in Fig. 3.2, by plotting % relaxation in the film as a function of film thickness. Stage-I corresponds to an initial sluggish phase where the relaxation rate is very slow and the main rate-controlling factors are the nucleation and mobility of dislocations [8]. Samples A, B and C exhibit Stage-I relaxation. The density of misfit dislocations observed in plan-view TEM samples for Sample A was too small to calculate any meaningful strain relaxation. Hence, no relaxation data for this sample is included in Table 3.1 or Figure 3.2.

Rapid strain relaxation takes place in Stage-II. Samples D and E with 250- and 500-nm-thick GaAsSb films undergo Stage-II relaxation. Finally, the relaxation rate decreases reaching a saturation stage classified here as Stage-III relaxation. The extent of

strain relaxation in Samples F, G and H with 1000-, 2000- and 4000-nm-thick GaAsSb films corresponds to Stage-III relaxation. The defects generated at these different stages of strain relaxation are discussed in the following sections.

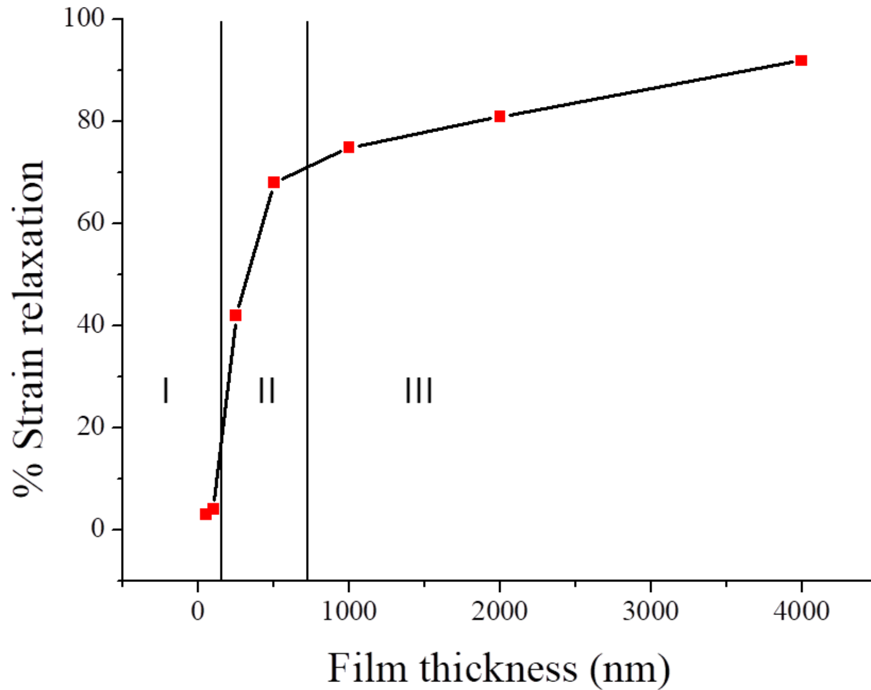

Fig. 3.2. Percentage of strain relaxation vs. film thickness showing three stages of strain relaxation in $GaAs_{1-x}Sb_x$/GaAs heterostructures.

3.3.2 Defects formed during Stage-I relaxation

Strong asymmetry in the distribution of misfit dislocations was observed in the early stage of strain relaxation. Figures 3.3(a) and (b) show plan-view bright-field TEM images of Samples B and C with 50-nm-thick and 100-nm-thick GaAsSb films, respectively. These images show the distribution of misfit dislocation lines at the film/substrate interface. The reason for the asymmetry in defect density is possibly due to

the different mobility of α- and β-dislocations along the orthogonal <110> directions [18] and/or due to the influence of local surface or interface morphology on dislocation nucleation and glide [19]. A more detailed discussion on the asymmetry of dislocation distribution is provided later in this chapter. Figures 3.3(c) and (d) show cross-sectional TEM images of Samples B and C, respectively. These films appear to be free of threading dislocations, although interfacial defects are visible in both cases.

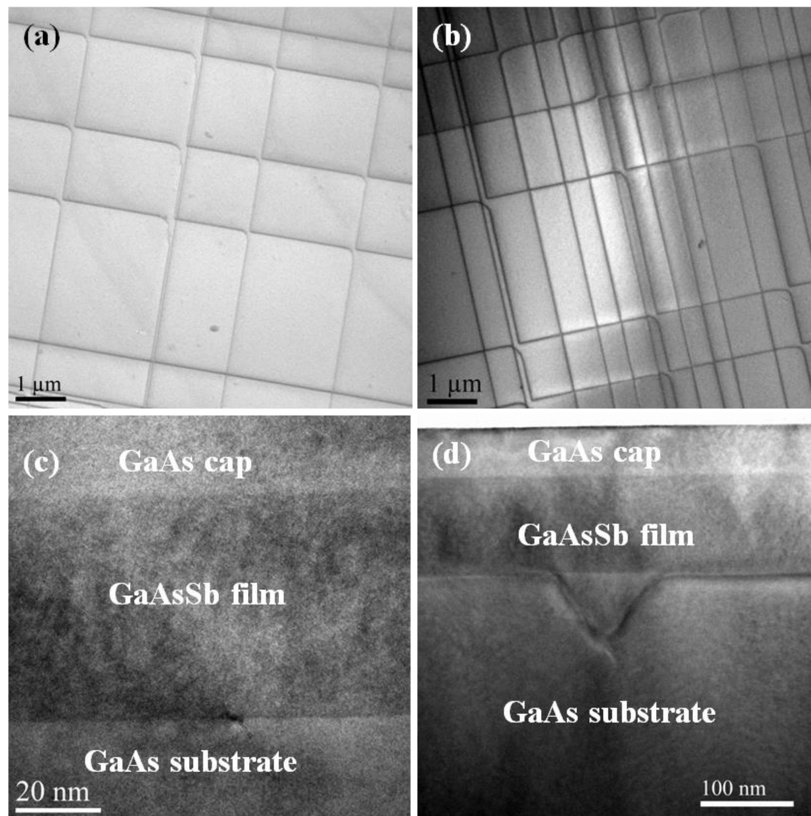

Fig. 3.3. Bright-field plan-view TEM images showing orthogonal network of misfit dislocations at the $GaAs_{1-x}Sb_x$/GaAs interface plane for: (a) Sample B, and (b) Sample C. Bright-field cross-sectional TEM images of: (c) Sample B, and (d) Sample C.

Table 3.2: Slip plane, Burgers vector and g.b/g.b×u contrast for two-beam conditions with excited $220/\bar{2}20$ reflection for 60° and 90° dislocations having $[110]/[\bar{1}10]$ dislocation line.

Dislocation line direction (***u***)	Dislocation type	Slip plane	Burgers vector (***b***)	***g.b/g.b×u***	
				220 reflection	$\bar{2}20$ reflection
$[110]$	60°	$(1\bar{1}1)$	$1/2[10\bar{1}]$	1/0	-1/-2
			$1/2[0\bar{1}\bar{1}]$	-1/0	-1/-2
		$(\bar{1}11)$	$1/2[0\bar{1}1]$	-1/0	-1/2
			$1/2[101]$	1/0	-1/2
	90°	(001)	$1/2[\bar{1}10]$	0/0	2/0
$[\bar{1}10]$	60°	(111)	$1/2[\bar{1}01]$	-1/-2	1/0
			$1/2[0\bar{1}1]$	-1/-2	-1/0
		$(\bar{1}\bar{1}1)$	$1/2[0\bar{1}\bar{1}]$	-1/2	-1/0
			$1/2[\bar{1}0\bar{1}]$	-1/2	1/0
	90°	(001)	$1/2[110]$	2/0	0/0

To identify the character of the misfit dislocations, standard ***g.b*** analysis was carried out with plan-view TEM samples. Two-beam imaging with either 220 or $\bar{2}20$

reflection excited was used to visualize strain contrast from dislocations lying at the heterointerface. The slip planes, Burgers vectors and ***g.b*** contrast for dislocations with dislocation line direction, ***u***=$[110]$ /$[\bar{1}10]$ for 60^0 mixed and 90^0 edge dislocations are listed in Table 3.2. Since both of these dislocations have edge components, the ***g.b ×u*** contrast must be taken into account when carrying out contrast analysis [20].

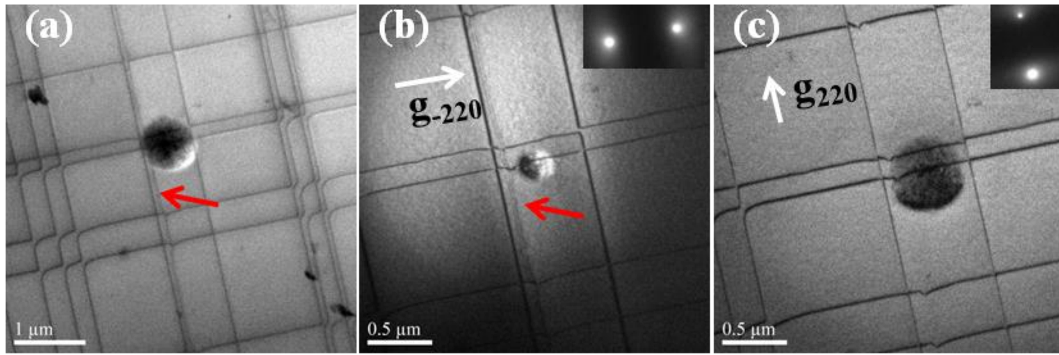

Fig. 3.4. $GaAs_{1-x}Sb_x$/GaAs interface plane in Sample C: (a) Bright-field plan-view TEM image, (b) Bright-field $g = \bar{2}20$ image; and (c) Bright-field $g = 220$ image.

The Burgers vectors of 90° dislocations lie completely in the (001) interface plane and are fully effective in relaxing misfit strain. Conversely, the Burgers vectors of 60° dislocations lie at 45° to the interface plane and are only 50% effective in relieving strain. The slip plane for 60° dislocations is $\{111\}$ type, which is also the widely-spaced and most favorable slip plane in sphalerite-type materials. Thus, the threading segment of 60° dislocations can easily glide on $\{111\}$ planes to create long misfit dislocation lines at the interface. Conversely, the slip plane for Lomer edge dislocations is (001) and the movement of 90° dislocations would then be difficult because of the high Peierls stress for glide in this plane.

Table 3.2 shows that 60° dislocations never become invisible under either of the two-beam imaging conditions used here, whereas the 90° dislocation goes out of contrast when the dislocation line is parallel to the reciprocal lattice vector of the active reflection. The types of dislocations visible in the plan-view TEM samples of heterostructures with 50 and 100-nm-thick GaAsSb films were identified by exploiting this feature.

Figure 3.4(a) shows a many-beam image recorded with the sample oriented along [001] zone-axis projection. All dislocations are visible in this imaging condition. Figures 3.4(b) and (c) show two-beam bright-field images with excited 220 and $\bar{2}20$ reflections, respectively. The majority of the dislocations in these images do not go out of contrast with either of the <220> beams excited, and show contrast that is characteristic of 60° dislocations. The dislocation line (marked by red arrow), which is visible with a $\bar{2}20$ strong beam but completely out of contrast with a 220 strong beam, was identified to have edge character. However, the two dark lines visible under the 220 excited-beam condition indicate that the dislocation could be dissociated. From Table 3.2, the strain contrast from pure edge dislocations must be stronger than from 60° dislocations that lie parallel to the reciprocal vector corresponding to the active reflection. However, the weaker strain contrast exhibited by the edge dislocations compared to that by 60° dislocations, as evident in Fig. 3.4(b), provides additional support that the dislocation could be split into partials. However, no stacking fault fringes were observed. Thus, no conclusion could be made about the Burgers vector of the edge dislocation. The dislocation lines corresponding to the 90° dislocation appear quite wavy whereas dislocation lines corresponding to the 60° dislocations adhere strictly to the <110> crystallographic directions.

3.4 Defects in Stage-II and Stage-III of strain relaxation

Figures 3.5(a) and (b) show networks of misfit dislocations on the (001) interface plane in heterostructures with 250-nm-thick and 500-nm thick GaAsSb films, respectively. Many curved dislocation lines deviating from orthogonal <110> directions are visible, suggesting that the overlapping strain fields of misfit dislocations cause changes in the local dislocation configuration in Stage-II of relaxation. In addition to dislocation loops, periodic banding of straight dislocation lines corresponding to 60° dislocations were also observed, most likely due to the regenerative nature of dislocation sources.

Figures 3.5(c) and (d) show cross-sectional TEM images of heterostructures with 250-nm-thick and 500-nm-thick GaAsSb films, respectively. Dislocation loops extend preferentially downwards into the buffer layer. Some dislocation loops lie along well-defined crystallographic directions emphasizing the importance of the Peierls barrier in determining the dislocation line direction in semiconductors. However, curved dislocation lines not adhering to any specific crystallographic directions were also observed. These dislocation lines seldom crossed the buffer layer/substrate interface, suggesting that this interface acted as a physical barrier to dislocation movement. The density of dislocation loops was higher in Sample E than in Sample D. This observation suggests that more and more curved dislocations are created as film relaxation progresses, and these extend into the substrate side of the interface, probably due to the repelling action of interfacial dislocations [21].

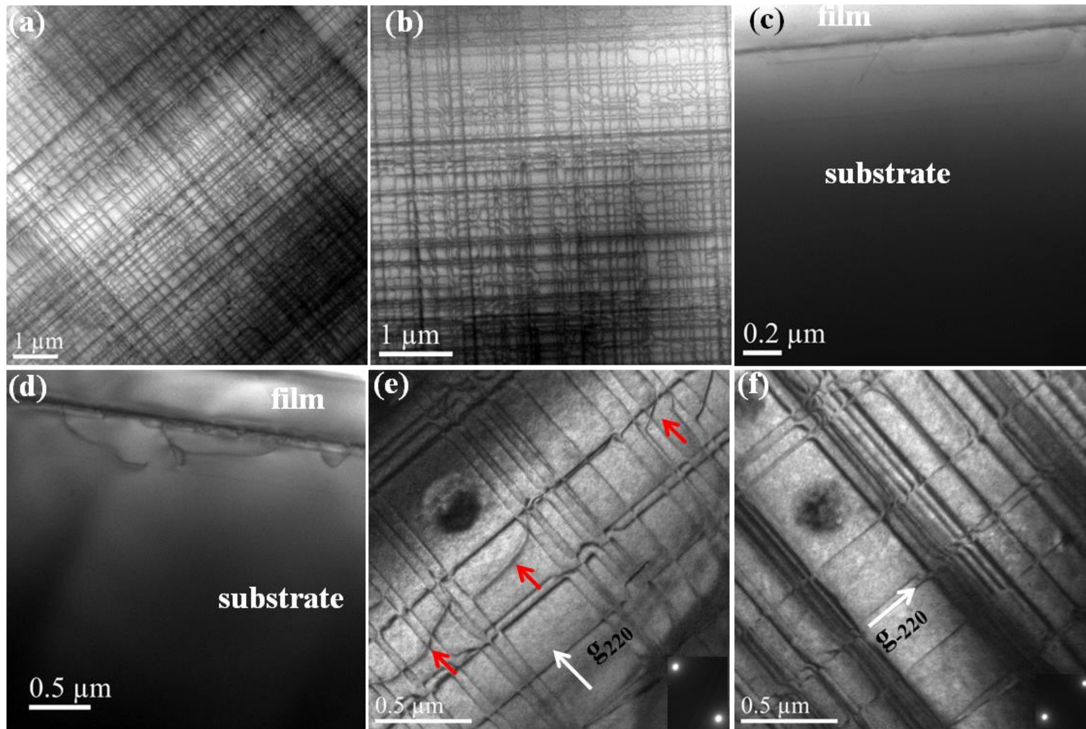

Fig. 3.5. Plan-view TEM images showing dislocation distribution at the interface plane of: (a) Sample D, and (b) Sample E. Bright-field cross-sectional TEM images of: (c) Sample D, and (d) Sample E. Bright-field two-beam plan-view images formed with: (e) $g = 220$, and (f) $g = \bar{2}20$ in Sample D.

Figures 3.5(e) and (f) show bright-field plan-view TEM images of Sample D recorded with 220 and $\bar{2}20$ reflections excited, respectively. The curved dislocations, marked by red arrows, are only visible with one of the active 220 reflections, and are completely out of contrast when the two-beam condition is set up by exciting the other 220 reflection. This contrast feature, as discussed in the previous section, indicates that these curved dislocations have edge character. It was also found previously that the majority of dislocation loops extending into the buffer layer in InGaAs/GaAs heterostructures were of edge character [12].

Dislocation loops extending into the buffer layer were also observed in Samples F, G and H, which had undergone Stage-III relaxation. Figures 3.6(a)-(c) show cross-sectional TEM images of Samples F, G and H. Threading dislocations were not observed in the cross-sectional TEM samples. Dislocation annihilation might be possible in Stage-III relaxation, as observed in high-mismatched heterostructures with thick films [22]. Plan-view TEM imaging could not be performed on these samples because the interface plane was buried too deep for observation with a TEM operated at 200 kV. From the limited specimen area visible in the cross-sectional samples, there was no noticeable difference in dislocation configuration for films with Stage-III relaxation compared with those with Stage-II relaxation. Thus, no conclusions could be made about whether or not dislocation annihilation had taken place in Samples F, G and H.

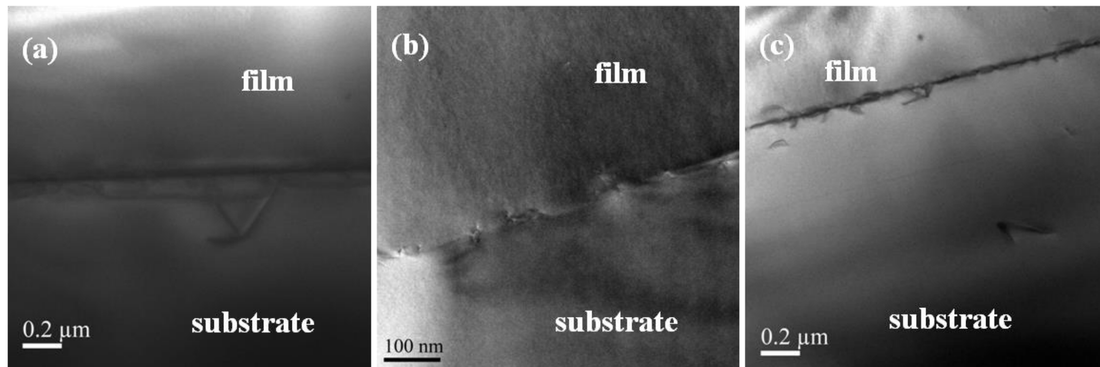

Fig. 3.6. Bright-field cross-sectional TEM images of (a) Sample F, (b) Sample G and (c) Sample H. Interfacial defects are present at GaAsSb/GaAs film/substrate interfaces. However, no threading dislocation is visible in any of the images.

3.5 Strain relaxation at the cap/film interface

Misfit dislocations present at the cap/film interface were observed in Samples E-H. Figures 3.7(a)-(d) show plan-view TEM images from regions that were thin enough to

exclude the bottom film/substrate interface from the field of view. The misfit dislocation lines were straight, strictly adhering to the <110> directions, and ***g.b*** contrast analysis confirmed that these were 60° dislocations. The long and well-separated chords of misfit dislocations indicate that Samples E-H have undergone Stage-I relaxation at the cap/film interface. Asymmetric strain relaxation, i.e., density of misfit dislocations along one <110> direction higher than in the other <110> direction, was exhibited at the cap/film interfaces in these samples.

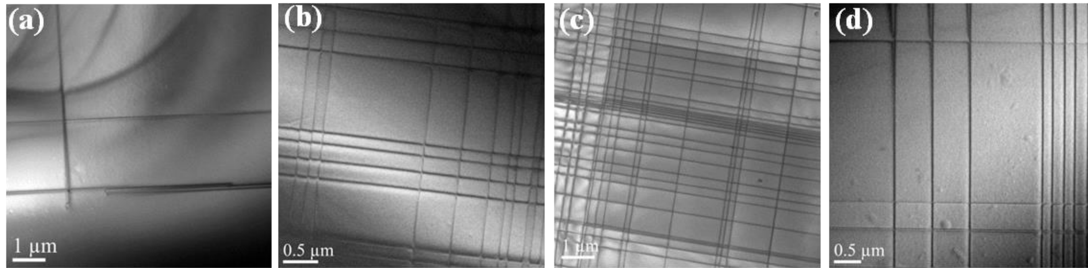

Fig. 3.7. Bright-field plan-view TEM images showing distribution of misfit dislocations at the cap/film interfaces of: (a) Sample E, (b) Sample F, (c) Sample G, and (d) Sample H.

3.6 Asymmetric dislocation distribution during Stage-I relaxation

Asymmetric distribution of misfit dislocations along the $[110]$ and $[1\bar{1}0]$ directions was observed at both the film/substrate and the cap/film interfaces in GaAs/GaAsSb/GaAs heterostructures. In order to quantitatively evaluate the asymmetry of dislocation distribution, a simple method to distinguish between $[110]$ and $[1\bar{1}0]$ directions in plan-view TEM samples was developed. Subsequently, it was possible to identify α- and β-type dislocations in plan-view TEM images. The distribution of α and

β-dislocations was studied at both compressively-strained film/substrate and tensile-strained cap/film interfaces in $GaAs/GaAs_{1-x}Sb_x/GaAs(001)$ heterostructures.

3.6.1 Distinguishing <110> directions in plan-view projection

In compound semiconductors with sphalerite structure such as GaAs, certain crystallographic planes are polar because of the two sublattices formed either by Ga or As atom, i.e., depending upon polarity, they will have either Ga-face or As-face. The crystal polarity in these non-centrosymmetric crystals was found to influence growth quality [23], dislocation mobility, etc. Several TEM techniques are available to determine crystal polarity. High-resolution transmission electron microscopy in conjunction with image simulation was used to determine polarity [24]. The HAADF imaging mode in the STEM produces images where the intensities of individual atomic columns are strongly proportional to atomic number Z, allowing for the possibility of polarity determination by comparing the relative intensities of well-resolved individual atomic columns [25]. However, in materials such as GaAs where the atomic numbers of the constituent atoms are close to each other, polarity determination by direct measurement of intensities of individual atomic columns might often not be possible because of intensity fluctuations caused by material factors such as presence of impurities, point defects, anti-site defects, etc. in the crystal and/or due to experimental issues such as variation of sample thickness across the field of view, etc. Alternatively, atomic-resolution spectroscopic techniques such as energy-dispersive x-ray spectroscopy or electron energy-loss spectroscopy may be used to determine polarity.

In this work, convergent beam electron diffraction (CBED) was used to determine crystal polarity. This technique allows examination of dynamical-diffraction-induced intensity patterns in CBED discs when the sample is sufficiently thick. Tafto and Spence [26] first demonstrated that multiple scattering involving higher-order odd-indexed reflections in <110> projection gave rise to constructive or destructive interference which was manifest as a white or black cross in (002) or $(00\bar{2})$ diffraction discs. Consequently, crystal polarity could be determined in the same projection. Lavagne *et al.* [27] used the Tafto-Spence method to determine polarity using plan-view <001> zone-axis CBED patterns collected from specimen areas that were thin enough to exclude the substrate. It was found that the observation of white or black crosses in (002) or $(00\bar{2})$ diffraction discs was not sufficient, and additional features in the transmitted disc had to be considered for unambiguous determination of polarity. In our case, the specimen geometry in [001] projection consisting of a strained GaAsSb layer sandwiched between a 50-nm GaAs capping-layer and a GaAs substrate would complicate interpretation of multiple scattering effects in the CBED discs. Thus, an alternative indirect route was taken to determine polarity in [001] projection. The procedure involves determination of the crystal polarity in <110> cross-sectional projection followed by careful sample cutting and sample loading in the TEM specimen holder to distinguish between the two <110> directions in [001] projection. Furthermore, polarity determination in cross-sectional samples is also helpful in identifying the chemical nature of the dislocation core.

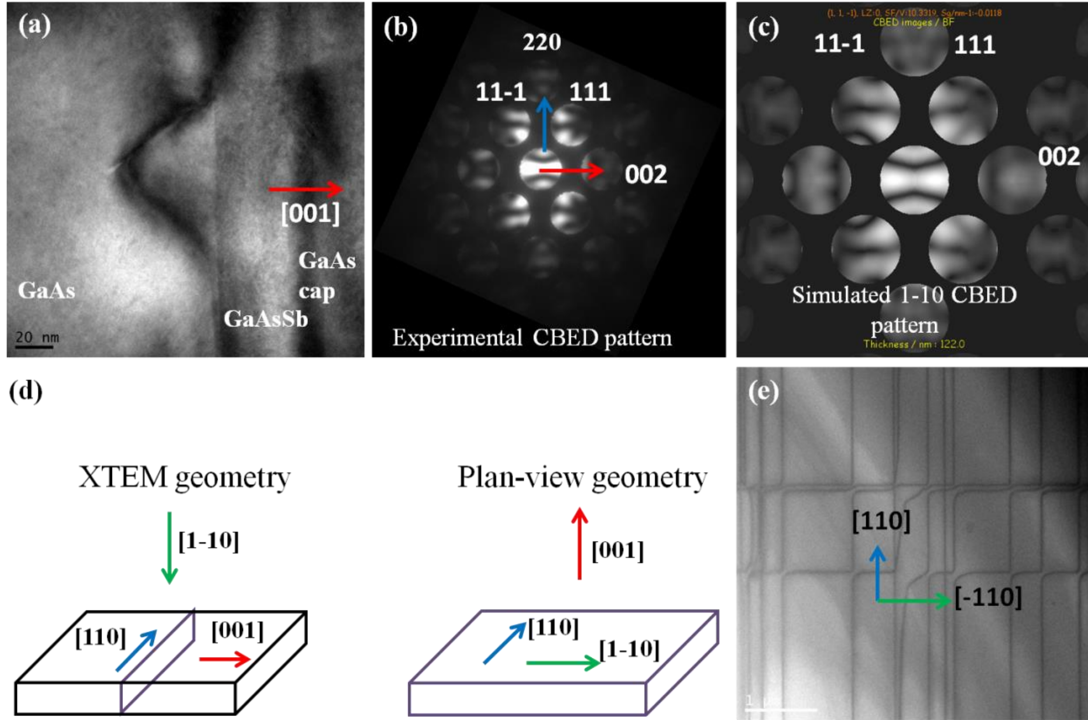

Fig. 3.8: (a) Cross-sectional TEM (XTEM) image of GaAs/GaAsSb/GaAs heterostructure showing in-plane [001] growth direction; (b) experimental CBED pattern collected from the GaAs substrate region of (a); (c) simulated [110] zone-axis CBED pattern matched with the experimental pattern shown in (b); (d) schematic of the geometry of XTEM and plan-view TEM samples showing in-plane and out-of-plane directions; (e) plan-view TEM image with identified in-plane [110] and $[1\bar{1}0]$ directions.

The crystal polarity in cross-sectional GaAs samples was determined by matching experimental and simulated <110> zone-axis CBED patterns. The loss of inversion symmetry in non-centrosymmetric crystal becomes readily apparent because of the differences in dynamical-diffraction-related intensity patterns in Bijvoet pairs of reflections. For example, there is a difference in intensity patterns between Bijvoet-pair

(111) and $(\overline{111})$ reflections in $[1\bar{1}0]$ zone-axis CBED pattern, which indicate the breakdown of Friedel's law due to multiple scattering effect.

Figure 3.8(a) shows a cross-sectional TEM image of a sample in <110> projection. The experimental CBED pattern, shown in Fig. 3.8(b), was collected from the GaAs substrate of the sample shown in Fig. 3.8(a). The simulated CBED pattern shown in Fig. 3.8(c) was generated using JEMS software [28]. The simulation was carried out for a sample thickness of 122 nm with the accelerating voltage set at 200 kV. Before comparing the intensity distribution of {111} reflections, the (002) disc in the experimental pattern was identified by aligning the g_{002} vector in the diffraction pattern with the [001] growth direction (shown by red arrow in Fig. 3.8) in a cross-sectional image of the sample.

The intensity patterns in {111} reflections on either side of the (002) disc in experimental and simulated CBED patterns were then compared. They showed clear differences in [110] and $[1\bar{1}0]$ zone-axis patterns which enabled the absolute orientations of the samples to be determined. Once the projection direction (shown as green arrow in Fig. 3.8) is known, the <110> direction (shown as blue arrow) parallel to the interface line in cross-sectional geometry can then be specified. The projection direction and the interface line direction in cross-sectional samples become the two in-plane orthogonal <110> directions in plan-view projection, as demonstrated in Fig. 3.8(d). Thus, special care was taken when preparing plan-view samples and loading them into TEM specimen holder so that the two in-plane orthogonal <110> directions in plan-view sample could be correlated with the already determined projection and interface line directions in the corresponding cross-sectional sample. It should be noted that to

successfully apply this method one must know the correct rotation angle between the image and the diffraction pattern. This rotation angle can be determined by under-focusing the diffraction lens so that an image of the sample is observed within each CBED disc. This angle was further confirmed by checking the orientation of a GaInP/GaAs samples using both CBED and aberration-corrected STEM imaging methods. The ability to distinguish between two <110> directions in plan-view samples allowed the asymmetry of dislocation distribution to be determined by measuring the mean spacing of α and β dislocations.

Strong asymmetry in the distribution of misfit dislocations was observed in the early stages of strain relaxation. Figure 3.9 shows a collage of bright-field TEM images of the interfacial dislocations in plan-view [001] projection in the GaAs/$GaAs_{0.917}Sb_{0.083}$/GaAs(001) heterostructure with 2000-nm-thick film. As clearly apparent from Fig. 3.9, the density of misfit dislocations at the cap/film interface having line direction, u=$[110]$ was much higher than those having u=$[\bar{1}10]$.

The density of misfit dislocations along the two <110> directions could be measured by determining the dislocation spacing along the two directions once the $[110]$ direction is distinguished from the $[\bar{1}10]$ in plan-view TEM samples using the method described above. Collages of several plan-view TEM images, typically covering several tens of μm distances along each <110> direction, were recorded. Figure 3.10 shows the measured misfit dislocation spacings at film/substrate and cap/film interfaces of GaAs/GaAsSb/GaAs heterostructures. The excess stress values were then calculated considering that strain relaxation takes place by single-kink motion of threading dislocations.

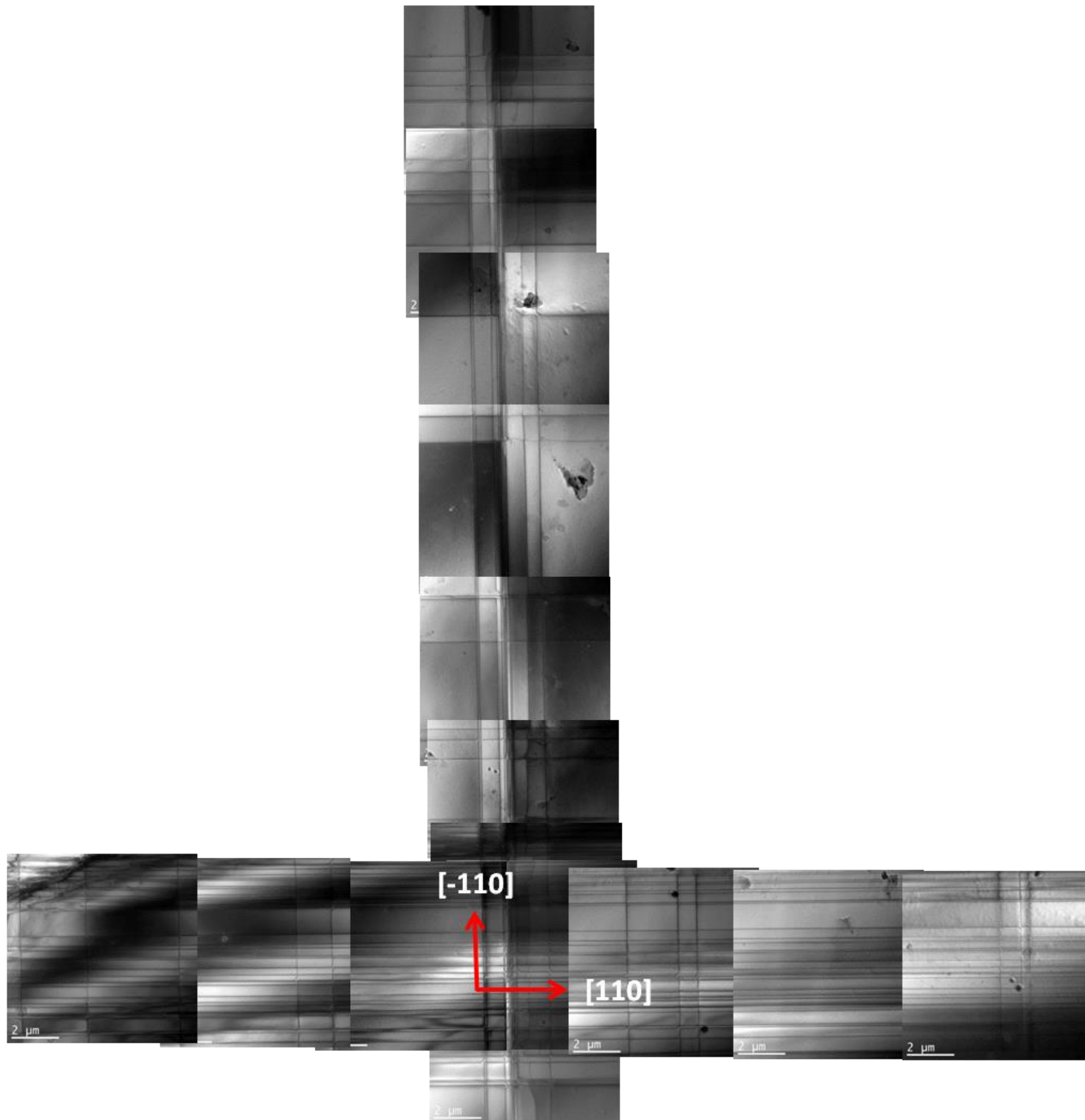

Fig. 3.9. Collage of plan-view bright-field [001] projected images showing distribution of misfit dislocations along the two <110> directions in at the cap/film interface of $GaAs/GaAs_{0.917}Sb_{0.083}/GaAs(001)$ heterostructure with 2000-nm-thick film.

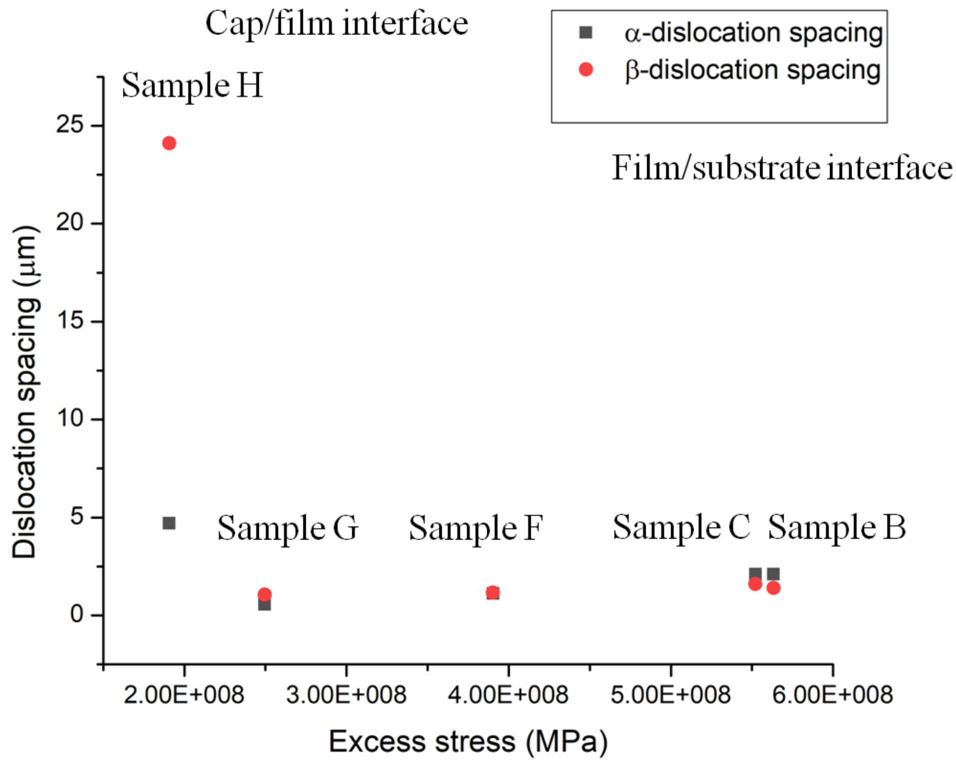

Fig. 3.10. Plot showing dislocation spacing as a function of excess stress for film/substrate interfaces and cap/film interfaces of GaAs/GaAsSb/GaAs heterostructures.

The density of dislocations extending along [110] direction is higher irrespective of the sign of strain at the interface. As noted earlier, the dislocation line corresponding to α-/β-dislocations changes between the two <110> directions with the change in the sign of strain at the interface. It is evident from Fig. 3.10 that the density of β-dislocations (inverse of square of dislocation spacing) is higher than for α-dislocations at the compressively-strained film/substrate interfaces, whereas the density of α-dislocations is higher at the tensile-strained cap/film interfaces. Since the in-plane edge component of

the Burgers vector relieves the misfit strain, the major relaxation direction becomes $[1\bar{1}0]$.

It has been reported that the major relaxation axis remains $[1\bar{1}0]$ regardless of the sign of interfacial strain in InGaP/GaAs heterostructures [29]. However, it was found that the direction along which the density of dislocations is higher swaps as a result of change in the sign of strain. The results were explained assuming the presence of dislocations with incorrect Burgers vectors, which effectively increases instead of relieving the interfacial strain. However, our aberration-corrected electron microscopy observations showed that the misfit dislocations in our samples had the correct sense of Burgers vector. Fox *et al*. suggested that the nucleation barrier is not the reason for asymmetry, and the sole reason is different Peierls barrier to dislocation glide corresponding to the two types of dislocation core [18]. However, our observations indicate that the type of dislocation that has higher density depends on the sign of strain at the interface. Moreover, 60° misfit dislocations were found to dissociate into 30° and 90° Shockley partial dislocations. A detailed description of the atomic arrangement of dissociated 60° dislocations and the associated partial dislocations is given later in Chapter 4. Shockley 30° partial dislocations are the leading dislocations in the case of compressively-strained film/substrate interfaces and typically reside in the GaAs substrate. The Shockley 90° partial dislocation is the leading dislocation at the tensile-strained cap/film interface and resides in the GaAsSb film layer, which suggests that the main reason for asymmetry might not be the Peierls stress specific to a dislocation core with specific chemical nature. However, the reason for the unique relaxation direction in the GaAs/GaAsSb/GaAs heterostructures is not clear at this point.

3.7 Dislocation nucleation and density evolution at GaAsSb/GaAs and GaAs/GaAsSb interfaces during Stage-I relaxation

The concept of excess stress as proposed by Dodson and Tsao is invoked to understand Stage-I strain relaxation at the film/substrate and cap/film interfaces [30]. The excess stress is defined as the difference between the stress related to the elastic strain energy and the dislocation self-stress. Excess stress is the driving force for threading dislocations to move laterally and relieve misfit strain. The expression for excess stress corresponding to macroscopically single-kink (SK) motion of misfit dislocations is given by [30]:

$$\tau_{ex}^{SK} = \frac{\mu cos\varphi}{(1-\nu)}[2(\varepsilon - \varepsilon_p)(1+\nu)cos\lambda - \frac{b(1-\nu cos^2\theta)}{4\pi h}\ln\left(\frac{4R}{b}\right)] \quad (6)$$

where μ is the [001] shear modulus of the relaxing layer, ν is the Poisson's ratio, ε is the misfit strain, ε_p is the amount of plastic strain, φ is the angle between the interface normal and the slip plane, λ is the angle between the Burgers vector and direction in the interface that is normal to dislocation line, b is the Burgers vector, θ is the angle between the dislocation line and Burgers vector, h is the thickness of the layer undergoing strain relaxation and R is the outer cut-off radius of the dislocation core. The value of R depends on the separation distance (S) between misfit dislocations at the interface. R= S/2, when S/2<h and R=h, when S/2>h [31]. In the case of strain relaxation at the GaAsSb/GaAs film/substrate interface, R=h for Samples A-C whereas R=S/2 for Samples D-H. The experimentally measured average values of S for Samples D, E, F, G and H are 110, 90, 74, 65 and 53 nm, respectively. For strain relaxation at the GaAs/GaAsSb cap/film interface, R=h. The inner cut-off radius of the dislocation core is

assumed to be b/4, which is typical for covalent semiconductors [32].

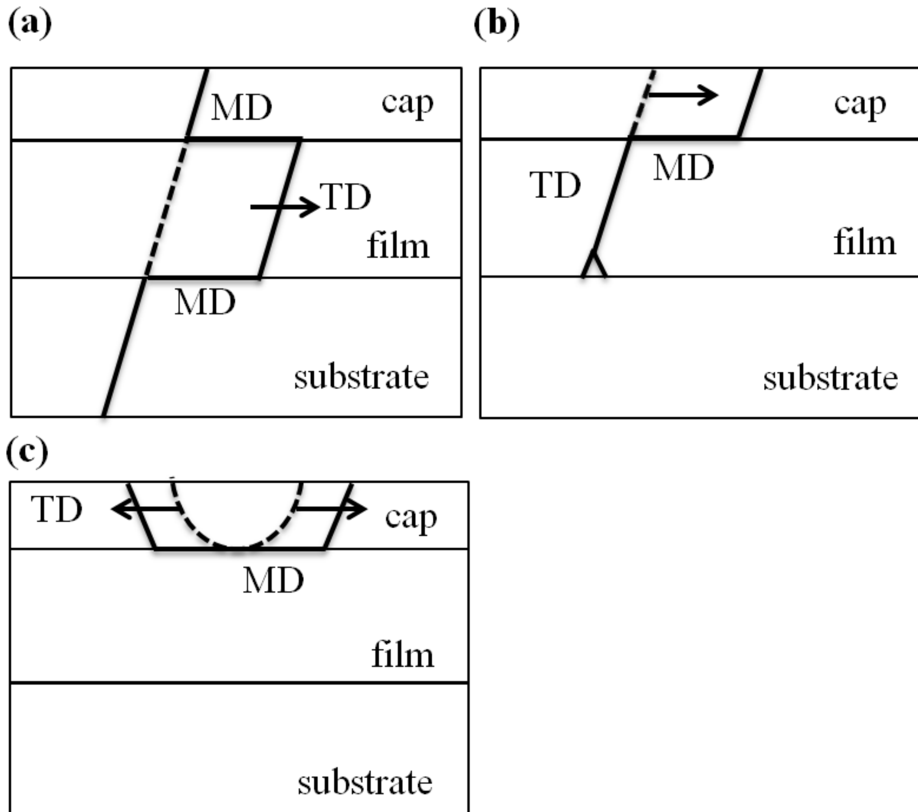

Fig. 3.11. Schematic depiction of possible strain relaxation mechanisms at the cap/film interface: (a) Extended double-kink motion of threading dislocation in the film; (b) Glide of threading dislocation in the capping layer, which is blocked at the film/substrate interface; (c) Surface half-loop creation and subsequent glide of threading dislocation in the capping layer.

Misfit dislocations at the GaAs/GaAsSb cap/film interface can be introduced in three different ways. Figure 3.11 provides a schematic illustration of these mechanisms. One possible way to deposit misfit dislocations at the cap/film interface is by propagation of dislocation dipoles [7], as illustrated in Fig. 3.11(a). In strained-layer heterostructures with a capping layer, the moving threading arm in the film may generate two misfit

dislocations, one at the film/substrate interface and one at the cap/film interface, which would have equal Burgers vectors of opposite sign and share the same glide plane. This kind of dislocation geometry has been experimentally observed by noting pairs of misfit dislocation lines in plan-view TEM samples [7,8]. Detailed theoretical investigations have also been carried out to understand when double misfit line geometry becomes energetically favorable [33,34]. The excess stress expression for this kind of extended double-kink (DK) motion of dislocation dipoles has additional terms corresponding to the self-stress of misfit dislocation at the cap/film interface and for interaction between misfit dislocations at the two interfaces [21] -

$$\tau_{ex}^{DK} = \frac{\mu cos\varphi}{(1-\nu)}[2(\varepsilon - \varepsilon_p)(1+\nu)cos\lambda - \frac{b(1-\nu cos^2\theta)}{4\pi h}\left(\ln\left(\frac{4h}{b}\right) + \ln\left(\frac{4(h_{cap}+h)}{b}\right) + 2\ln\left(\frac{h}{h_{cap}+h}\right)\right)] \quad (7)$$

This equation assumes no interaction of strain fields between dislocations lying at the same interface. This condition is met only for Samples A-C. For Samples D-H, although this equation may not yield quantitatively accurate values of excess stress corresponding to DK motion, the trend of excess stress evolution with increasing film thickness should still be the same.

The threading dislocations that are pinned at the GaAsSb/GaAs film/substrate interface may act as pre-existing dislocation sources and these dislocations can glide laterally to relieve misfit strain when the excess stress in the capping layer is positive. Figure 3.11(b) shows a schematic illustration of this process. The excess stress for the cap/film interface, considering that strain relaxation occurs by movement of threading

dislocations through the capping layer, can also be evaluated using Eq. (6) with ***h*** corresponding to the thickness of the capping layer.

The heterogeneous nucleation of dislocation half-loops at the surface might be possible, especially since deterioration of the growth surface can be expected in thicker films. The surface steps associated with 60° dislocations create a cross-hatch surface morphology in low-mismatched (001)-grown heterostructures [35,36]. The stress concentration at the surface troughs can make them potential nucleation sites for dislocation half-loops [37]. These half-loops can create two threading dislocations upon reaching the interface, which move laterally in opposite directions under the application of misfit stress, thus generating misfit dislocations at the cap/film interface. The schematic illustration of this process is shown in Fig. 3.11(c). Alternative contributions such as homogeneous nucleation of surface half-loops, operation of Hagen-Strunk mechanism [38] or dislocation injection from 'diamond' defects have been proposed [39]. However, due to lack of experimental observations and/or theoretical investigations showing the energetic cost as too high to be realistic, these mechanisms are not considered to be major sources for dislocation nucleation at the cap/film interface.

Figure 3.12 shows a plot of excess stress for single-kink motion of misfit dislocations (eq. 6) and for double-kink motion of misfit dislocations (eq. 7) evaluated at the film/substrate interface and at the cap/film interface. The density of 60° misfit dislocations at the film/substrate interfaces of Samples B and C, and at the cap/film interfaces of Samples F-H, are also shown. The dislocation density was calculated by measuring the dislocation spacing from collages of plan-view TEM images typically

covering distances of more than 100 μm along each of the two <110> directions. The dislocation densities are listed in Table 3.3:

Table 3.3: Dislocation densities at heterointerfaces that have undergone Stage-I relaxation

Sample	Dislocation density (1×10^{8} cm^{-2})
B	0.36
C	0.29
F	4.1
G	5.4
H	0.77

The following observations can be made from Fig. 3.12:

(i) Despite excess stress on dislocations at the cap/film interface, either corresponding to motion of single misfit dislocations or dislocation dipoles, which is lower in comparison to that on dislocations at the film/substrate interface, the density of misfit dislocations at the cap/film interfaces of Samples F-H is higher than at the film/substrate interfaces of Samples B and C. This apparent anomaly is expected since the GaAs capping layers were grown at higher temperature (600 °C) compared to the GaAsSb films (500 °C). During Stage-I relaxation, kinetic factors such as dislocation nucleation and mobility determine the final density of

dislocations. Both these factors have an Arrhenius-type relation with temperature, and their rates increase with temperature increase. Additionally, if heterogeneous nucleation of dislocation half-loops is considered to be the primary mechanism for dislocation generation, which is shown later to be true, the well-developed cross-hatch pattern of the growth surface in heterostructures that have undergone Stage-II or Stage-III relaxation will significantly impact the final dislocation density by facilitating dislocation nucleation at the surface troughs. Thus, the higher density of misfit dislocations at the cap/film interface can be attributed to the higher growth temperature of the GaAs capping layer and enhanced heterogeneous nucleation of dislocation half-loops at the rougher growth surface.

(ii) The onset of relaxation at both interfaces, as observed by TEM, has been marked with arrows in Fig. 3.12. In the case of Sample A, only one single dislocation was observed in an area of 150×150 μm^2. Thus, the estimated dislocation density was ~ 4.5×10^3 cm^{-2} or lower. Such a low density of dislocations at the film/substrate interface indicates that the critical thickness for the GaAsSb film has just been reached. On the other hand, the misfit dislocation distribution at the cap/film interface was first observed in Sample E. The excess stress corresponding to single-kink motion of threading dislocations at this interface becomes positive with increasing film thickness for the first time in Sample E and misfit dislocations are accordingly generated. As can be seen in Fig. 3.12, the density of misfit dislocations at the cap/film interface in Sample E was, however, higher although the excess stress was approximately half that of Sample A. This reduction of critical thickness at the cap/film interface can again be attributed to

the higher growth temperature of the GaAs capping layer and rougher surface with well-developed cross-hatch morphology.

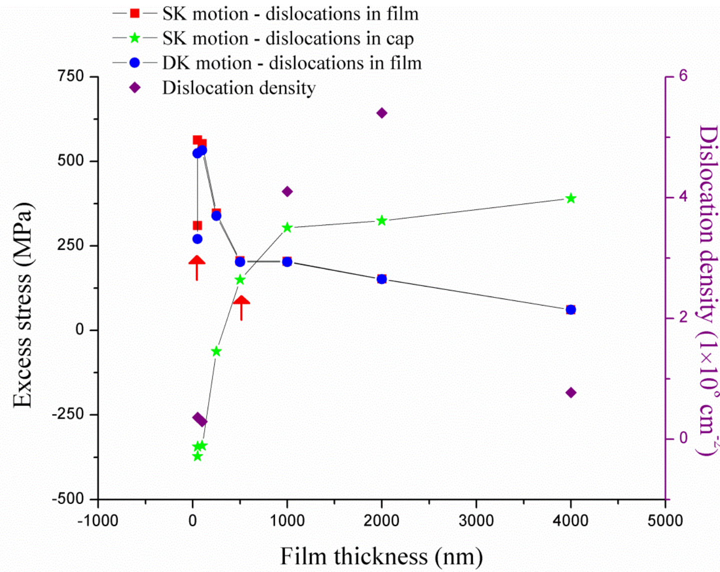

Fig. 3.12. Evolution of excess stress and dislocation density with increasing film thickness. The dislocation density values are shown for film/substrate interfaces in Samples B and C, and for cap/film interfaces in Samples F, G and H. The two arrows mark the onset of relaxation at the two interfaces: Sample A for film/substrate interface and Sample E for cap/film interface. SK: single-kink, DK: double-kink.

(iii) The dislocation density evolution at the cap/film interface appears to be more complex than at the film/substrate interface. As observed from Fig. 3.12, the dislocation density at the film/substrate interface increases with excess stress. However, the dislocation density at the cap/film interface increases with excess stress in Samples E, F and G and then decreases in Sample H even though the excess stress increases. The kinetic factors that govern the early stages of strain relaxation, namely dislocation

nucleation and mobility, need to be better understood in order to explain this observation. Mathematically, the rate of strain relaxation at early stage can be expressed as [8] -

$$\frac{d\varepsilon(t)}{dt} = N(t)Vbcos\theta \tag{8}$$

N(t) is the density of nuclei at time t as given by -

$$N(t) = BN_0 t\tau_{ex}^{n} \exp\left(-\frac{Q_n}{KT}\right) \tag{9}$$

where B and n are material constants, N_0 is the density of pre-existing nuclei at t=0, Q_n is the activation energy for dislocation nucleation.

V is the velocity of dislocations at time t as given by -

$$V = V_0\left(\frac{\tau_{ex}}{\mu}\right)^{m} \exp\left(-\frac{Q_v}{kT}\right) \tag{10}$$

where V_0 and m are material constants and Q_v is the activation energy for dislocation glide.

Both density of nuclei and velocity of dislocations are excess-stress dependent and they are expected to increase with increase in excess stress. Therefore, the only other factor that might explain the lowering of dislocation density in Sample H is lowering of pre-existing nuclei, N_0 term in Eq. 10. The three possible sources of dislocation nucleation have already been discussed previously and shown schematically in Fig. 3.11. Operation of double-kink motion of threading dislocations, which has been observed in GaAsP/GaAs [7] and SiGe/Si [8] systems, can be noted in plan-view TEM images by observing pairs of dislocations with separation distance being $h \cot 55°$ [7]. However, the majority of dislocations in Samples B and C were found to exist as unpaired dislocations.

Moreover, as can be noted from Fig. 3.12, single-kink motion would be favored from the excess-stress point of view as compared to double-kink motion. In thicker films of Samples D-H, the excess stress for double-kink motion gradually decreases. Thus, if double-kink motion is occurring for Samples D-H, one would expect a decrease in dislocation density at the cap/film interface with increasing film thickness. However, the TEM results show increases in dislocation density in Samples E-G. From these observations, it is concluded that misfit dislocation deposition at the cap/film interface via double-kink motion of threading dislocations in the film is not operative in the present system.

The threading dislocations that are blocked at the film/substrate interface can also glide laterally to relieve misfit strain in the capping layer. The density of threading dislocations in the film would be dependent on the number of blocking events at the film/substrate interface. In thicker films such as Samples D-H, the density of dislocations at the film/substrate interface is very high and interactions of the dislocation strain fields are inevitable, which may lead to blocking of certain threading dislocations. The success of blocking events should increase with decreasing excess stress. Accordingly, one would expect the highest threading dislocation density in Sample H. However, another competing effect that might reduce the density of threading dislocations is dislocation annihilation. It is well established for high-mismatched heterostructures that the threading dislocation density in thicker films typically decreases due to annihilation of dislocations having opposite Burgers vector [22]. In low-mismatched heterostructures, however, the density of threading dislocations is several orders of magnitude lower. It should be noted that no threading dislocations were observed in cross-sectional TEM images of Samples

F-H. Thus, interaction of such sparsely populated threading dislocations leading to significant reduction of threading dislocation density through an annihilation process appears to be unlikely in low-mismatched systems. In that case, the N_0 term should not drastically decrease for Sample-H. Hence, it is concluded that single-kink motion of threading dislocations that are blocked at the film/substrate interface is not the primary mechanism for strain relaxation at the cap/film interface.

For single-kink motion of threading dislocations in the capping layer, heterogeneously nucleated surface half-loops can be a source for threading dislocations extending into the capping layer from the surface. Figure 3.13(a) shows height profiles obtained from AFM images of Samples E-H. It is immediately evident that the surface is mesoscopically much smoother for Sample H. The trough-to-trough distances are measured to be 1 ± 0.2 μm, 1.1 ± 0.3 μm, 1.4 ± 0.5 μm and 2.3 ± 0.3 μm for Samples E, F, G and H, respectively. It appears that the surface starts to recover itself through surface step elimination via lateral mass transport [40] as the relaxation rate slows down in Stage-III. Figures 3.13(b) and (c) show AFM surface profiles of Samples G and H. It is clear that the cross-hatch morphology is much less prominent for Sample H. It should be noted that the time required to grow Sample H is twice of that for Sample G, and Sample H is only 11% more relaxed than Sample G. Hence, the growth front has sufficient time to eliminate surface steps through diffusion-controlled mass transport in the absence of significant addition of surface steps that are created due to plastic relaxation.

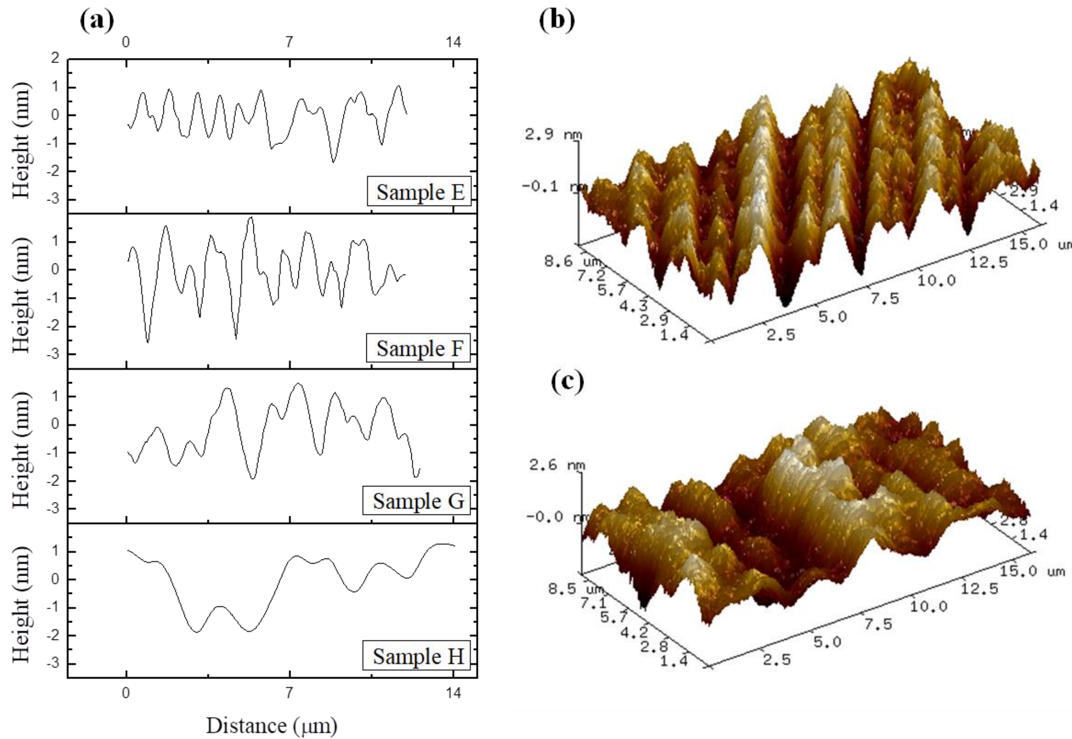

Fig. 3.13. (a) Surface height profiles along <110> direction obtained by AFM in Samples E-H. AFM images showing surface topography of (b) Sample G and (c) Sample H.

The areal density of troughs is thus considerably decreased in Sample H. Since these troughs are nucleation sites for dislocations, dislocation creation for strain relaxation in the capping layer is directly impacted and a noticeable drop in dislocation density is observed at the cap/film interface of Sample H. These results provide unambiguous evidence that heterogeneous nucleation of dislocation half-loops at the surface is the primary nucleation mechanism in low-mismatched heterostructures.

In the absence of cross-hatch morphology, the strain relaxation in the film can be initiated by pre-existing threading dislocations. However, as these threading dislocations move, they create ridges and grooves at the surface, thereby making heterogeneous

nucleation of surface half-loops possible. In fact, the misfit dislocation densities at the film/substrate interfaces of Samples B and C are orders of magnitude higher than the typical dislocation density of the substrate. This observation supports the conclusion that heterogeneously nucleated surface half-loops are a major source of dislocations even at early stages of relaxation.

3.8 Conclusions

Defects created at different stages of strain relaxation in low-mismatched GaAs(cap)/GaAsSb/GaAs(001) heterostructures have been characterized, and the evolution of dislocation density and surface morphology has been investigated. The major conclusions of this study can be summarized as follows:

(i) By systematically varying GaAsSb film thicknesses in the range of 50 to 4000 nm, three different stages of strain relaxation were identified. The films relaxed very slowly during Stage-I, exhibiting a metastable growth regime of low defect density. Rapid relaxation took place in Stage-II, while the relaxation rate decreased again in Stage-III.

(ii) Most defects created during Stage-I are 60° dislocations that cause asymmetric strain relaxation. Dislocations with [110] line direction were found to be higher in density irrespective of the sign of strain at the interface. Apart from 60° dislocations, dislocation lines of edge character were also observed.

(iii) Many curved dislocations were formed during Stage-II and Stage-III relaxation. The majority were on the GaAs substrate side, and some had edge character.

Cross-sectional TEM images revealed that all GaAsSb films had undergone 2D layer-by-layer growth and they were mostly free of threading dislocations.

(iv) Stage-I strain relaxation was exhibited by the formation of dissociated positive 60° dislocations at the cap/film interfaces of heterostructures with thicker GaAsSb films (500 nm and above). Moreover, the strain relaxation was primarily carried out by threading dislocations created by heterogeneous nucleation of surface half-loops. A decrease in dislocation density at the cap/film interface was observed in the heterostructure with the 4000-nm-thick film even though excess stress had increased. This was correlated with smoothening of the surface in this heterostructure, which reduced the number of potential nucleation sites for dislocation half-loops. The cross-hatched surface morphology is also commonly observed in InGaAs/GaAs and SiGe/Si heterostructures. Hence, the conclusion about surface half-loops are the primary source of dislocations should in general also be valid for any low-mismatched epitaxially-grown diamond-cubic/sphalerite semiconductor heterostructure.

References

[1] T. Anan, M. Yamada, N. Nishi, K. Kurihara, K. Tokutome, A. Kamei, S. Sugou, Electron. Lett. 37 (2001) 566–567.

[2] C.M. Jones, E. Kioupakis, J. Appl. Phys. 122 (2017).

[3] F.C. Frank, J.H. Van Der Merwe, (1947) 216–225.

[4] J.H. Van Der Merwe, J. Appl. Phys. 34 (1963) 117–122.

[5] J.H. Van Der Merwe, J. Appl. Phys. 34 (1963) 123–127.

[6] J.W. Matthews, S. Mader, T.B. Light, J. Appl. Phys. 41 (1970) 3800–3804.

[7] J.W. Matthews, J. Cryst. Growth 27 (1974) 118–125.

[8] D.C. Houghton, J. Appl. Phys. 70 (1991) 2136–2151.

[9] J. Narayan, S. Oktyabrsky, J. Appl. Phys. 92 (2002) 7122–7127.

[10] Y.B. Bolkhovityanov, A.S. Deryabin, A.K. Gutakovskii, L. V. Sokolov, A.P. Vasilenko, Acta Mater. 61 (2013) 5400–5405.

[11] K.L. Kavanagh, M.A. Capano, L.W. Hobbs, J.C. Barbour, P.M.J. Marée, W. Schaff, J.W. Mayer, D. Pettit, J.M. Woodall, J.A. Stroscio, R.M. Feenstra, J. Appl. Phys. 64 (1988) 4843–4852.

[12] E.A. Fitzgerald, D.G. Ast, P.D. Kirchner, G.D. Pettit, J.M. Woodall, J. Appl. Phys. 63 (1988) 693–703.

[13] K.H. Chang, P.K. Bhattacharya, R. Gibala, J. Appl. Phys. 66 (1989) 2993–2998.

[14] J. Zou, D.J.H. Cockayne, B.F. Usher, J. Appl. Phys. 73 (1993) 619–626.

[15] A. Maros, N. Faleev, R.R. King, C.B. Honsberg, D. Convey, H. Xie, F.A. Ponce, J. Vac. Sci. Technol. B 34 (2016) 02L113.

[16] B.P. Rodríguez, J.M. Millunchick, J. Appl. Phys. 100 (2006) 4–11.

[17] A. Gangopadhyay, A. Maros, N. Faleev, D.J. Smith, Acta Mater. 162 (2019) 303-315.

[18] B.A. Fox, W.A. Jesser, J. Appl. Phys. 68 (1990) 2739–2746.

[19] R.S. Goldman, K.L. Kavanagh, H.H. Wieder, S.N. Ehrlich, R.M. Feenstra, J. Appl. Phys. 83 (1998) 5137–5149.

[20] D.B. Williams, C.B. Carter, Transmission Electron Microscopy: A Textbook for Materials Science, second ed., Springer, New York, 2009.

[21] E.A. Fitzgerald, G.P. Watson, R.E. Proano, D.G. Ast, P.D. Kirchner, G.D. Pettit, J.M. Woodall, J. Appl. Phys. 65 (1989) 2220–2237.

[22] R. Hull, J.C. Bean, Crit. Rev. Solid State Mater. Sci. 17 (1992) 507–546.

[23] F.A. Ponce, D.P. Bour, W.T. Young, M. Saunders, J.W. Steeds, Appl. Phys. Lett. 69 (1996) 337–339.

[24] D.J. Smith, R.W. Glaisher, P. Lu, Philos. Mag. Lett. 59 (1989) 69–75.

[25] M. De La Mata, C. Magen, J. Gazquez, M.I.B. Utama, M. Heiss, S. Lopatin, F. Furtmayr, C.J. Fernández-Rojas, B. Peng, J.R. Morante, R. Rurali, M. Eickhoff, A. Fontcuberta I Morral, Q. Xiong, J. Arbiol, Nano Lett. 12 (2012) 2579–2586.

[26] J. Tafto, J.C.H. Spence, J. Appl. Crystallogr. 15 (1982) 60–64.

[27] S. Lavagne, C. Roucau, C. Levade, G. Vanderschaeve, Philos. Mag. A 82 (2002) 1451–1462.

[28] P.A. Stadelmann, Ultramicroscopy 21 (1987) 131–145.

[29] M.J. Matragrano, D.G. Ast, J.R. Shealy, V. Krishnamoorthy, J. Appl. Phys. 79 (1996) 8371–8378.

[30] B.W. Dodson, J.Y. Tsao, Appl. Phys. Lett. 51 (1987) 1325–1327.

[31] E.A. Fitzgerald, Mater. Sci. Reports 7 (1991) 87–140.

[32] J.P. Hirth, J. Lothe, Theory of Dislocations, second ed., Wiley, New York, 1982.

[33] M.E. Twigg, J. Appl. Phys. 68 (1990) 5109–5114.

[34] T.J. Gosling, R. Bullough, S.C. Jain, J.R. Willis, J. Appl. Phys. 73 (1993) 8267–8278.

[35] J.W.P. Hsu, E.A. Fitzgerald, Y.H. Xie, P.J. Silverman, M.J. Cardillo, Appl. Phys. Lett. 61 (1992) 1293–1295.

[36] K.H. Chang, R. Gilbala, D.J. Srolovitz, P.K. Bhattacharya, J.F. Mansfield, J. Appl. Phys. 67 (1990) 4093–4098.

[37] M. Albrecht, S. Christiansen, J. Michler, W. Dorsch, H.P. Strunk, P.O. Hansson, E. Bauser, Appl. Phys. Lett. 67 (1995) 1232.

[38] W. Hagen, H. Strunk, Appl. Phys. 17**,** 85–87 (1978)

[39] D.J. Eaglesham, E.P. Kvam, D.M. Maher, C.J. Humphreys, D.J. Eaglesham, D.M. Maher, J.C. Bean, Philos. Mag. A 59 (1989) 1059–1073.

[40] A.M. Andrews, J.S. Speck, A.E. Romanov, M. Bobeth, W. Pompe, J. Appl. Phys. 91 (2002) 1933–1943.

CHAPTER 4

ATOMIC-SCALE CHARACTERIZATION OF INTERFACIAL DEFECTS IN LOW-MISMATCHED GaAs(001)-BASED HETEROSTRUCTURES

4.1 Introduction and Motivation

Misfit dislocations and, more importantly, their associated threading arms are often deleterious for device performance as they introduce deep-level traps that can act as non-radiative recombination centers for charge carriers [1,2]. The location of the traps within the bandgap is related to the specific type and core structure of the dislocation [3]. Thus, the detailed atomic arrangements at the dislocation core can play important roles in determining the device electronic properties. Moreover, the type and core structure of a dislocation influence its velocity, and thus govern the kinetics of plastic relaxation of an epitaxial film during growth, especially in its initial stages [4].

Transmission electron microscopy (TEM) has historically played a pivotal role in the characterization of dislocations. The strain contrast from dislocations was exploited in the *g.b* method to determine the Burgers vector of the defect [5]. Alternatively, the edge component of a Burgers vector can be determined by drawing a Burgers circuit around a lattice image obtained using high-resolution electron microscopy, with the projection direction aligned with the dislocation line direction. Apart from determining the Burgers vector of the dislocation, the high spatial resolution offered by electron microscopy is useful for studying dislocation core structures in semiconductors. The dislocations belong to either glide set or shuffle set depending on whether the shear takes place between

closely or widely spaced {111} planes [6]. The structure of dislocation cores can be further complicated by reconstruction of the core, by the presence of kinks and jogs along the dislocation line, or by possible interaction with vacancies and other dislocations [7].

Direct structural imaging of dislocation cores has previously been challenging due to the requirement for atomic resolution, which was historically difficult to achieve due to the aberration-limited resolution of the objective lens of the electron microscope. The correction of spherical aberration of the objective lens was first realized in the late 1990s [8,9] and sub-angstrom resolution is nowadays routinely achieved. Moreover, high-angle annular-dark-field imaging with probe-corrected scanning TEM offers the advantage of atomic-resolution Z-contrast imaging with no contrast reversal with defocus, making the image interpretation much more intuitive. This development has led to a resurgence in the atomic-scale characterization of defects in semiconductor thin films and heterostructures [10-12]. This chapter describes atomic-scale characterization of interfacial dislocations, generated during the strain relaxation process in low-mismatched GaAs(001)-based heterostructures.

4.2 Dissociated 60° dislocations

60° dislocations are primarily formed during the initial stage of strain relaxation in GaAs/GaAsSb/GaAs heterostructures, as already described in Chapter 1. Figure 4.1(a) shows the crystallography of 60° dislocations for the sphalerite structure. Negative 60° dislocations are formed at the film/substrate interface to relieve compressive misfit strain. The core structure of dislocations which lie in $(1\bar{1}1)$ and $(\bar{1}11)$ slip planes and have [110] dislocation line direction are visible in 110 projected (S)TEM images. The possible

Burgers vectors $a/2[10\bar{1}]$ and $a/2[0\bar{1}\bar{1}]$ in $(1\bar{1}1)$ plane are shown by yellow arrows, while green arrows mark $a/2[0\bar{1}1]$ and $a/2[101]$ Burgers vectors that lie in $(\bar{1}11)$ slip plane. These Burgers vectors, however, do not lie in (110) projection plane and their projected components run along $[\bar{1}12]$ and $[\bar{1}1\bar{2}]$ directions, which are the traces of $(1\bar{1}1)$ and $(\bar{1}11)$ slip planes in the projection plane. Figure 4.1(a) also shows the dissociation of an $a/2[0\bar{1}\bar{1}]$ perfect dislocation into $a/6[\bar{1}\bar{2}\bar{1}]$ and $a/6[1\bar{1}\bar{2}]$ Shockley partials, as indicated by purple arrows. The $a/6[1\bar{1}\bar{2}]$ Shockley partial lies completely in the (110) projection plane whereas $a/6[\bar{1}\bar{2}\bar{1}]$ partial does not, and it would thus have a projected component along the $[\bar{1}12]$ direction. Understanding these geometrical constructions is important to correctly determine the Burgers vectors of dislocations in projected (S)TEM images, which will be described next.

All of the 60° interfacial misfit dislocations observed in this study were dissociated to form intrinsic stacking faults, which are denoted by observation of a single faulted layer in atomic-resolution (S)TEM images. Figure 4.1(b) shows an atomic-resolution HAADF-STEM image of a dissociated 60° dislocation at the film/substrate interface. The perfect stacking of AaBbCcAaBbCc changes to AaBbCcBbCcAa in the faulted region, where ABC and abc represent the close-packed {111} planes in the cation (Ga) sublattices and anion (As) sublattices, respectively. A right-hand/finish-start (RH/FS) Burgers circuit enclosing both partial dislocations bounding the stacking fault was drawn to identify the Burgers vector of the perfect dislocation, which was found to be $a/4[1\bar{1}\bar{2}]$ according to the directions shown in Fig. 4.1(b). As illustrated in Figure 4.1(a), this is the projected component of the $a/2[0\bar{1}\bar{1}]$ or $a/2[10\bar{1}]$ Burgers vector which lies in $(1\bar{1}1)$ slip plane and makes a 60° angle with the $[110]$ dislocation line

direction, which is also the projection direction. Because STEM images are 2D projections of a 3D structure, no distinction between these two Burgers vectors can be made.

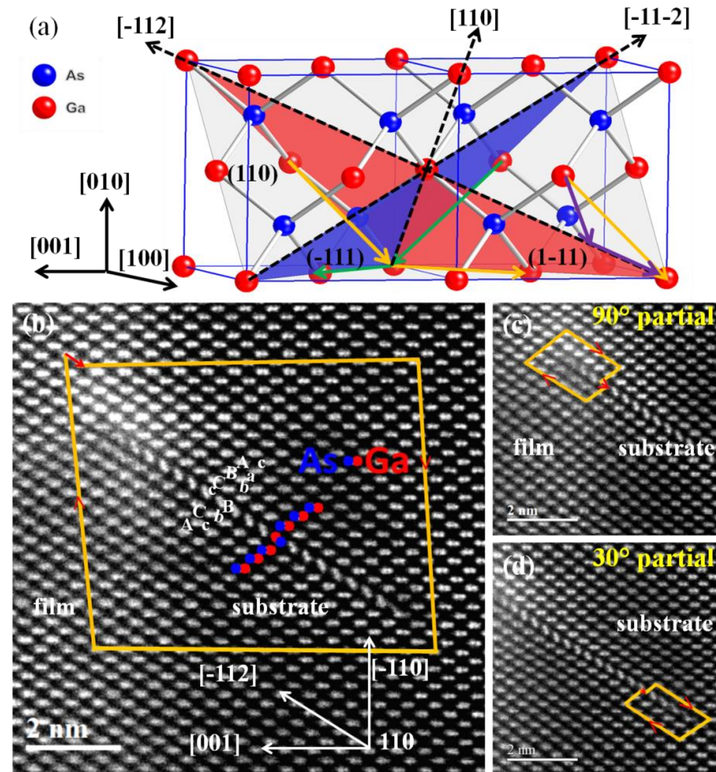

Fig. 4.1. (a) Crystal model showing Burgers vectors of perfect 60° dislocations and Shockley partial dislocations generated at compressively-strained (001) interface. Aberration-corrected HAADF-STEM images of GaAsSb/GaAs(001) heterostructure showing: (b) dissociated 60° dislocation at film/substrate interface, (c) 90° partial dislocation located very close to film/substrate interface, and (d) 30° partial dislocation located well into substrate [12].

Stacking faults are bounded by partial dislocations which can be either Shockley or Frank partials [13]. Shockley partials have Burgers vectors of $a/6\langle 112\rangle$ type, whereas

Frank partials have Burgers vectors of $a/3\langle 111\rangle$ type. Burgers circuit analysis was performed to identify the type of partial dislocations associated with the stacking fault shown in Fig. 4.1(b) using a Burgers circuit around the partial dislocation that started and ended at the fault plane [10,13]. The Burgers vector of a partial dislocation would be a fraction of a full lattice translation. The Burgers circuit drawn around the partial dislocation in Fig. 4.1(c) yields a Burgers vector of $a/6[1\overline{1}\overline{2}]$, that makes a 90° angle with the $[110]$ dislocation line and lies completely in the plane of projection. Figure 4.1(d) shows the Burgers circuit drawn around the other partial located here in the substrate. The magnitude of the Burgers vector in projection in this case is half that of the 90° partial, i.e., $a/12[1\overline{1}\overline{2}]$, which is the projection of the true Burgers vector, i.e., $a/6[\overline{1}\overline{2}\overline{1}]$ or $a/6[21\overline{1}]$, that makes a 30° angle with the $[110]$ dislocation line. The corresponding dissociation reaction is identified as:

$$a/2[0\overline{1}\overline{1}] = a/6[\overline{1}\overline{2}\overline{1}] + a/6[1\overline{1}\overline{2}]$$

OR

$$a/2[10\overline{1}] = a/6[21\overline{1}] + a/6[1\overline{1}\overline{2}]$$

60° perfect   30° partial   90° partial

To determine whether the core of the partials belong to glide set or shuffle set, different atomic structural models need to be considered. There are three possible configurations for intrinsic stacking faults bounded by 90° and 30° partials: two belong to the shuffle set and one to the glide set [6,14]. Due to energetic considerations, the stacking fault that is upright is considered, in which case bonds in the stacking fault are

correct but horizontal bonds in the partials might be incorrect cation-cation or anion-anion bonds.

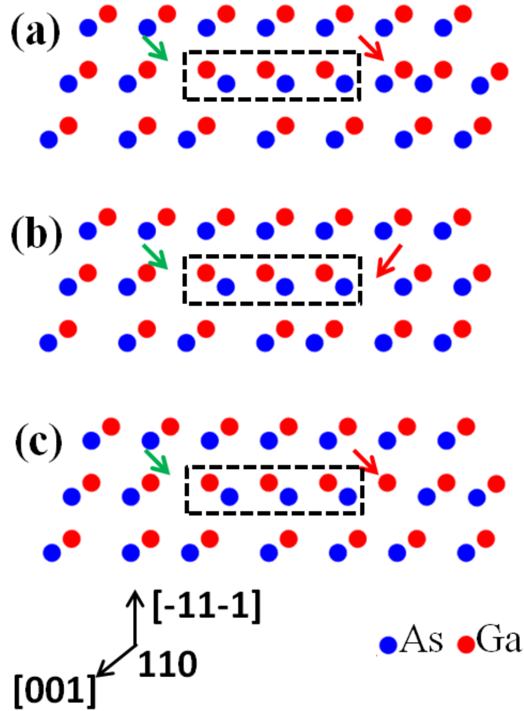

Fig. 4.2. Atomic structural models of dissociated 60° dislocation for: (a) interstitial shuffle type, (b) vacancy shuffle type, and (c) glide type. The cores of 90° and 30° partial dislocations are marked by green and red arrows, respectively. The faulted area is shown by dashed box [12].

Figures 4.2(a) and (b) show atomic models that correspond to dissociation of 60° shuffle set dislocations, whereas Fig. 4.2(c) shows a model for the dissociated 60° glide set dislocation. The faulted area is denoted by the dashed box. The 90° partial cores are left of the stacking fault, marked by green arrow, and the 30° partials are on the right, marked by red arrow. The core structure of these 90° partials is the same in all three models and all have wrong bonds at their cores. However, the core structures of the 30°

partials are all different. The shuffle-set 30° partials are of two types, namely interstitial or vacancy. The interstitial shuffle type contains a pair of cation-anion atoms at the core, as shown in Fig. 4.2(a), whereas the vacancy shuffle type is distinguished by the absence of cation-anion pairs at the core, as shown in Fig. 4.2(b). Both types have incorrect bonds at their cores. The glide-set 30° partial is characterized by the presence of unpaired cation or anion atoms with correct bonding at the core. Observation of a single, unpaired atomic column in the dislocation core of a 30° partial in atomic-resolution HAADF-STEM image would thus confirm that the dislocation belongs to glide set.

Figure 4.3(a) shows a HAADF-STEM image of a dissociated 60° misfit dislocation. The cores of the 90° and 30° partials are indicated by arrows. By identifying the crystal polarity, the resolved atomic columns can be assigned to either cation or anion, and the chemical configuration of the dislocation core can then be determined. The crystal polarity was established here by matching the experimental and simulated CBED patterns, as described in detail in Chapter 3. The image shows an unpaired Ga atomic column at the core of 30° partial that is marked by a yellow circle in the pseudo-colored magnified image in the inset of Fig. 4.3(a). This confirms that the dissociated 60° misfit dislocation at the film/substrate interface is of glide set.

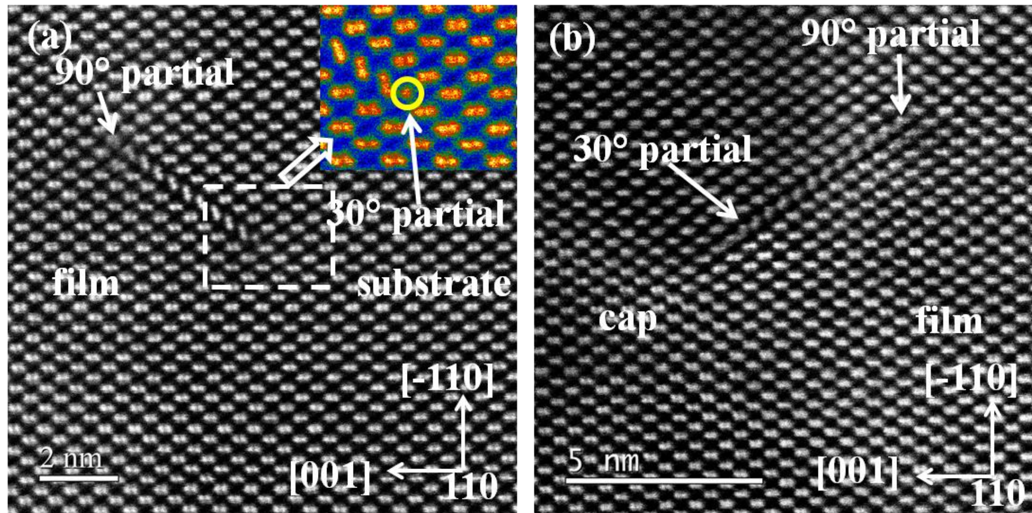

Fig. 4.3. (a) Aberration-corrected HAADF-STEM image of dissociated 60° misfit dislocation at GaAsSb/GaAs interface. The pseudo-colored magnified image of the 30° partial in inset clearly shows presence of unpaired Ga atomic column at dislocation core. (b) HAADF-STEM image of dissociated 60° misfit dislocation at cap/film interface, showing presence of single As atomic column at 30° partial dislocation core [12].

The heterostructures studied here had a 50-nm-thick capping layer of GaAs grown on $GaAs_{1-x}Sb_x$ films, and misfit dislocations could be introduced at the cap/film interface as a result of the large strain relaxation of the $GaAs_{1-x}Sb_x$ film, which would cause the build-up of strain energy in the capping layer. Thus, the creation of misfit dislocations at the cap/film interface would become energetically favorable. The tensile strain in the capping layer was relieved by misfit dislocations that have an extra half-plane in the capping layer, thus making positive dislocations. Figure 4.3(b) shows an aberration-corrected STEM image of a misfit dislocation at the cap/film interface which is again dissociated, creating an intrinsic stacking fault bounded by 90° and 30° partial dislocations. The unpaired As atomic column at the core of the 30° partial, albeit slightly

complicated possibly by the presence of kinks along the dislocation line, indicates that the misfit dislocation again belongs to the glide set.

Several theoretical investigations on the stand-off position of misfit dislocations from the interface have predicted that the dislocations should reside in the material with smaller shear modulus rather than right at the interface [15-18]. The same reasoning explains the observation of a 90° partial located in the InGaAs film of the compressively-strained InGaAs/GaAs heterostructure, which has a smaller shear modulus than GaAs [21]. Since the shear modulus of $GaAs_{0.92}Sb_{0.08}$ is less than for GaAs, the trailing 30° partial should be located right at the tensile-strained GaAs(cap)/$GaAs_{0.92}Sb_{0.08}$ interface, if not in the $GaAs_{0.92}Sb_{0.08}$ film.

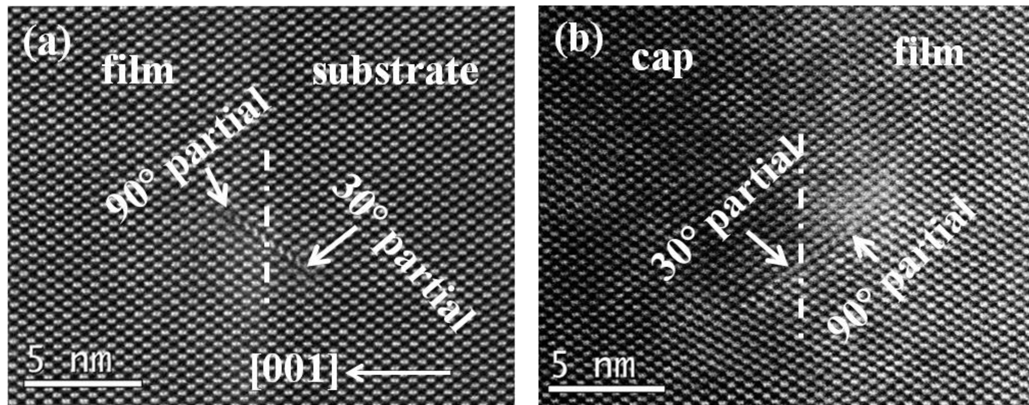

Fig. 4.4. Aberration-corrected HAADF-STEM images showing the location of 30° and 90° Shockley partials with respect to: (a) compressively-strained film/substrate interface, and (b) tensile-strained cap/film interface in GaAs/GaAsSb/GaAs heterostructure. Interface locations are shown by dashed white lines [12].

Figures 4.4(a) and (b) show the locations of two Shockley partial dislocations at the film/substrate and cap/film interfaces, respectively. The interface position was

identified by noting the background intensity of the GaAs and $GaAs_{0.92}Sb_{0.08}$ layers. The trailing 90° partial in Fig. 4.4(a) is located in the GaAsSb film at a distance of 1.6 nm from the film/substrate interface, whereas the leading 30° partial is located in the GaAs substrate at a distance of 2.1 nm from the film/substrate interface. In comparison, for the tensile-strained cap/film interface, as shown in Fig. 4.4(b), the leading 90° partial is located 2.5 nm from the interface in the GaAsSb film whereas the trailing 30° partial is pushed 1 nm from the interface into the GaAs capping layer, which has a higher shear modulus than the film. Thus, the equilibrium positions of the Shockley partial dislocations are insensitive to the shear moduli of the film and substrate since the leading partial is located in the constraining layer, whereas the trailing partial is located close to the interface in the layer undergoing relaxation for both tensile and compressively strained interfaces.

In {111} glide planes, the 90° partial dislocation lies in the same direction as the resolved shear stress whereas the 30° partial dislocation makes a 60° angle with the stress direction. Consequently, the 90° partial experiences twice as much stress as experienced by the 30° partial. The 30° partial is the leading partial dislocation under compressive stress condition and it is considered that once a 30° Shockley partial nucleates, the trailing 90° partial which experiences a greater force would quickly nucleate and terminate the fault. Under tensile stress condition, however, the 90° partial is the leading partial and since the trailing 30° partial dislocation experiences a weaker force, its nucleation can be delayed, thus effectively prolonging the dissociation width. This geometrical effect was cited to explain the narrow faults observed in the compressively-strained InGaAs/GaAs system in contrast to wider faults observed in the Si/GaP system

[19]. However, no difference in dissociation width between stacking faults lying at the compressively-strained interface and those at the tensile-strained interface was observed in the present system. The dissociation width of the faults at the compressively-strained $GaAs_{0.92}Sb_{0.08}/GaAs$ interface was measured to be 5-9 nm. The dissociation width of the stacking fault at the tensile-strained GaAs(cap)/$GaAs_{0.92}Sb_{0.08}$ interface was ~ 3-5 nm. Therefore, it can be concluded that the geometrical factor arising from the orientation of the Shockley partials with respect to the resolved shear stress direction in {111} planes, does not have any significant effect on the dissociation width of the stacking faults in the present case.

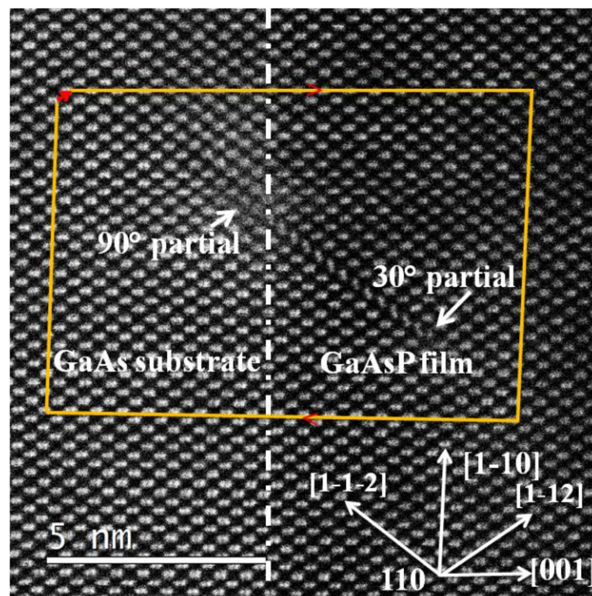

Fig. 4.5. Aberration-corrected HAADF-STEM image showing dissociated 60° dislocation at the tensile-strained film/substrate GaAsP/GaAs interface in GaAs/GaAsP/GaAs heterostructure. Interface location indicated by dashed white line.

Figure 4.5 shows an aberration-corrected HAADF-STEM image of a dissociated 60° dislocation at the film/substrate GaAsP/GaAs interface. The dissociated dislocation is

bounded by 30° and 90° Shockley partials at its two ends. The 30° Shockley partial dislocation contains a single atomic column comprised of Ga atoms in [110] projection. The approximate location of the interface has been identified based on the difference in the background intensity of the image that pertains to the film and the substrate. The GaAsP film appears darker in intensity compared to the GaAs substrate in Z-contrast HAADF-STEM imaging, which is compliant to the fact that the replacement of As by P, which is a lighter element, results in a lower average atomic number of the film than the substrate.

A RH/FS Burgers circuit is drawn encompassing the dissociated dislocation to identify the Burgers vector, which is marked by the red arrow connecting the start and the end of the Burgers circuit. The projected component of the Burgers vector is $a/4[1\bar{1}2]$. The dislocation lies in $(\bar{1}11)$fault plane, and the possible dissociation reactions are:

$$a/2[0\overline{11}] = a/6[1\bar{1}2] + a/6[\overline{12}1]$$

OR

$$a/2[10\bar{1}] = a/6[1\bar{1}2] + a/6[211]$$

60° perfect 90° partial 30° partialLomer-Cottrell locks

Lomer-Cottrell locks are formed by the interaction of two dissociated dislocations lying on intersecting {111} planes. The detailed atomic arrangement of this kind of defect is revealed by aberration-corrected HAADF-STEM images, as shown in Fig. 4.6(a). The characteristic single atomic column at the core of the 30° partial, which consist of Ga atoms in this projection, are marked by white arrows.

The 30° partials of the stacking faults at two different {111} glide planes react together to form the Lomer-Cottrell lock. The 30° partials are separated by a Ga-As pair. Combining the dissociated dislocations will yield a stair-rod dislocation and two Shockley partial dislocations of edge character. One of these reactions is:

$$a/6[1\bar{1}\bar{2}] + a/6[\bar{1}\bar{2}\bar{1}] + a/6[1\bar{1}2] + a/6[211] = a/6[1\bar{1}0] + a/6[1\bar{1}\bar{2}] + a/6[1\bar{1}2]$$

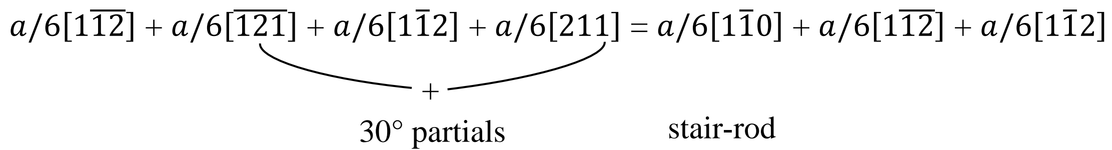

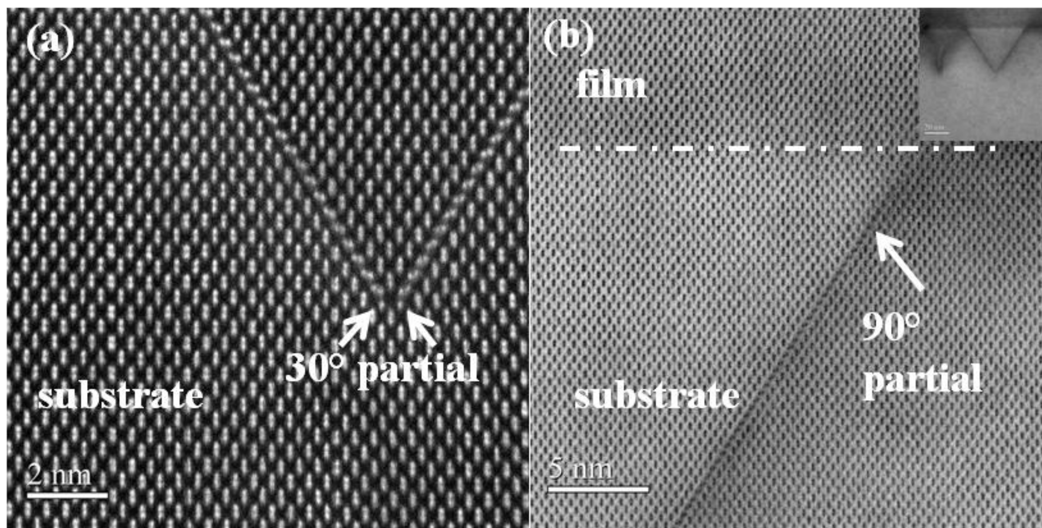

Fig. 4.6. (a) Aberration-corrected HAADF-STEM [110] projected images showing two intersecting stacking faults forming stair-rod dislocation at film/substrate interface. (d) Bright-field STEM image showing location of one 90° partial corresponding to defect complex shown in (a). The film/substrate interface is marked by white dashed line. Inset shows low magnification image illustrating that the entire defect lies in the substrate.

These dislocations have parallel edge components but an anti-parallel screw component. To illustrate this point, the Burgers vectors of the 30° Shockley partial dislocations is expressed as a combination of edge and screw components:

$$a/6[\overline{1}\overline{2}\overline{1}] = a/12[1\overline{1}\overline{2}] + a/4[\overline{1}\overline{1}0]$$

$$a/6[211] = a/12[1\overline{1}2] + a/4[110]$$

30° partial edge component screw component

The stair-rod dislocation is of edge character and lies in the (001) plane, which is not the favorable slip plane for sphalerite materials. Thus, this dislocation is considered as a sessile dislocation. Figure 4.5(b) shows that the 90° partial is located a few nanometers away from the interface in the substrate. The 30° partial is located well into the substrate. It is interesting to note that both 90° and 30° partial dislocations corresponding to the two interacting stacking faults are located in the GaAs substrate, which is unlike the case for isolated stacking faults.

The Lomer-Cottrell locks were formed at all stages of strain relaxation. However, the Hirth lock dislocation was not observed in any of the samples. In the case of Hirth lock dislocations, the two interacting 30° partials have dissimilar elements in their cores [20]. This is possible when a misfit dislocation with wrong sense of Burgers vector, formed during the process of strain relaxation, reacts with a misfit dislocation with correct sense of Burgers vector. The absence of any Hirth lock dislocations indicates that the misfit dislocations had correct Burgers vectors and helped to relieve strain at the interface.

4.3 Lomer dislocations

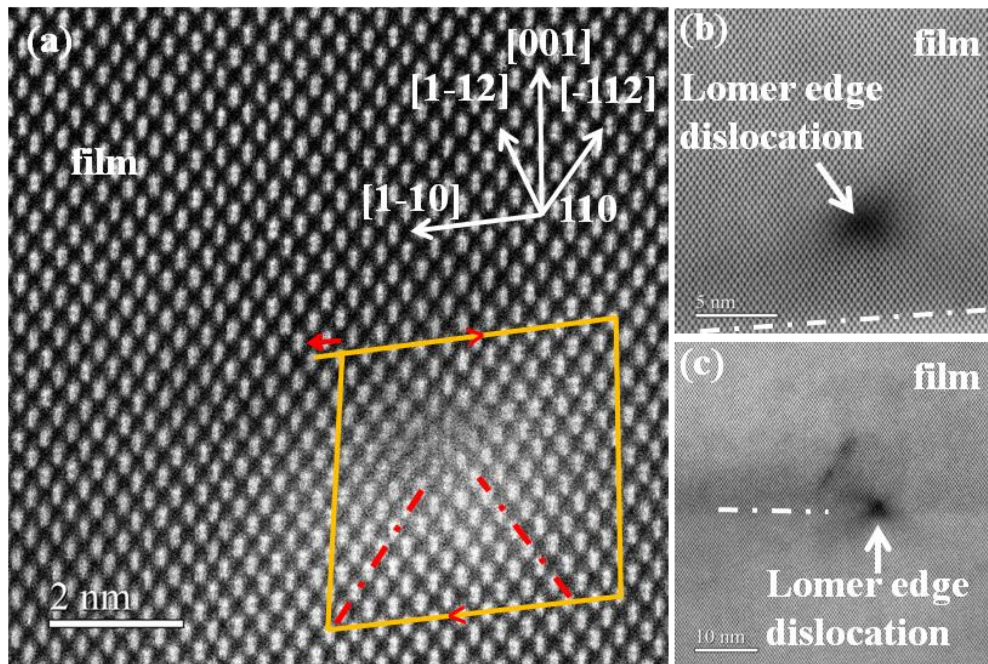

Fig. 4.7. (a) Aberration-corrected HAADF-STEM image of Lomer edge dislocation in Sample E. Bright-field STEM images showing (b) location of edge dislocation in (a) relative to strained film/substrate interface, and (c) another Lomer edge dislocation situated right at film/substrate interface of Sample F. Interfaces are marked by white dashed lines [21].

In addition to dissociated 60° dislocations, stair-rod dislocations and dislocation loops, Lomer edge dislocations with compact core structures were also observed. The Burgers vector of a perfect 90° Lomer dislocation lies in the projection plane when the dislocation is viewed in 'end-on' geometry, i.e., the dislocation line is aligned with the projection direction. Since Lomer edge dislocations are perfect dislocations, Burgers vectors of these dislocations are integer multiples of the distance between two atomic sites in the crystal lattice. Figure 4.6(a) shows an atomic-resolution HAADF-STEM

image of a Lomer edge dislocation in a GaAs/GaAsSb/GaAs heterostructure with a 500-nm-thick GaAsSb film. The Burgers vector of the dislocation was determined by Burgers circuit analysis to be $a/2[1\bar{1}0]$, following the RH/FS convention.

A possible mechanism for Lomer dislocation formation is the reaction between two perfect 60° dislocations lying on two intersecting {111} glide planes. The extra half-planes of the two 60° dislocations corresponding to $(1\bar{1}1)$ and $(\bar{1}11)$ glide planes have been highlighted in Fig. 4.7(a). The energetically favorable dislocation reaction can be written as:

$$a/2[0\overline{11}] + a/2[101] = a/2[1\bar{1}0]$$

Figures 4.7(b) and (c) are bright-field STEM images of Lomer dislocations showing the positions of the dislocation relative to the strained film/substrate interface of Samples E and F, respectively. The dislocation in Fig. 4.7(b) is located 6.5 nm away from the interface in the GaAsSb film, whereas the one in Fig. 4.7(c) is situated right at the interface. It is interesting that isolated Lomer edge dislocations were observed in many places, including several hundred nanometers into the film as well as at the interface. This random distribution appears to be indicative of their creation by stochastic interaction of threading dislocations. Their density, as observed in cross-sectional TEM samples, was much lower compared to the density of interfacial dissociated 60° dislocations. Moreover, Lomer dislocations with compact core structures were only observed in heterostructures that had undergone Stage-II and/or Stage-III relaxation.

Figure 4.8 shows a HAADF-STEM image of a dissociated dislocation at the film/substrate interface of the GaAs(cap)/$GaAs_{0.913}Sb_{0.087}$/GaAs(001) heterostructure,

which had a 1000-nm-thick film. Burgers circuit analysis was again used to identify the Burgers vectors of the various dislocations associated with the extended defect. As shown in Fig. 4.8(a), a RH/FS Burgers circuit was drawn enclosing both the partial dislocations and yielded $a/2[1\bar{1}0]$ Burgers vector, which makes a 90° angle with the [110] projection direction. Thus, the defect is a 90° dislocation that has been dissociated to create the intrinsic stacking fault. RH/FS Burger circuits starting and finishing on the fault were drawn at both ends to determine the Burgers vectors associated with each partial dislocations. The Burgers vector of the leading partial dislocation, which is located in the GaAs substrate, turns out to be $a/12[1\bar{1}2]$. This would correspond to the projected component of an actual Burgers vector of either $a/6[\overline{12}1]$ or $a/6[211]$, which makes a 30° angle to the [110] projection direction. Hence, it is a 30° Shockley partial dislocation lying in the $(\bar{1}11)$ fault plane. The extra half-plane associated with the 30° partial dislocation is terminated by a single atomic column, although it appears to be made more complicated by the possible presence of a kink along the dislocation line. From polarity determination using matching experimental and simulated CBED patterns, this atomic column consisted of Ga atoms in [110] projection, indicating again that the dislocation primarily belongs to the glide set.

The trailing partial dislocation located in the GaAsSb layer appears to be far more complex. A RH/FS Burgers circuit was drawn to identify the Burgers vector. The inset shows a magnified view of the trailing partial, where the red arrow indicates the Burgers

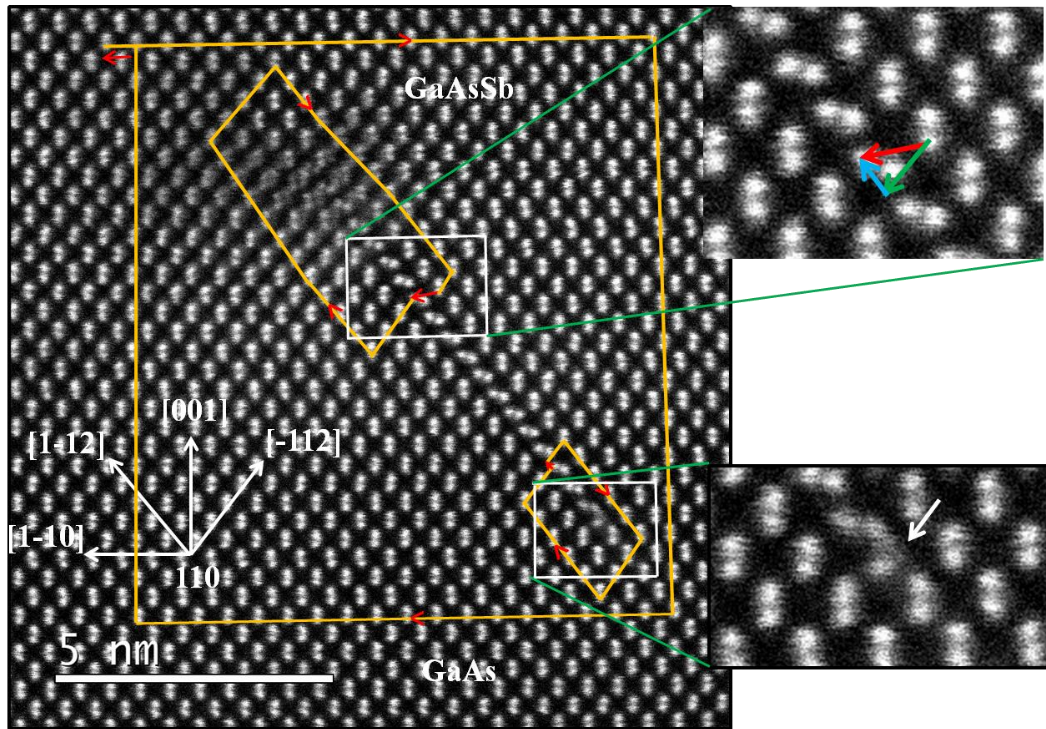

Fig. 4.8. Atomic-resolution HAADF-STEM image showing dissociated 90° dislocation at $GaAs_{0.913}Sb_{0.087}$/GaAs interface. RH/FS Burgers circuits are drawn around the fault and partial dislocations. The magnified image of boxed area around the trailing partial core shows Burgers vector (red arrow) of trailing partial as a resultant of Burgers vector (green arrow) of perfect 60° dislocation and Burgers vector (blue arrow) of 90° Shockley partial dislocation. Magnified image at the bottom portion of the image shows boxed area around 30° partial core.

vector. This Burgers vector can be thought as the resultant of the Burgers vectors of a 60° perfect dislocation and a 90° partial dislocation, as indicated by the green and cyan arrows, respectively. The Burgers vector of the 60° dislocation is either $a/2[10\overline{1}]$ or $a/2[0\overline{1}\overline{1}]$, while the Burgers vector of the 90° partial dislocation is $a/6[1\overline{1}2]$. Hence, the Burgers vector of the trailing partial can be written as:

$$a/2[10\bar{1}] + a/6[1\bar{1}2] = a/6[4\overline{11}]$$

OR

$$a/2[0\overline{11}] + a/6[1\bar{1}2] = a/6[1\overline{41}]$$

This defect can be formed by reaction between a dissociated 60° dislocation and a perfect 60° dislocation, in which case the latter reacts with the trailing 90° partial dislocation of the dissociated 60° dislocation. This dislocation reaction can be described as:

$$a/2[10\bar{1}] + a/6[1\bar{1}2] + a/6[\overline{12}1] = {}^{a}/_{2}\,[1\bar{1}0]$$

OR

$$a/2[0\overline{11}] + a/6[1\bar{1}2] + a/6[211] = {}^{a}/_{2}\,[1\bar{1}0]$$

Alternatively, the dislocation could be formed by dissociation of a perfect Lomer dislocation. The dissociation reaction can then be described as:

$$a/2[1\bar{1}0] = a/6[4\overline{11}] + a/6[\overline{12}1]$$

OR

$$a/2[1\bar{1}0] = a/6[1\overline{41}] + a/6[211]$$

In terms of elastic strain energy considerations, which are proportional to the square of the Burgers vector, the reaction between the dissociated 60° dislocation and the

perfect 60° dislocation is more energetically favorable than the dissociation of a perfect 90° dislocation.

4.4 Conclusions

The core structure of defects created at different stages of strain relaxation in GaAs/GaAsSb/GaAs(001) heterostructure have been characterized using aberration-corrected STEM. The main conclusions are as follows -

(i) Interfacial 60° misfit dislocations in low-mismatched GaAs/GaAsSb/GaAs(001) and GaAs/GaAsP/GaAs(001) heterostructures were dissociated to form intrinsic stacking faults bounded by 30° and 90° partial dislocations. Aberration-corrected STEM images clearly showed the presence of unpaired atomic columns at the cores of 30° partial dislocations, which established that these defects were primarily glide-set dislocations.

(ii) Dissociated 60° dislocations with anti-parallel screw components on intersecting {111} planes, interacted to form Lomer-Cottrell locks. Aberration-corrected STEM images revealed that the leading glide-set 30° partials had interacted to create stair-rod dislocations. The core of the stair-rod dislocation consists of single atomic columns that belong to the two leading 30° partials separated by a Ga-As pair.

(iii) Lomer edge dislocations with compact core structures were observed right at the interface and also several nm away from the interface into the GaAsSb film. Additionally, a novel dissociated edge dislocation was observed at the interface, which was bounded by a dislocation with *a*/6<411> type Burgers vector at one end and a glide-set 30° partial dislocation at the other end.

References

[1] T. Wosiński, O. Yastrubchak, A. Mąkosa, T. Figielski, J. Phys. Condens. Matter 12 (2000) 10153–10160.

[2] T. Wosiński, A. Mąkosa, T. Figielski, J. Raczyńska, Appl. Phys. Lett. 67 (1995) 1131.

[3] L.I. Fedina, A.K. Gutakovskii, T.S. Shamirzaev, J. Appl. Phys. 124 (2018).

[4] R. Hull, R. A. Logan, B. E. Weir, and J.M. Vandenberg, Appl. Phys. Lett. 63 (1993) 1504.

[5] D.B. Williams, C.B. Carter, Transmission Electron Microscopy: A Textbook for Materials Science, second ed., Springer, New York, 2009.

[6] J. Hornstra, J. Phys. Chem. Solids 5 (1958) 129–141.

[7] V. V. Bulatov, Scripta. Mat. 45 (2001) 1247–1252.

[8] O.L. Krivanek, N. Dellby, A.R. Lupini, Ultramicroscopy 78 (1999) 1–11.

[9] M. Haider, H. Rose, S. Uhlemann, B. Kabius, K. Urban, J. Electron Microsc. 47 (1998) 395–405.

[10] Y. Arroyo Rojas Dasilva, R. Kozak, R. Erni, M.D. Rossell, Ultramicroscopy 176 (2017) 11–22.

[11] Y. Arroyo Rojas Dasilva, M.D. Rossell, F. Isa, R. Erni, G. Isella, H. von Känel, P. Gröning, Scripta. Mat. 127 (2017) 169–172.

[12] A. Gangopadhyay, A. Maros, N. Faleev, D.J. Smith, Scripta. Mat. 153 (2018) 77–80.

[13] J. P. Hirth, J. Lothe, Theory of Dislocations, second ed., Wiley, New York, 1982.

[14] D.B. Holt, J. Phys. Chem. Solids 23 (1962) 1353–1362.

[15] M.Y. Gutkin, M. Militzer, A.E. Romanov, V.I. Vladimirov, Phys. Stat. Sol. 113 (1989) 337–344.

[16] X. Wu, G.C. Weatherly, Semicond. Sci. Technol. 18 (2003) 307–311.

[17] J. Zou, D.J.H. Cockayne, Appl. Phys. Lett. 63 (1993) 2222–2224.

[18] W. Mader, D. Knauss, Acta Metall. 40 (1992) S207-S215.

[19] P.M.J. Marée, J.C. Barbour, J.F. Van Der Veen, K.L. Kavanagh, C.W.T. Bulle-Lieuwma, M.P.A. Viegers, J. Appl. Phys. 62 (1987) 4413–4420.

[20] T. Paulauskas, C. Buurma, E. Colegrove, B. Stafford, Z. Guo, M.K.Y. Chan, C. Sun, M.J. Kim, S. Sivananthan, R.F. Klie, Acta Cryst. 70 (2014) 524–531.

[21] A. Gangopadhyay, A. Maros, N. Faleev, D.J. Smith, Acta Mater. 162 (2019) 103-115.

CHAPTER 5

ATOMIC-RESOLUTION STRUCTURAL IMAGING OF INTERFACIAL DEFECTS IN GaSb/GaAs(001) HETEROSTRUCTURE

5.1 Introduction

The growth of GaSb/GaAs(001) heterostructures has been the subject of ongoing attention due to the band alignment and high electron mobility, which are useful for optoelectronic device applications [1,2]. The large difference in lattice parameter (7.8%) between GaSb and GaAs combined with differences in thermal expansion coefficients cause high misfit strain at the interface, which results in a critical thickness of ~4 Å. Beyond the critical thickness, the misfit strain at the GaSb/GaAs(001) interface is reported to be relieved by either a two-dimensional interfacial array of 90° Lomer dislocations [3,4], or a mixture of 60° and 90° dislocations [5]. Threading dislocations, which are deleterious for device performance, are associated primarily with the 60° dislocations. Hence, the density of threading dislocations should be orders of magnitude less when the misfit strain is relieved exclusively by an interfacial array of Lomer dislocations in [110] and $[1\bar{1}0]$ directions [6]. The core structures of these interfacial defects are important because the detailed atomic arrangements determine the associated defect states in the band gap. Additionally, knowledge of the core structure may shed light on the formation mechanism of the Lomer dislocations [7].

High-resolution electron microscopy offers the unique advantage of being able to image dislocation cores at very high spatial resolution, and the technique has previously

been widely used for many years to reveal the atomic structure of dislocation cores in semiconductor heterostructures [8]. The recent generations of aberration-corrected electron microscopes (ACEMs) have the capability to routinely produce images with sub-angstrom level resolution, which enables direct atomic-structure imaging of dislocation cores in many semiconductors [9], as also shown in previous chapters for the GaAs/GaAsSb/GaAs heterostructures. This chapter concentrates on atomic-scale characterization of interfacial defects occurring in an isovalent GaSb/GaAs(001) heterostructure, using aberration-corrected scanning TEM.

The GaSb/GaAs sample studied was provided by the group of Prof. Ganesh Balakrishnan at University of New Mexico. Cross-section TEM samples were prepared using mechanical polishing, dimpling and argon ion milling. Conventional TEM images were obtained using the JEOL 2010F microscope operated at 200 kV. Atomic-resolution STEM imaging was carried out using the JEOL ARM-200F microscope also operated at 200 kV, as described previously.

5.2 Results and discussion

Figure 5.1(a) shows a bright-field TEM micrograph of the GaSb/GaAs(001) heterostructure. A high density of threading defects and stacking faults is present in the GaSb layer. As expected, the GaSb/GaAs interface also exhibits a high density of defects. Aberration-corrected STEM imaging was used to examine the atomic structure of the interfacial defects, and Fig. 5.1(b) shows a typical atomic-resolution HAADF-STEM image of the GaSb/GaAs interface region. Several different types of interfacial defects can be identified, including 60° and Lomer dislocations, as well as a short {111}-type intrinsic stacking fault propagating upwards from the plane of the interface.

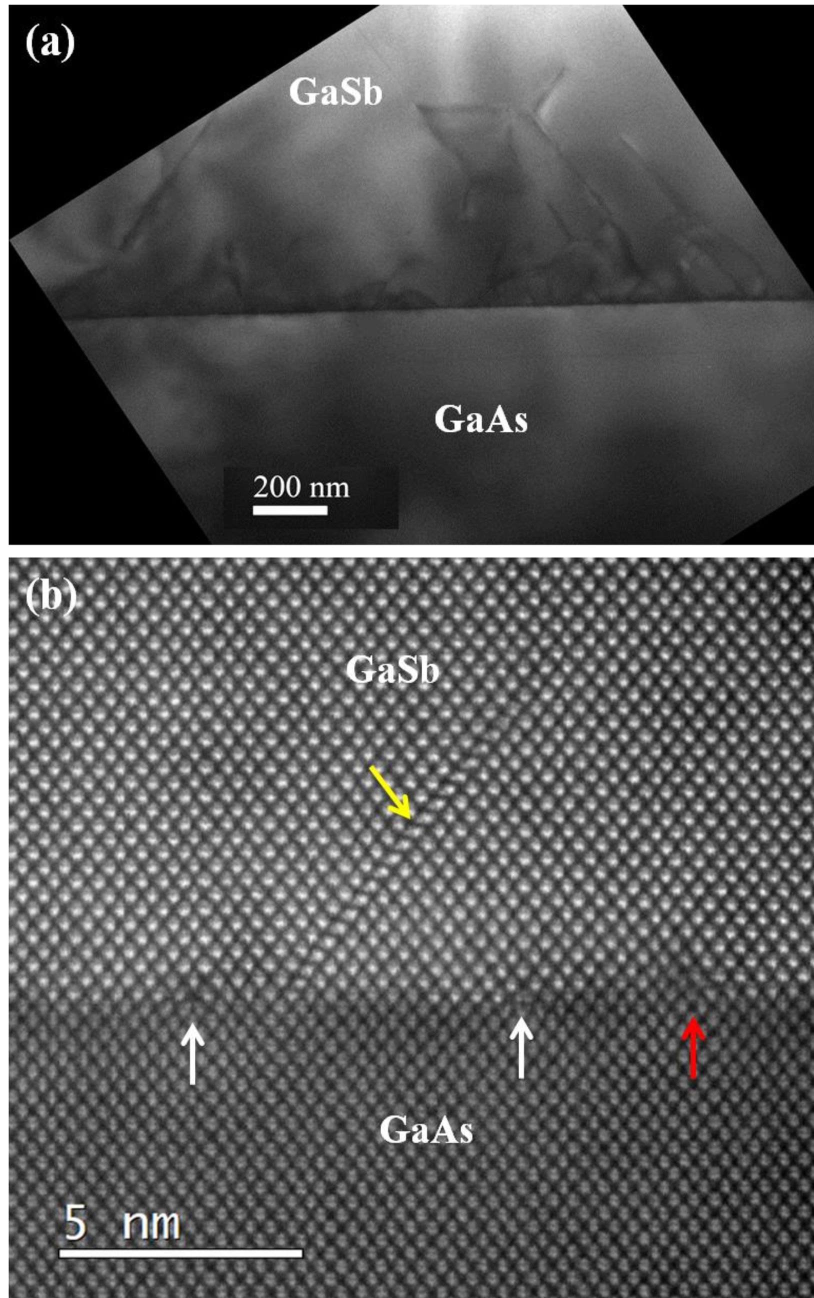

Fig. 5.1. (a) TEM micrograph of GaSb/GaAs(001) heterostructure revealing the crystalline quality and defect structure of the GaSb layer. (b) Atomic-resolution HAADF-STEM structural image of GaSb/GaAs heterointerface region showing short {111}-type intrinsic stacking fault (yellow arrow), 60° dislocation (red arrow) and two Lomer dislocations (white arrows).

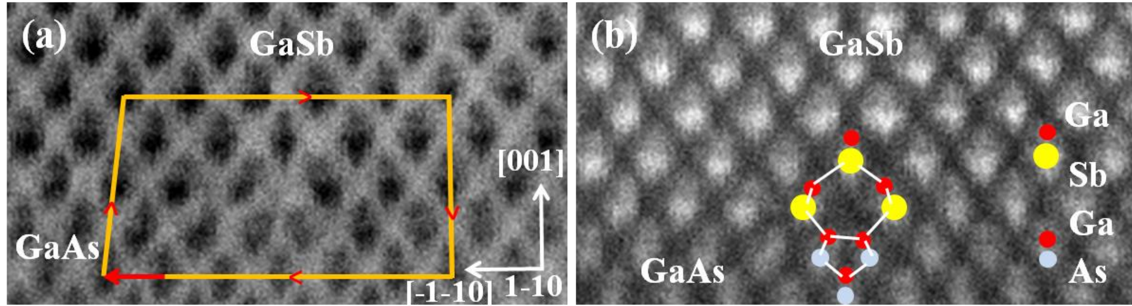

Fig. 5.2. (a) Atomic-resolution LABF-STEM structural image of interfacial dislocation at GaSb/GaAs interface, together with corresponding RH/FS Burgers circuit. (b) HAADF-STEM image of the same defect with structural model overlaid on the dislocation depicting the five-membered and seven-membered atomic ring arrangements at the defect core.

Figure 5.2(a) shows a large-angle bright-field (LABF) STEM image of an interfacial defect at the GaSb/GaAs interface. The Burgers vector of the defect is determined by drawing a RH/FS (right-hand/finish-start) Burgers circuit, and the arrow joining the finishing and starting points of the circuit indicates the Burgers vector. Thus, the Burgers vector here is identified to be $a/2[\bar{1}\bar{1}0]$, according to the directions shown on the figure, which constitutes a full lateral lattice translation. This perfect 90° dislocation is known as a Lomer edge dislocation, since the $[1\bar{1}0]$ dislocation line direction, which is also the beam projection direction, makes a 90° angle with the $[\bar{1}\bar{1}0]$ Burgers vector direction. The atomic arrangements at the dislocation core can be directly determined based on the atomic-column intensities in the HAADF-STEM image of the same defect shown in Fig. 5.2(b). As represented by the schematic, the dislocation core consists of five-membered and seven-membered rings of atoms. This atomic arrangement corresponds to the shuffle-set variant of the two types of core structures of edge

dislocations in diamond-cubic crystals, as originally proposed by Hornstra [10] and also previously reported for the GaSb/GaAs interface by Wang et al. [11].

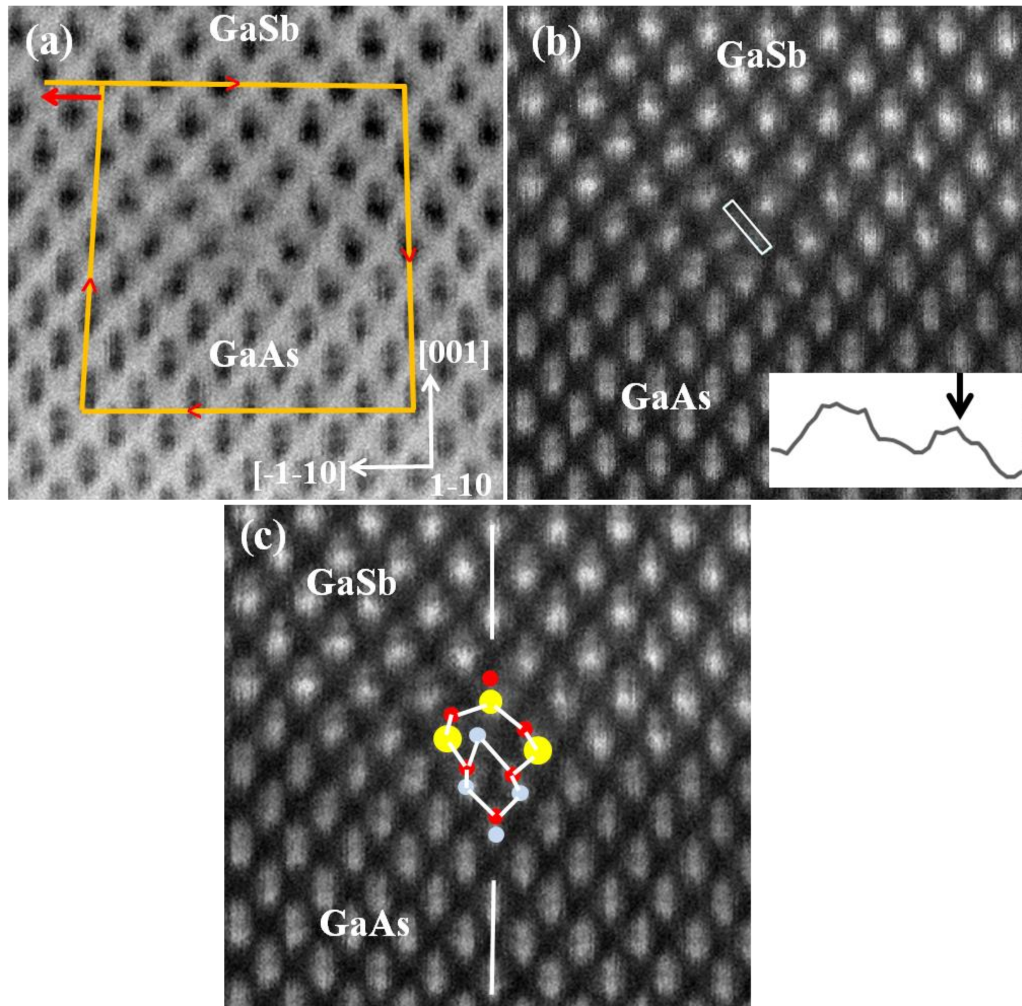

Fig. 5.3. (a) Atomic-resolution LABF-STEM image of dislocation located at GaSb/GaAs interface with corresponding RH/FS Burgers circuit. (b) HAADF-STEM image of the dislocation core and intensity profile (inset) revealing two distinct peaks corresponding to separate atomic columns. (c) Proposed atomic arrangement at dislocation core overlaid on HAAD F-STEM image.

Figure 5.3(a) shows an atomic-resolution LABF-STEM image of another defect located at the GaSb/GaAs interface. A RH/FS Burgers circuit was drawn encompassing the defect in order to identify the Burgers vector, which was again determined to be $a/2[\bar{1}\bar{1}0]$, corresponding to a Lomer dislocation. Figure 5.3(b) includes an intensity profile across the HAADF STEM image of the same defect. This profile confirms the existence of single atomic column at the core, which is displaced slightly towards the left-hand side with respect to the $\{220\}$ median plane (marked by solid white vertical lines in Fig. 5.3(c)). Figure 5.3(c) depicts schematically the atomic arrangements at the dislocation core, which consist in this case of six-membered and eight-membered rings of atoms. This atomic configuration corresponds to the glide-set variation of a Lomer dislocation, as originally proposed by Hornstra [10], and is formally identified as a left-displaced glide-set Lomer dislocation.

Figure 5.4(a) shows an aberration-corrected LABF-STEM structure image of yet another defect located at the GaSb/GaAs(001) interface, associated in this case with an interface step. A RH/FS Burgers circuit drawn around the dislocation again identifies the Burgers vector as $a/2[\bar{1}\bar{1}0]$. This Burgers vector is equivalent to a full lattice translation with a 90° angle with the $[1\bar{1}0]$ dislocation line direction, and thus the defect is confirmed to be a Lomer edge dislocation. Figure 5.4(b) includes an intensity profile that indicates the presence of an atomic column at the core (marked by the arrow), albeit displaced slightly towards the right with respect to the $\{220\}$ median plane (marked by the solid white lines in Fig. 5.4(c)). The atomic arrangement of the dislocation core, based on the contrast of the HAADF-STEM image, is shown schematically in Fig. 5.4(c). The dislocation core consists of six-membered and eight-membered rings of atoms.

Careful observation of the intensity profile across the interface indicates that the dislocation is associated with an interfacial atomic step, as shown in Fig. 5.4(c). Thus, this specific dislocation is identified as a right-displaced glide-set Lomer dislocation that incorporates an atomic step on one side of the defect.

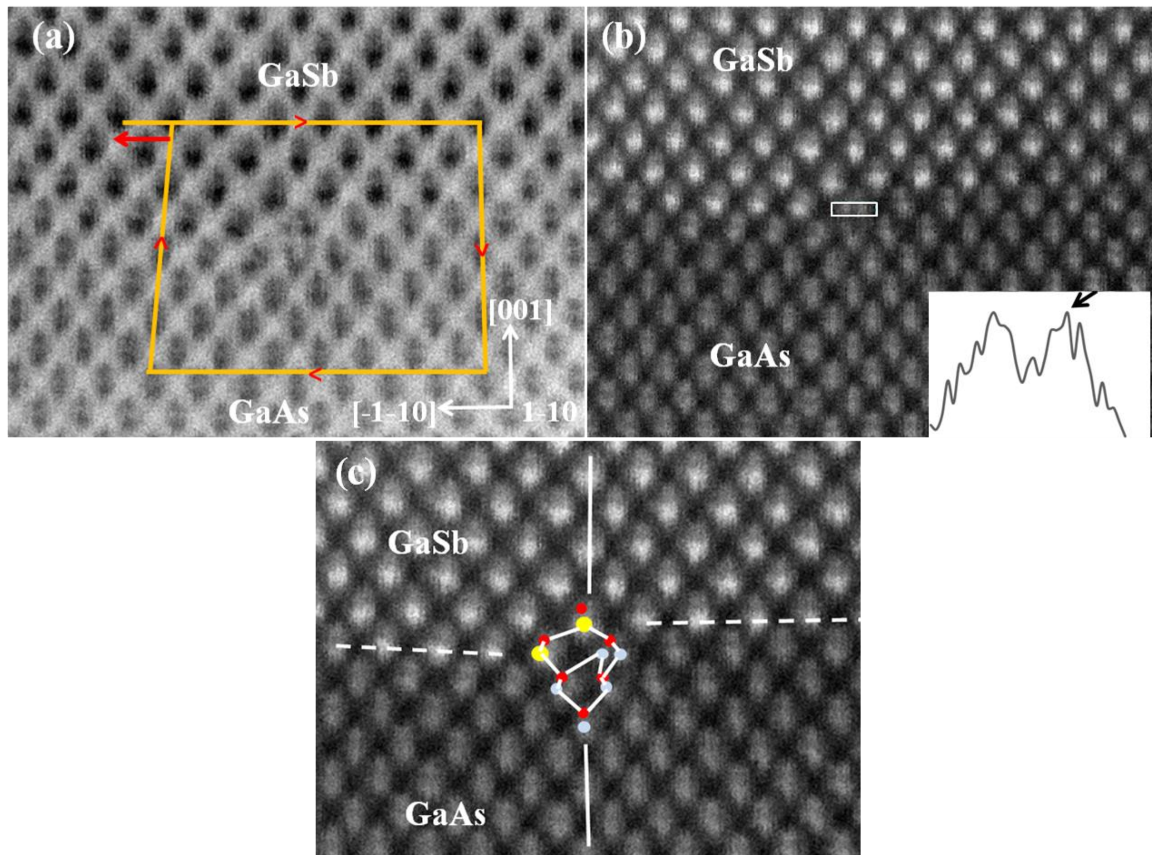

Fig. 5.4. (a) Aberration-corrected LABF-STEM image of interfacial dislocation at GaSb/GaAs interface with corresponding RH/FS Burgers circuit. (b) HAADF-STEM image and intensity profile from HAADF-STEM image of dislocation core revealing two distinct peaks (the one corresponding to the atom centrally located in the defect core is marked by arrow in the inset). (c) Proposed atomic arrangement of defect core overlaid on HAADF-STEM image. Dotted line shows location of GaSb/GaAs interface.

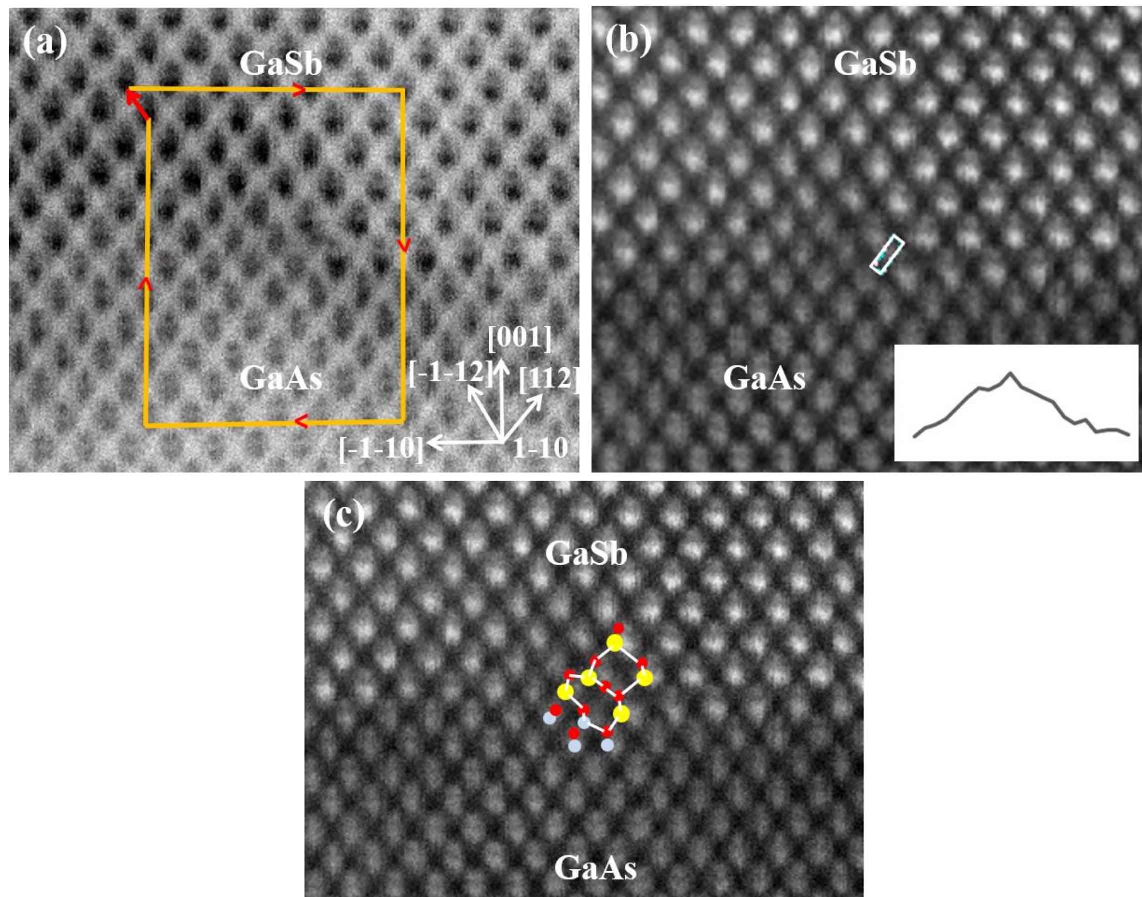

Fig. 5.5. (a) Aberration-corrected LABF-STEM structure image of interfacial defect in the GaSb/GaAs heterostructure with corresponding RH/FS Burgers circuit. (b) HAADF-STEM image and intensity profile obtained from HAADF-STEM image reveal single atomic peak at defect core. (c) Proposed atomic arrangement of defect core overlaid on HAADF-STEM image.

Figure 5.5(a) shows an atomic-resolution LABF-STEM image of a fourth type of GaSb/GaAs interfacial defect, together with the corresponding RH/FS Burgers circuit. The closure vector here is identified as $^{a}/_{4}\,[\bar{1}\bar{1}2]$, according to the directions shown on Fig. 5.5(a). This arrangement would correspond to the projected component of a 60° dislocation with a Burgers vector of either $a/2[\bar{1}01]$ or $a/2[0\bar{1}1]$, which lies in a (111)

slip plane. Figure 5.5(b) includes an intensity profile from the HAADF-STEM image of the dislocation core, which confirms the presence of a single atomic column at the defect core. Figure 5.5(c) shows a model of the dislocation core overlaid on the HAADF-STEM image showing the most probable atomic arrangement. The presence of the single As atomic column at the core confirms that the dislocation belongs primarily to the glide-set [12].

Figure 5.6 shows an atomic-resolution HAADF-STEM image of a stacking fault originating at the GaSb/GaAs(001) interface, and extending upwards into the GaSb layer. A RH/FS Burgers circuit was drawn to encompass the partial dislocations at both ends of the dissociated defect. The closure vector here is identified as $a/_4\,[\overline{11}\overline{2}]$, which would be the projected component of either $a/2[0\overline{1}\overline{1}]$ or $a/2[\overline{1}0\overline{1}]$ Burgers vectors of an undissociated 60° dislocation that lies in a $(\overline{11}1)$ slip plane. Thus, this 60° dislocation has dissociated into 30° Shockley partial and 90° Shockley partial dislocations, as observed previously for the GaAsSb/GaAs(001) heterostructures. The dissociation reaction can be written as:

$$a/2[0\overline{1}\overline{1}] = a/6[1\overline{2}\overline{1}] + a/6[\overline{1}\overline{1}\overline{2}]$$

OR

$$a/2[\overline{1}0\overline{1}] = a/6[\overline{2}1\overline{1}] + a/6[\overline{1}\overline{1}\overline{2}]$$

60° perfect 30° partial 90° partial

The 30° partial is the leading partial dislocation and is located right at the compressively-strained GaSb/GaAs interface. The core of the 30° Shockley partial dislocation contains

the characteristic single atomic column, identified here as corresponding to Sb, indicating that the dislocation belongs to glide-set. The corresponding 90° Shockley partial dislocation, which is the associated trailing partial dislocation, is located in the GaSb layer.

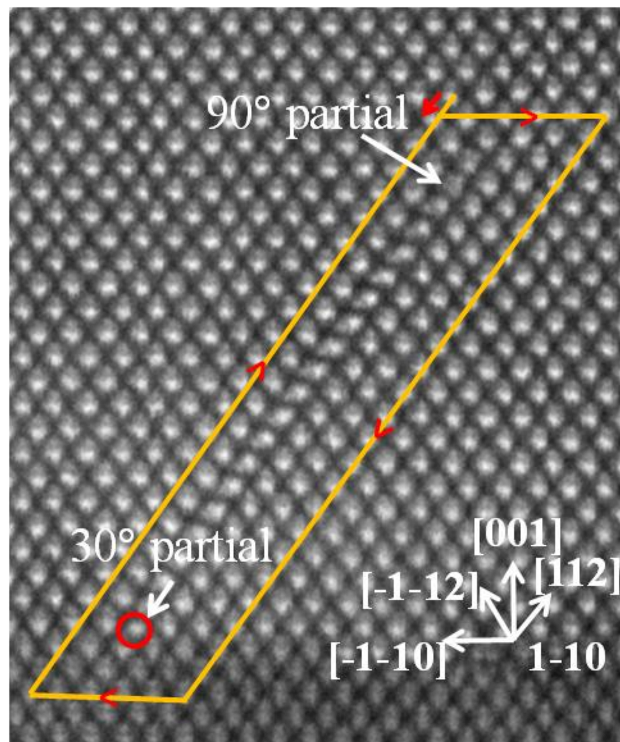

Fig. 5.6. Aberration-corrected HAADF-STEM image of dissociated 60° dislocation at the GaSb/GaAs(001) interface and corresponding RH/FS Burgers circuit.

Once the different types of defects and the atomic arrangements of their core had been identified, their relative frequency of occurrence at the interface was determined. Out of the eighteen analyzed defects, twelve were classic 5-7 ring shuffle-set Lomer dislocations, two defects were left-displaced 6-8 ring glide-set Lomer dislocations, one was right-displaced 6-8 ring glide-set Lomer dislocation, two were perfect 60° dislocations and one was a dissociated 60° dislocation. The average distance between the

Lomer dislocations at the interface was measured to be 6.0 ± 0.5 nm. The Lomer dislocations were not regularly spaced along the interface, most likely because of the occurence of the different defect types as well as the presence of interface steps. However, only a relative few were associated with these monolayer steps at the interface, indicating that the presence of an interface step was not a prerequisite for formation of a Lomer dislocation.

5.3 Summary

The interfacial defects present in a GaSb/GaAs(001) heterostructure have been characterized and their core structures have been determined using aberration-corrected STEM structure images. Several types of defects, including Lomer edge dislocations, perfect 60° dislocations and dissociated 60° dislocations were identified using Burgers circuit analysis. The majority (83%) of the eighteen analyzed interfacial defects were perfect 90° Lomer dislocations. These defects interestingly had three different types of core structure: the well-known 5-7 ring shuffle-set, as well as the 6-8 ring left-displaced glide-set and the 6-8 ring right-displaced glide-set. The 5-7 ring shuffle-set Lomer dislocations were the most commonly observed, but no symmetric glide-set Lomer dislocations were seen. The presence of single atomic columns at the core of the perfect 60° dislocation, and at the core of the 30° Shockley partial of the dissociated 60° dislocation, indicated that both of these defects belonged to the glide set.

References

[1] B.R. Bennett, R. Magno, J.B. Boos, W. Kruppa, M.G. Ancona, Solid. State. Electron. 49 (2005) 1875–1895.

[2] G.T. Nelson, B.C. Juang, M.A. Slocum, Z.S. Bittner, R.B. Laghumavarapu, D.L. Huffaker, S.M. Hubbard, Appl. Phys. Lett. 111 (2017) 231104.

[3] S. Huang, G. Balakrishnan, D.L. Huffaker, J. Appl. Phys. 105 (2009) 103104.

[4] S.H. Huang, G. Balakrishnan, A. Khoshakhlagh, A. Jallipalli, L.R. Dawson, D.L. Huffaker, Appl. Phys. Lett. 88 (2006) 131911.

[5] W. Qian, M. Skowronski, R. Kaspi, M. De Graef, V.P. Dravid, J. Appl. Phys. 81 (1997) 7268–7272.

[6] A. Jallipalli, G. Balakrishnan, S.H. Huang, T.J. Rotter, K. Nunna, B.L. Liang, L.R. Dawson, D.L. Huffaker, Nanoscale Res. Lett. 4 (2009) 1458–1462.

[7] Y.B. Bolkhovityanov, A.S. Deryabin, A.K. Gutakovskii, L. V. Sokolov, A.P. Vasilenko, Acta Mater. 61 (2013) 5400–5405.

[8] A. Vilà, A. Cornet, J.R. Morante, P. Ruterana, M. Loubradou, R. Bonnet, Y. González, L. González, Philos. Mag. A 71 (1995) 85–103.

[9] D.J. Smith, Prog. Cryst. Growth Charact. Mater. 66 (2020) 100498.

[10] J. Hornstra, J. Phys. Chem. Solids. 5 (1958) 129–141.

[11] Y. Wang, P. Ruterana, J. Chen, S. Kret, S. El Kazzi, C. Genevois, L. Desplanque, X. Wallart, ACS Appl. Mater. Interfaces 5 (2013) 9760–9764.

[12] A.J. McGibbon, S.J. Pennycook, J.E. Angelo, Science 269 (1995) 519–522.

CHAPTER 6

SUMMARY AND FUTURE WORK

6.1 Summary

The research of this dissertation has involved a comprehensive study of strain relaxation mechanisms in low-mismatched $GaAs/GaAs_{1-x}Sb_x/GaAs(001)$ heterostructures primarily using transmission electron microscopy. Atomic-scale characterization of interfacial defects in low-mismatched GaAs(001)-based heterostructures and high-mismatched GaSb/GaAs(001) heterostructures using aberration-corrected scanning transmission electron microscopy was also performed, and their core structure was studied in detail.

The thickness of the GaAsSb films in $GaAs/GaAs_{1-x}Sb_x/GaAs(001)$ ($x\sim0.08$) heterostructures was varied in the range of 50 nm to 4000 nm in order to understand the creation and evolution of defects and to investigate strain relaxation mechanisms in these heterostructures. Three distinct stages of strain relaxation were identified. Diffraction contrast analysis of plan-view TEM samples using *g.b* method revealed that Stage-I relaxation exhibited a sluggish relaxation rate primarily rendered by the motion of 60° dislocations propagating along two orthogonal <110> directions. Many curved dislocations were formed in Stage-II and Stage-III relaxation, and majority of them extended into the substrate. In heterostructures with thicker films (500-nm-thick and onwards), the capping layer exhibited Stage-I relaxation by the formation of 60° dislocations at the cap/film interface. Dislocation densities in the capping layers were measured from plan-view TEM samples. It was noted that the dislocation density

decreased in the heterostructure with 4000-nm-thick film in comparison to the heterostructure with 2000-nm-thick film even though the misfit strain increased. To understand this anomalous result, three different sources of dislocations in the capping layer were considered: i) macroscopic double-kink motion of a threading dislocation; ii) single-kink motion of a threading dislocation in the capping layer, which is blocked at the film/substrate interface; and iii) single-kink motion of threading dislocations that are generated from the surface troughs as dislocation half-loops. A detailed consideration of these nucleation mechanisms by calculation of theoretical excess stress for single-kink and double-kink motion of threading dislocations, in conjunction with experimental evidence obtained using TEM characterization of these heterostructures and AFM characterization of sample surfaces, led to the conclusion that nucleation of dislocation half-loops was the dominant nucleation mechanism in these heterostructures.

Atomic-resolution HAADF-STEM images of interfacial defects in GaAs(001)-based low-mismatched heterostructures were analyzed to characterize the defects and understand their core structure. Burgers circuit analysis indicated that the interfacial 60° dislocations, both at compressively-strained film/substrate interface and tensile-strained cap/film interfaces of GaAs/GaAsSb/GaAs heterostructures, and at the tensile-strained film/substrate interfaces of GaAs/GaAsP/GaAs heterostructures, were dissociated to form intrinsic stacking faults bounded by 30° and 90° Shockley partial dislocations. The core of the 30° Shockley partial dislocation contained a single atomic column. Comparison with established models of dissociated 60° dislocations indicated that these dislocations primarily belonged to the glide set. In addition to isolated stacking faults, the leading 30° Shockley partial dislocations of two dissociated 60° dislocations on intersecting glide

planes interacted to form Lomer-Cottrell lock at the compressively-strained GaAsSb/GaAs interface. Aberration-corrected STEM images of such defect configuration revealed that the core of the stair-rod dislocations contained single atomic columns corresponding to two 30° partial dislocations of identical polarity separated by a Ga-As pair. Additionally, Lomer dislocations with compact core structure were observed at the interface as well as inside the film, indicating the stochastic nature of formation of Lomer dislocations. A novel type of dissociated 90° dislocation bounded by a 30° Shockley partial dislocation and a *a*/6<411> type partial dislocation was also observed at the compressively-strained GaAsSb/GaAs interface.

Interfacial defects formed at the high-mismatched GaSb/GaAs(001) hetero-interface were imaged with aberration-corrected STEM. While the majority of the defects were perfect 90° dislocations, perfect 60° and dissociated 60° dislocations were also observed. Three different types of 90° Lomer dislocations were identified. The classic 5-7 atomic-ring shuffle set dislocation, the left-displaced 6-8 atomic-ring glide-set dislocation and the right-displaced 6-8 atomic-ring glide-set dislocation. The shuffle-set Lomer dislocations were the most commonly observed among these three dislocation types. Single atomic columns were observed at the core of the both perfect 60° and 30° Shockley partial dislocation corresponding to the dissociated 60° dislocations indicating that these dislocations primarily belonged to glide set.

6.2 Future work

Cross-hatch morphology is characteristically formed in relaxed low-mismatched heterostructures that combine diamond-cubic/sphalerite semiconductor materials. In this dissertation, it has been argued that dislocation half-loops nucleated at the surface troughs

are the major source of threading dislocations in these heterostructures. AFM surface images of the heterostructures with 2000-nm-thick and 4000-nm-thick films showed that a substantial smoothening of the surface had occurred in the latter compared to the former. This surface smoothening appeared to be correlated with a decrease in misfit dislocation density at the cap/film interface. Further experiments are needed to validate this correlation. Thermal annealing could be performed to achieve smoothening of the growth front after deposition of the film is completed and the capping layer should then be deposited. The duration of thermal annealing should be the same time taken to grow a film at a growth rate of 2 Å/s, i.e., ~167 minutes and the holding temperature should be 500°C, which is the temperature at which the film was grown in the experiments described here. AFM characterization of the heterostructure surface after the annealing and determination of dislocation density from plan-view TEM images of the cap/film interface should be performed so that a comparison can be made with the surface morphology and dislocation density at the cap/film interface of the GaAs/GaAsSb/GaAs heterostructure with the 4000-nm-thick GaAsSb film.

The core structure of dislocations has been studied using aberration-corrected STEM technique. However, a major limitation of this approach of viewing dislocations with ‘end-on’ geometry is that any variation of the dislocation core structure along the dislocation line which coincides with the beam projection direction, cannot be directly visible or interpreted from the 2D projected image. Recently, depth-dependent imaging in HAADF-STEM imaging mode has become possible due to better depth resolution achievable as a result of larger convergence angles [1]. Depth-dependent imaging in conjunction with simulated images of different possibilities of dislocation core structure

could be used to identify the possible presence of reconstruction related defects, kinks along the dislocation line, or any possible switch in the particular set (glide or shuffle) to which the dislocation belongs.

Defect states that are deep in the band gap are effective for non-radiative recombination of electron-hole pairs and can be therefore very detrimental for device performance. The determination of the location of the defect state within the band gap would thus be useful to identify defects that are more detrimental to device performance. These defect states are dependent on the atomic configuration at the defect core, which could be determined by transmission electron microscopes with sub-angstrom level spatial resolution [2-4]. Monochromated electron energy-loss spectroscopy has recently been used to identify bandgap states related to point defects [5,6]. Electron energy-loss spectroscopy in an aberration-corrected STEM has recently been applied to identify the atomic and electronic structure of Shockley partial dislocations associated with dissociated 60° misfit dislocations [7]. However, bandgap state determination of commonly observed 5-7 atomic ring shuffle-set and/or 6-8 glide-set type Lomer dislocations in high-mismatched semiconductor heterostructures using monochromated EELS with an aberration-corrected STEM has yet to be reported and would be worth pursuing.

References

[1] A.Y. Borisevich, A.R. Lupini, S.J. Pennycook, Proc. Natl. Acad. Sci. 103 (2006) 3044-3048.

[2] H. Yang, J.G. Lozano, T.J. Pennycook, L. Jones, P.B. Hirsch, P.D. Nellist, Nat. Commun. 6 (2015) 1–7.

[3] H. Du, C.L. Jia, L. Houben, V. Metlenko, R.A. De Souza, R. Waser, J. Mayer, Acta Mater. 89 (2015) 344–351.

[4] T. Paulauskas, C. Buurma, E. Colegrove, B. Stafford, Z. Guo, M.K.Y. Chan, C. Sun, M.J. Kim, S. Sivananthan, R.F. Klie, Acta Crystallogr. Sect. A Found. Adv. 70 (2014) 524–531.

[5] S. Wang, K. March, F.A. Ponce, P. Rez, Phys. Rev. B 99 (2019) 115312.

[6] W.J. Bowman, K. March, C.A. Hernandez, P.A. Crozier, Ultramicroscopy 167 (2016) 5-10.

[7] P.E. Batson, M.J. Lagos, Ultramicroscopy 180 (2017) 34–40.

LIST OF REFERENCES

D.A. Neaman, Semiconductor Physics and Devices: Basic Principles, fourth ed., McGraw-Hill, New York, 2003.

A.W. Bett, F. Dimroth, G. Stollwerck, O. V. Sulima, Appl. Phys. A Mater. Sci. Process. 69 (1999) 119–129.

F. Capasso, Science 235 (1987) 172–176.

C.S. Schnohr, Appl. Phys. Rev. 2 (2015) 031304.

J.A. Venables, Introduction to Surface and Thin Film Processes, second ed., Cambridge University Press, 2000.

C.P. Kuo, S.K. Vong, R.M. Cohen, G.B. Stringfellow, J. Appl. Phys. 57 (1985) 5428–5432.

H. Morkoç, B. Sverdlov, G.B. Gao, Proc. IEEE 81 (1993) 493–556.

J.W. Matthews, S. Mader, T.B. Light, J. Appl. Phys. 41 (1970) 3800–3804.

W.T. Read, Jr., Philos. Mag. 45 (1954) 775–796.

A.D. Krnttz, S.A. Kulrn, A.L. Avernacht, Phys. Rev. 101 (1956).

R. Hull, J.C. Bean, Crit. Rev. Solid State Mater. Sci. 17 (1992) 507–546.

E.A. Fitzgerald, Mater. Sci. Reports 7 (1991) 87–140.

J. P. Hirth, J. Lothe, Theory of Dislocations, second ed., Wiley, New York, 1982.

J.C. Bean, T.T. Sheng, L.C. Feldman, A.T. Fiory, R.T. Lynch, Appl. Phys. Lett. 44 (1984) 102-104.

J.Y. Tsao, B.W. Dodson, Appl. Phys. Lett. 53 (1988) 848–850.

B.W. Dodson, J.Y. Tsao, Appl. Phys. Lett. 51 (1987) 1325–1327.

D.C. Houghton, J. Appl. Phys. 70 (1991) 2136–2151.

D.J. Eaglesham, E.P. Kvam, D.M. Maher, C.J. Humphreys, D.J. Eaglesham, D.M. Maher, J.C. Bean, Philos. Mag. 59 (1989) 1059–1073.

M. Albrecht, S. Christiansen, J. Michler, W. Dorsch, H.P. Strunk, P.O. Hansson, E. Bauser, Appl. Phys. Lett. 67 (1995) 1232.

R. Hull, J.C. Bean, J. Vac. Sci. Technol. A 7 (1989) 2580–2585.

V. Higgs, P. Kightley, P.J. Goodhew, P.D. Augustus, Appl. Phys. Lett. 59 (1991) 829-831.

L.B. Freund, J. Appl. Phys. 68 (1990) 2073–2080.

K.W. Schwarz, Phys. Rev. Lett. 78 (1997) 4785–4788.

E.A. Stach, K.W. Schwarz, R. Hull, F.M. Ross, R.M. Tromp, Phys. Rev. Lett. 84 (2000) 947–950.

E.A. Fitzgerald, phys. stat. sol. (a) 171 (1999) 227–238.

P. Sheldon, K.M. Jones, M.M. Al-Jassim, B.G. Yacobi, J. Appl. Phys. 63 (1988) 5609–5611.

K.L. Kavanagh, M.A. Capano, L.W. Hobbs, J.C. Barbour, P.M.J. Marée, W. Schaff, J.W. Mayer, D. Pettit, J.M. Woodall, J.A. Stroscio, R.M. Feenstra, J. Appl. Phys. 64 (1988) 4843–4852.

M. Grundmann, U. Lienert, D. Bimberg, A. Fischer-Colbrie, J.N. Miller, Appl. Phys. Lett. 55 (1989) 1765–1767.

B.A. Fox, W.A. Jesser, J. Appl. Phys. 68 (1990) 2739–2746.

R.S. Goldman, K.L. Kavanagh, H.H. Wieder, S.N. Ehrlich, R.M. Feenstra, J. Appl. Phys. 83 (1998) 5137–5149.

O. Yastrubchak, T. Wosiński, J.Z. Domagała, E. Łusakowska, T. Figielski, B. Pécz, and A.L. Tóth, J. Phys. Condens. Matter 16 (2004) S1–S8.

L. Gelczuk, D. Pucicki, J. Serafińczuk, M. Dąbrowska-Szata, P. Dłuzewski, J. Cryst. Growth 430 (2015) 14–20.

L. Gelczuk, J. Serafisiczuk, Mater. Sci. 26 (2008) 157.

E.A. Fitzgerald, G.P. Watson, R.E. Proano, D.G. Ast, P.D. Kirchner, G.D. Pettit, J.M. Woodall, J. Appl. Phys. 65 (1989) 2220–2237.

H. Teichler, Jpn. J. Appl. Phys. 16 (1977) 737-745.

I. Yonenaga, K. Sumino, J. Cryst. Growth 126 (1993) 19–29.

I. Yonenaga, K. Sumino, J. Appl. Phys. 65 (1989) 85–92.

M.J. Matragrano, D.G. Ast, J.R. Shealy, V. Krishnamoorthy, J. Appl. Phys. 79 (1996) 8371–8378.

P.M. Petroff, R.A. Logan, A. Savage, Phys. Rev. Lett. 44 (1980) 287–291.

M.S. Abrahams, J. Blanc, C.J. Buiocchi, Appl. Phys. Lett. 21 (1972) 185–186.

E.A. Fitzgerald, D.G. Ast, P.D. Kirchner, G.D. Pettit, J.M. Woodall, J. Appl. Phys. 63 (1988) 693–703.

F.R.N. Nabarro, T. Mura, Dislocations in Solids: Other Effects of Dislocations: Disclinations (Vol. 5), 1981.

V. V. Bulatov, J.F. Justo, W. Cai, S. Yip, A.S. Argon, T. Lenosky, M. De Koning, T. Diaz de la Rubia, Philos. Mag. A 81 (2001) 1257–1281.

J. Bennetto, R.W. Nunes, D. Vanderbilt, Phys. Rev. Lett. 849 (1997) 1–4.

X. Xu, S.P. Beckman, P. Specht, E.R. Weber, D.C. Chrzan, R.P. Erni, I. Arslan, N. Browning, A. Bleloch, C. Kisielowski, Phys. Rev. Lett. 95 (2005) 1–4.

V. V. Bulatov, Scr. Mater. 45 (2001) 1247–1252.

P. Hirsch, D. Cockayne, J. Spence, M. Whelan, Philos. Mag. 86 (2006) 4519–4528.

J. Spence, C. Koch, Scr. Mater. 45 (2001) 1273–1278.

T. Paulauskas, C. Buurma, E. Colegrove, B. Stafford, Z. Guo, M.K.Y. Chan, C. Sun, M.J. Kim, S. Sivananthan, R.F. Klie, Acta Crystallogr. Sect. A Found. Adv. 70 (2014) 524–531.

J. Narayan, S. Sharan, Mater. Sci. Eng. B 10 (1991) 261–267.

J.Y. Tsao, Materials Fundamentals of Molecular Beam Epitaxy, first ed., Academic Press, Inc., California, 2012.

P.F. Fewster, N.L. Andrew, J. Appl. Phys. 74 (1993) 3121–3125.

E. Ruska, P.W. Hawkes, R. Rudenberg, F. Brickwedde, M. Schwartz, Phys. Today 43 (1990) 84–85.

M. Haider, H. Rose, S. Uhlemann, B. Kabius, K. Urban, J. Electron Microsc. 47 (1998) 395–405.

O.L. Krivanek, N. Dellby, A.R. Lupini, Ultramicroscopy 78 (1999) 1–11.

P. Hartel, H. Rose, C. Dinges, Ultramicroscopy 63 (1996) 93–114.

D.J. Smith, Microsc. Microanal. (2008) 2–15.

T. Aoki, J. Lu, M.R. McCartney, D.J. Smith, Semicond. Sci. Technol. 31 (2016) 094002.

M. Tanaka, K. Tsuda, J. Electron Microsc. 60 (2011) 245–267.

C. Ophus, Microsc. Microanal. (2019) 563–582.

P.A. Stadelmann, Ultramicroscopy 21 (1987) 131–145.

A. Olsen, J.C.H. Spence, Philos. Mag. A 43 (1981) 945–965.

P. Lu, D.J. Smith, Philos. Mag. Part B 62 (1990) 435–450.

F.J. Giessibl, Rev. Mod. Phys. 75 (2003) 949–983.

T. Anan, M. Yamada, N. Nishi, K. Kurihara, K. Tokutome, A. Kamei, S. Sugou, Electron. Lett. 37 (2001) 566–567.

C.M. Jones, E. Kioupakis, J. Appl. Phys. 122 (2017) 045703.

F.C. Frank, J.H. Van Der Merwe, Proc. R. Soc. Lond. A 198 (1947) 205-216.

J.H. Van Der Merwe, J. Appl. Phys. 34 (1963) 117–122.

J.H. Van Der Merwe, J. Appl. Phys. 34 (1963) 123–127.

J.W. Matthews, S. Mader, T.B. Light, J. Appl. Phys. 41 (1970) 3800–3804.

J. Narayan, S. Oktyabrsky, J. Appl. Phys. 92 (2002) 7122–7127.

Y.B. Bolkhovityanov, A.S. Deryabin, A.K. Gutakovskii, L. V. Sokolov, A.P. Vasilenko, Acta Mater. 61 (2013) 5400–5405.

K.H. Chang, P.K. Bhattacharya, R. Gibala, J. Appl. Phys. 66 (1989) 2993–2998.

J. Zou, D.J.H. Cockayne, B.F. Usher, J. Appl. Phys. 73 (1993) 619–626.

A. Maros, N. Faleev, R.R. King, C.B. Honsberg, D. Convey, H. Xie, F.A. Ponce, J. Vac. Sci. Technol. B 34 (2016) 02L113.

B.P. Rodríguez, J.M. Millunchick, J. Appl. Phys. 100 (2006) 4–11.

A. Gangopadhyay, A. Maros, N. Faleev, D.J. Smith, Acta Mater. 162 (2019) 303-315.

D.B. Williams, C.B. Carter, Transmission Electron Microscopy: A Textbook for Materials Science, second ed., Springer, New York, 2009.

F.A. Ponce, D.P. Bour, W.T. Young, M. Saunders, J.W. Steeds, Appl. Phys. Lett. 69 (1996) 337–339.

D.J. Smith, R.W. Glaisher, P. Lu, Philos. Mag. Lett. 59 (1989) 69–75.

M. De La Mata, C. Magen, J. Gazquez, M.I.B. Utama, M. Heiss, S. Lopatin, F. Furtmayr, C.J. Fernández-Rojas, B. Peng, J.R. Morante, R. Rurali, M. Eickhoff, A. Fontcuberta I Morral, Q. Xiong, J. Arbiol, Nano Lett. 12 (2012) 2579–2586.

J. Tafto, J.C.H. Spence, J. Appl. Crystallogr. 15 (1982) 60–64.

S. Lavagne, C. Roucau, C. Levade, G. Vanderschaeve, Philos. Mag. A 82 (2002) 1451–1462.

M.E. Twigg, J. Appl. Phys. 68 (1990) 5109–5114.

T.J. Gosling, R. Bullough, S.C. Jain, J.R. Willis, J. Appl. Phys. 73 (1993) 8267–8278.

J.W.P. Hsu, E.A. Fitzgerald, Y.H. Xie, P.J. Silverman, M.J. Cardillo, Appl. Phys. Lett. 61 (1992) 1293–1295.

K.H. Chang, R. Gilbala, D.J. Srolovitz, P.K. Bhattacharya, J.F. Mansfield, J. Appl. Phys. 67 (1990) 4093–4098.

W. Hagen, H. Strunk, Appl. Phys. 17**,** (1978) 85-87.

A.M. Andrews, J.S. Speck, A.E. Romanov, M. Bobeth, W. Pompe, J. Appl. Phys. 91 (2002) 1933–1943.

T. Wosiński, O. Yastrubchak, A. Mąkosa, T. Figielski, J. Phys. Condens. Matter 12 (2000) 10153–10160.

T. Wosiński, A. Mąkosa, T. Figielski, J. Raczyńska, Appl. Phys. Lett. 67 (1995) 1131.

L.I. Fedina, A.K. Gutakovskii, T.S. Shamirzaev, J. Appl. Phys. 124 (2018).

R. Hull, R. A. Logan, B. E. Weir, and J.M. Vandenberg, Appl. Phys. Lett. 63 (1993) 1504.

J. Hornstra, J. Phys. Chem. Solids 5 (1958) 129–141.

Y. Arroyo Rojas Dasilva, R. Kozak, R. Erni, M.D. Rossell, Ultramicroscopy 176 (2017) 11–22.

Y. Arroyo Rojas Dasilva, M.D. Rossell, F. Isa, R. Erni, G. Isella, H. von Känel, P. Gröning, Scr. Mater. 127 (2017) 169–172.

A. Gangopadhyay, A. Maros, N. Faleev, D.J. Smith, Scr. Mater. 153 (2018) 77–80.

D.B. Holt, J. Phys. Chem. Solids 23 (1962) 1353–1362.

M.Y. Gutkin, M. Militzer, A.E. Romanov, V.I. Vladimirov, Phys. Status Solidi 113 (1989) 337–344.

X. Wu, G.C. Weatherly, Semicond. Sci. Technol. 18 (2003) 307–311.

J. Zou, D.J.H. Cockayne, Appl. Phys. Lett. 63 (1993) 2222–2224.

H. Akinaga, K. Tanaka, K. Ando, T. Katayama, J. Cryst. Growth 0248 (1995) 0–5.

P.M.J. Marée, J.C. Barbour, J.F. Van Der Veen, K.L. Kavanagh, C.W.T. Bulle-Lieuwma, M.P.A. Viegers, J. Appl. Phys. 62 (1987) 4413–4420.

B.R. Bennett, R. Magno, J.B. Boos, W. Kruppa, M.G. Ancona, Solid. State. Electron. 49 (2005) 1875–1895.

G.T. Nelson, B.C. Juang, M.A. Slocum, Z.S. Bittner, R.B. Laghumavarapu, D.L. Huffaker, S.M. Hubbard, Appl. Phys. Lett. 111 (2017) 231104.

S. Huang, G. Balakrishnan, D.L. Huffaker, J. Appl. Phys. 105 (2009).

S.H. Huang, G. Balakrishnan, A. Khoshakhlagh, A. Jallipalli, L.R. Dawson, D.L. Huffaker, Appl. Phys. Lett. 88 (2006) 131911.

W. Qian, M. Skowronski, R. Kaspi, M. De Graef, V.P. Dravid, J. Appl. Phys. 81 (1997) 7268–7272.

A. Jallipalli, G. Balakrishnan, S.H. Huang, T.J. Rotter, K. Nunna, B.L. Liang, L.R. Dawson, D.L. Huffaker, Nanoscale Res. Lett. 4 (2009) 1458–1462.

A. Vilà, A. Cornet, J.R. Morante, P. Ruterana, M. Loubradou, R. Bonnet, Y. González, L. González, Philos. Mag. A Phys. Condens. Matter, Struct. Defects Mech. Prop. 71 (1995) 85–103.

D.J. Smith, Prog. Cryst. Growth Charact. Mater. 66 (2020) 100498.

Y. Wang, P. Ruterana, J. Chen, S. Kret, S. El Kazzi, C. Genevois, L. Desplanque, X. Wallart, ACS Appl. Mater. Interfaces 5 (2013) 9760–9764.

A.J. McGibbon, S.J. Pennycook, J.E. Angelo, Science 269 (1995) 519–522.

A.Y. Borisevich, A.R. Lupini, S.J. Pennycook, Proc. Natl. Acad. Sci. U. S. A. (2006).

H. Yang, J.G. Lozano, T.J. Pennycook, L. Jones, P.B. Hirsch, P.D. Nellist, Nat. Commun. 6 (2015) 1–7.

H. Du, C.L. Jia, L. Houben, V. Metlenko, R.A. De Souza, R. Waser, J. Mayer, Acta Mater. 89 (2015) 344–351.

S. Wang, K. March, F.A. Ponce, P. Rez, Phys. Rev. B 99 (2019) 115312.

W.J. Bowman, K. March, C.A. Hernandez, P.A. Crozier, Ultramicroscopy 167 (2016) 5-10.

P.E. Batson, M.J. Lagos, Ultramicroscopy 180 (2017) 34–40.